Aus der Klinik für Kardiologie, Pneumologie und Angiologie
der Heinrich-Heine-Universität Düsseldorf
Direktor: Univ.-Prof. Dr. med. Malte Kelm

Non invasive quantification of angioplasty induced vascular inflammation by ^{19}F MRI
Histological validation

Dissertation

zur Erlangung des Grades eines Doktors der Medizin der Medizinischen Fakultät der
Heinrich-Heine-Universität Düsseldorf

vorgelegt von
Moritz Walz
2023

Als Inauguraldissertation gedruckt mit Genehmigung der Medizinischen Fakultät der Heinrich-Heine-Universität Düsseldorf

gez.:

Dekan: Prof. Dr. med. Nikolaj Klöcker

Erstgutachter: PD Dr. med. Florian Bönner

Zweitgutachter: PD Dr. med. Michael Gliem

Zusammenfassung

Atherosklerosebedingte kardiovaskuläre Erkrankungen (ASCVD) stellen trotz großen Fortschritten in Behandlung und Prävention eine der häufigsten Gründe für Morbitität und Mortalität dar. Eine wichtige Ursache für die hohe ASCVD Krankheitslast liegt darin begründet, dass viele arterielle atherosklerotische Plaques keine Symptome verursachen bis zu dem Zeitpunkt, an dem es zur Ruptur des Plaques kommt und dramatische Komplikationen wie Herzinfarkt und Schlaganfall resultieren. Dennoch entwickelt ein Großteil der von Atherosklerose betroffenen Personen niemals diese Komplikationen. Aus diesem Grunde wäre es wünschenswert, spezifisch jene Patienten zu identifizieren, die ein hohes Risiko für eine Plaqueruptur aufweisen. Zurzeit ist kein Screeningverfahren in klinischen Alltag verfügbar, das die Detektion und Charakterisierung atherosklerotischer Plaques in verschiedenen Gefäßterritorien ermöglicht. Computertomographie und Positronenemissionstomographie wurden in der klinischen Forschung hinsichtlich dieser Fragestellung getestet. Ein weiteres vielversprechendes Bildgebungsverfahren ist das ^{19}F-Fluor MRT unter Verwendung von intravenösem Perfluorocarbon (PFC) Nanoemulsions-Kontrastmittel. Im Mausmodell konnten mittels ^{19}F Bildgebung bereits rupturgefährdete Plaques in experimentellen 9.4 T Scannern dargestellt werden. Derzeit gibt es jedoch keine Studien, die diese Ergebnisse bei klinisch eingesetzten Magnetfeldstärken bestätigen.

Im Schweinemodell haben wir ein Verfahren zur Induktion von Gefäßverletzung und -entzündung entwickelt, um die Möglichkeit der ^{19}F MRT-basierten Detektion von Gefäßinflammation bei 3 T zu evaluieren. In acht Aachen Minipigs wurde mittels Angioplastiekatheter eine endovaskuläre Endotheldenudation und/oder Ballonüberdehnung einer A. carotis durchgeführt. Die kontralateralen Arterien dienten als Kontrolle. Nach der Prozedur wurde die PFC Nanoemulsion verabreicht und die Karotiden wurden mittels ^{19}F MRT *in vivo* und *ex vivo* hinsichtlich des Ausmaßes der Entzündungsreaktion untersucht. Zur Validierung der MRT-Befunde wurden histologische Schnitte der Arterien angefertigt.

Ex vivo ^{19}F-Kontrastanreicherung konnte in allen behandelten Arterien, jedoch in keinem der Kontrollgefäße festgestellt werden. Mikroskopisch zeigte sich eine ausgeprägte Entzündungsreaktion in den behandelten Karotiden während keine Entzündung in der Kontrollgruppe gefunden wurde. Das Ausmaß der Entzündung wurde durch Zählung aller Zellen sowie der CD163$^+$ Makrophagen quantifiziert. Die Zellzahlen entsprachen etwa denen, die in der Literatur für atherosklerotische Plaques angegeben werden. Weiterhin korrelierte die Stärke der Entzündung mit dem ^{19}F-Kontrastsignal.

Unsere *proof-of-concept* Studie zeigt, dass selbst kleine Entzündungsfoci reproduzierbar mittels ^{19}F Bildgebung dargestellt werden können. Dennoch sind weitere Studien notwendig, um in verschiedenen Gefäßterritorien zu evaluieren, ob auch atherosklerose assoziierte Entzündungen nachweisbar sind. Der Vorteil des ^{19}F MRT im Vergleich zur CT- und PET-basierten Atherosklerosebildgebung ist die breite Verfügbarkeit und die Strahlenunabhängigkeit des Verfahrens. Ferner können verschiedene funktionalisierte PFC Kontrastmittel kombiniert werden, um strukturelle und zelluläre Komponenten vulnerabler Atheroskleroseplaques zu identifizieren.

Summary

Atherosclerotic cardiovascular diseases (ASCVD) remain among the most common causes of morbidity and mortality in industrialized countries and worldwide despite major advances in treatment and prevention. An important reason for the high burden of ASCVD is the fact that many arterial atherosclerotic plaques do not cause any symptoms until the time at which they rupture and cause devastating complications such as myocardial infarction or stroke. Still, the majority of individuals affected by atherosclerosis never experiences these complications. Thus, it would be highly desirable to specifically identify those patients affected by atherosclerosis that are at risk for rupture. Research has shown that inflamed atheromas are especially likely to rupture. Currently, no screening tool is available in routine practice which is capable of detecting and characterizing atherosclerotic plaques across different vascular territories. Computed tomography and positron emission tomography are evaluated in clinical research for that purpose. Another promising imaging modality is the ^{19}F-fluorine MRI using intravenous Perfluorocarbon (PFC) nanoemulsion contrast. In mice, the ^{19}F imaging could delineate rupture-prone plaques using experimental 9.4 T MR scanners. To date, there are no studies that confirm these results at field strengths used in clinical practice.

We developed a pig model of vascular injury to determine the capability of the ^{19}F MRI to detect small sources of vascular inflammation at 3 T. Eight Aachen minipigs underwent an endovascular procedure that involved endothelial denudation and/or balloon overdistention of one carotid artery. The contralateral artery served as control. Thereafter, the PFC nanoemulsion was administered and the carotids were assessed for the presence and extent of vascular inflammation by ^{19}F MRI *in vivo* and *ex vivo*. Histological sections of the arteries were then prepared to validate the MRI findings.

^{19}F contrast enhancement could be found in all treated vessels *ex vivo*. None of the untreated carotids exhibited contrast enhancement. Microscopy of the explanted arteries confirmed the presence of significant inflammation in all treated carotids while signs of inflammation were absent in the control group. The size of the cellular inflammatory response was approximated by counting the number of all cells and of CD163^{+} macrophages on microscopic images. Cell counts were similar to values reported in the literature for atherosclerosis. Moreover, the intensity of the inflammatory response seen on histology correlated with the degree of ^{19}F contrast enhancement.

Our proof-of-concept study confirms that small sources of inflammation in the carotid arteries can be reliably detected by ^{19}F imaging. Further research in different vascular territories is necessary to determine whether the inflammatory response associated with atherosclerosis can also be resolved. Compared to CT- and PET-based atherosclerosis imaging, the ^{19}F MRI has the advantage that it is a radiation-free, widely available method that can be further enhanced by using a combination of functionalized PFC contrast agents that are able to identify different structural and cellular components which characterize vulnerable atherosclerotic plaques.

Abbreviations

^{18}FDG	^{18}Fluorodeoxyglucose
^{18}F-NaF	^{18}fluorine sodium fluoride
^{19}F MRI	^{19}fluorine magnetic resonance imaging
ABC	Antibody-biotin-complex
ATP	Adenosine triphosphate
ASCVD	Atherosclerotic cardiovascular diseases
ASDR	Age-standardized death rates
bFFE	Balanced fast field echo
BMW	Balanced middle weight
BW	Bodyweight
CCS	Coronary calcium scoring
CCTA	Coronary computed tomography angiography
CMR	Cardiac magnetic resonance
CI	Confidence interval
CT	Computed tomography
CVD	Cardiovascular diseases
DAMP	Danger-associated molecular pattern
DNA	Deoxyribonucleic acid
EDTA	Ethylendiaminotetraacetic acid
FAI	Fat attenuation index
FITC	Fluorescein isothiocyanate
FSC	Forward scatter
H&E	Hematoxylin & Eosin
ICAM-1	Intercellular adhesion molecule 1
IHC	Immunohistochemistry
IM	Intramuscular
IQR	Interquantile range
IU	International unit
IV	Intravenous
IVUS	Intravascular ultrasound
LAD	Left anterior descending coronary artery
LDL	Low-density lipoprotein
LFA-1	Leukocyte function-associated antigen 1
MACE	Major adverse cardiovascular events
mM	Millimolar
MRI	Magnetic resonance imaging
NLR	Nod-like receptor
NMR	Nuclear magnetic resonance
OCT	Optic-coherence tomography
OD	Optic density
oxLDL	Oxidized low-density lipoprotein
PAMP	Pathogen-associated molecular pattern
PBS	Phosphate-buffered saline
PC-CMR	Phase contrast cardiac magnetic resonance
PCS	Photon correlation spectroscopy
PET	Positron emission tomography
PEG	Polyethylenglycol
PFA	Paraformaldehyde
PFC	Perfluorocarbons
PFOB	Perfluorooctylbromide
PRR	Pattern recognition receptor
PSGL-1	P-selectin glycoprotein ligand-1
PTA	Percutaneous transluminal angioplasty
RCF	Relative centrifugal field
RGB	Red-Green-Blue
ROI	Region of interest
ROS	Reactive oxygen species
SMC	Smooth muscle cell
SNR	Signal to noise ratio
SPIO	Small paramagnetic particles of iron oxide
SSC	Side scatter
SSTR-2	Somatostatin receptor 2
TCFA	Thin-cap fibroatheroma
TE	Echo time
TLR	Toll-like receptor
TR	Repetition time
TSE	Turbo spin-echo
USPIO	Ultrasmall paramagnetic particles of iron oxide
VEGF	Vascular endothelial growth factor
VENC	phase contrast velocity enhanced

Contents

1 Introduction

1.1 Significance of Atherosclerotic Vascular Disease

Cardiovascular diseases (CVD) are the most prevalent cause of mortality worldwide, especially in industrialized countries (Wilkins et al., 2017; Townsend et al., 2016). CVD is an umbrella term including ischemic heart disease, cerebrovascular diseases, peripheral artery disease, atrial fibrillation, and others (Stewart et al., 2017). The majority of deaths from CVD are attributable to coronary heart disease and cerebrovascular diseases. Overall, CVD account for about 17.3 million deaths globally (31.5% of all deaths, 45% in industrialized countries). The number of deaths caused by CVD has shown a marked rise since 1990 from 12.3 million (25.9%). Thus, CVD have a vast economic impact, resulting in yearly expenditures 210 billion Euro in the EU. Because CVD frequently affect younger individuals, there are also social implications to consider since about a third of deaths are so-called "premature deaths" that occur at age less than 70.

Within most European countries, age standardized death rates (ASDR) of CVD have shown a major recline over the last decades. In Germany, for instance, a reduction in ASDR of nearly 30% was noted in 2013 as compared to 10 years prior. Regarding ischemic heart disease, the downward trend in mortality was even larger (-35.2% and -41.4% in males and females, respectively). The recline of CVD-ASDR in industrialized countries is likely due to a combination of primary preventive measures and improved care (Mensah et al., 2017). In different studies, it was estimated that lifestyle changes and treatment of CVD risk factors was responsible for 44 to 75% of the mortality reduction. Improved treatment may contribute up to 47% to the reduction of mortality.

The causative pathology underlying most instances of CVD is atherosclerosis. The prevalence of atherosclerosis exceeds the prevalence of CVD greatly since virtually all individuals are affected by atherosclerosis by a certain age (Strong et al., 1999; Webber et al., 2012). In many cases, though, atherosclerotic plaques remain clinically silent because the lesions do not cause any relevant luminal compromise (Libby et al., 2019). However, because of structural variability within atherosclerotic plaques some asymptomatic individuals are at high risk of plaque rupture and subsequent development of a coronary or cerebrovascular event. That is, plaques can be small and stable and thus never lead to symptoms, whereas other plaques are unstable even while they are still small in size (Naghavi et al., 2003; Gray et al., 2019). In a prospective trial by Stone et al. (2011), the authors investigated the occurrence of major adverse cardiovascular events (MACE) in patients who had a previous coronary angiography for an acute coronary syndrome. It was found that about half of the recorded MACE were due to lesions that caused a luminal obstruction of $32.3 \pm 20.6\%$ at the initial angiography. Presumably, most of these lesions were asymptomatic due to their small size. Nonetheless, they were unstable. It would be highly desirable to identify these high-risk non-obstructive lesions early to prevent the potentially devastating consequences of atherosclerotic plaque rupture by using the available treatment options. But while major advances in the management of CVD patients have lead to significant reductions in mortality, modalities to screen for the presence of subclinical vulnerable atherosclerotic plaques are still scarce, especially with regards to coronary and intracranial blood vessels (Gray et al., 2019; Waxman et al., 2006; Ryu et al., 2014). In the carotid territory, ultrasound examination can provide an estimation of plaque vulnerability but according to the 2020 guideline by the American Society of Echocardiography further research is still necessary to delineate the role of ultrasonography in the assessment of plaque vulnerability (Johri et al., 2020). Currently, non-invasive evaluation of coronary plaques is not possible by ultrasound.

In addition, there are two further reasons that make screening for unstable plaques a challenge. First, the large number of people at risk that need to be examined, and secondly, the relatively low prevalence of unstable plaques within the screened population. Even in patients with a history of an acute coronary

syndrome, only 104 of 1814 non-culprit lesions identified on angiography caused a MACE within a follow-up period of 3.4 years (Stone et al., 2011). Therefore, there are a number of demands on a potential diagnostic tool: (1) Lesion assessment should occur non-invasively because invasive procedures are not justified in a low risk population, (2) there should be no short or long term adverse effects from screening to ensure people's acceptance and to allow later reevaluations, (3) the method has to be widely available to permit broad useage, (4) both the sensitivity and specificity should be sufficiently high to obtain the desired diagnostic gain while avoiding overdiagnosis (Tomaniak et al., 2020).

It should be noted, though, that atherosclerotic plaques do not constitute a homogeneous entity (see also Section 1.2.2). Histological studies and, more recently, invasive imaging modalities like optic coherence tomography highlight the structural variability of plaques (Virmani et al., 2006a; Libby et al., 2019). Most lesions can be classified as either thin cap fibroatheromas (TCFA) or a fibrous cap atheromas. The thin fibrous cap of TCFA is prone to rupture which precedes thrombosis and infarction. As the name would imply, the strong fibrous cap of fibrous cap atheromas stabilizes such lesions. Infarction is typically due to an erosion of the plaque. The clinical characteristics of a myocardial infarction were shown to differ depending on the type of underlying atheroma. Ruptured TCFA present more commonly as STEMI and therefore benefit from early revascularization. Conversely, eroded plaques frequently lead to NSTEMI (Partida et al., 2018). Early clinical trials indicate that antiplatetet therapy may be an alternative to aggressive endovascular treatment in individuals presenting with plaque erosion (Jia et al., 2017).

Lifestyle changes and pharmacotherapy led to a change in the incidence of infarctions caused by TCFA rupture and eroded plaques. Plaque erosion is currently on the rise, potentially due to the fact that these plaques are less responsive to the currently recommended CVD treatment (Libby et al., 2019). The standard medical management of atherosclerosis involves statin therapy which stabilizes and inhibits the progression of atherosclerotic plaques by reducing LDL-cholesterol synthesis. Newer agents were developed to treat statin-intolerant patients or patients with a high residual risk despite the use of statins. Many of these drugs act by reducing the rate of LDL receptor degradation whereby the hepatic clearance of LDL-cholesterol is enhanced (Tokgözoğlu and Libby, 2022). Due to the differences in morphology between TCFA and eroded plaques, some experts argue that it may be beneficial to personalize treatment according to the type of lesion present in a certain patient. As noted for cases of plaque erosion, antiplatelet therapy may be most effective management option for fibrous cap atheromas. Similarly, there is preclinical evidence that other agents could modify the pathogenesis of plaque erosion. On the contrary, studies suggest that statins enhance neutrophil NETosis which is mechanistically linked to plaque erosion (Chow et al., 2010). This finding raises concern that statins may actually be detrimental in the treatment of fibrous cap atheromas (Libby et al., 2019). Thus, there is a clinical need to distinguish among patients with TCFA and eroded plaques to (1) guide pharmacologic management and (2) select patients that would benefit from a preventive catheter intervention.

Numerous biomarkers, including CRP, IL-6, IL-18, oxidized LDL, and matrix metalloproteinases, have been investigated in prospective observational studies regarding their potential to predict the presence of unstable plaques (Koenig and Khuseyinova, 2007). For a number of biomarkers statistical associations between plasma concentration and future cardiovascular events could be found. But these biomarkers lack the sensitivity and specificity to provide sufficiently high predictive values to guide clinical decision making, especially if used as a screening tool. Therefore, imaging modalities capable of detecting unstable atherosclerotic lesions are a more recent focus of research. A promising tool for that purpose is the ^{19}F MRI which we evaluated in a preclinical pig model of vascular injury. Other relevant approaches employed in the field of imaging atherosclerosis are discussed in Sections 1.3 and 4.6. The pathophysiological mechanism underlying the ^{19}F MRI-based visualization and stability assessment of atherosclerotic plaques of the TCFA subtype is inflammation. Therefore, central concepts pertaining to inflammation in general and to inflammatory processes within atherosclerotic plaques will be reviewed next.

1.2 General and Vascular Inflammation

1.2.1 General Sequences in Acute Tissue Inflammation

Inflammation is a somatic reaction to numerous exogenous and endogenous triggers. Common inducers of inflammation include (Rock et al., 2009):

- tissue necrosis
  - physical damage of tissue integrity
  - chemical insults
  - ischemia
- infection
- toxin exposure
- crystals
- antigens

Despite the diverse nature of these triggers of inflammation, the mechanisms underlying the ensuing inflammatory response are similar. The four main components that are responsible for inflammation are (1) the inducers of inflammation, (2) sensors tasked with detection of these inducers, (3) inflammatory mediators, and (4) the tissue affected by the inflammatory reaction (Rock et al., 2009; Medzhitov, 2010).

The initial process required for the development of inflammation is the detection of an abnormal condition within a tissue. This occurs by activation of special receptors, called *pattern recognition receptors* (PRRs), which are commonly expressed by cells of the innate immune system but also on non-immune cells (Prabhu and Frangogiannis, 2016). *Toll-like receptors* (TLR), *Nod-like receptors* (NLR), and *Scavenger receptors* are examples of receptors which signal a perturbation within a tissue (Medzhitov, 2010; Schroder and Tschopp, 2010; Zani et al., 2015). Molecules bound by these receptors are microbial peptides, carbohydrates, and nucleic acids, adenosinetriphosphate (ATP), uric acid, potassium ions, and others (Rock et al., 2009). Such molecules of microbial and non-microbial origin are collectively termed *pathogen associated molecular patterns* (PAMPs) and *danger associated molecular patterns* (DAMPs), respectively. The subsequent induction of inflammation is the physiological means to prevent the spread of tissue injury and to restore tissue integrity thereafter.

Mediators of inflammation are mainly proteins whose gene transcription into RNA is controlled by a signal cascade originating from the binding of DAMPs or PAMPs to PRRs (Rock et al., 2009). Interleukins and chemokines are examples of such proteins. The mediators are then secreted into the extracellular space to bind to specific receptors on other cells which informs these cells about the potentially harmful condition. They also lead to the recruitment of leukocytes from the circulation into inflamed tissues by inducing the following chain of events: The cytokine *Interleukin 1*β can cause an activation of endothelial cells. This leads to an enhanced expression of certain proteins on the endothelial surface which bind molecules located in leukocyte membranes. For example, the proteins *E-selektin* and *intercellular adhesion molecule 1* (ICAM-1) found on activated endothelium can interact with *leukocyte function-associated antigen 1* (LFA-1) and *P-selectin glycoprotein ligand-1* (PSGL-1) on leukocytes (Nourshargh and Alon, 2014). This enables leukocytes to adhere to endothelial cells in the microcirculation. Thereafter, leukocytes migrate from the blood into the extravascular space and then follow a concentration gradient of chemokines which guides the cells into the focus of inflammation (Weninger et al., 2014; Nourshargh and Alon, 2014).

The recruitment and activation of cells in inflammation is highly dynamic. During the course of

inflammation, different resident and immune cell populations can be found within the tissue. Commonly, neutrophils are the first type of leukocyte to migrate into a focus after the onset of inflammation. Later, macrophages accumulate in high numbers. Typically, neutrophils are responsible for degrading cells and debris by secreting reactive oxygen species (ROS) and proteolytic enzymes. The neutrophils then remove the debris via phagocytosis. After some days, the neutrophils perish within the inflamed tissue. At about that time, monocytes are recruited from the circulation and subsequently differentiate into macrophages. The macrophages continue the phagocytosis of inflammatory debris including also the perished neutrophils. This process is termed efferocytosis (see Section 4.4). Later, macrophages are involved in the resolution of inflammation and tissue restitution. This occurs by secretion of anti-inflammatory mediators and growth factors. In tissues capable of regeneration a complete restoration may occur by proliferation of resident cells. Tissues lacking this regenerative potential usually undergo reparation characterized by proliferation of fibroblasts and deposition of a connective tissue matrix which serves as a mechanically stable replacement of the destroyed tissue. This may result in a functional compromise (Sugimoto et al., 2016). Thus, an acute inflammatory response is characterized by a sequential tissue infiltration by different leukocyte populations and an activation of resident cells that attempt to restore tissue integrity. Even though the template of molecular and cellular dynamics outlined above occurs in virtually all foci of inflammation, the precise nature of the ongoing events differs depending on the type of tissue involved as well as the specific inflammatory trigger. The inflammatory processes associated with the initiation and progression of atherosclerosis are discussed below.

1.2.2 Specific Inflammatory Pattern in Atherosclerosis

In many cases, atherosclerosis is the pathological process underlying ischemic heart disease and cerebrovascular disease (Hansson et al., 2006; Witztum and Lichtman, 2014). Elucidation of its pathophysiology has therefore been a focus of research for many years. However, the precise mechanisms that lead to the development of atherosclerotic plaques are still not fully discovered. Initially, atherosclerosis was not considered to be an inflammatory disease. More recently, though, the pivotal role of inflammation in the development and progression of atherosclerotic plaques was recognized (Hansson et al., 2006).

Atherosclerotic plaques are thought to arise from precursor lesions termed *fatty streaks*. These precursors can already be seen in adolescents as deposits of lipids and lipid-laden macrophages in the vascular intima (Strong et al., 1999). The fatty streaks may then either progress to form an atherosclerotic plaque or may disappear over time (Hansson et al., 2006). It was found that atherosclerotic plaques occur preferentially at branching points within a vessel where blood flow is turbulent rather than laminar (Ross, 1999). This led to the hypothesis that an endothelial dysfunction may be the inciting factor that ultimately causes the formation of an atherosclerotic plaque (Moroni et al., 2019). Experimental data suggest that these abnormal flow conditions can by themselves change gene expression patterns and thereby induce an alteration in endothelial function (Nakashima et al., 1998). Next, the presence of elevated *low-density lipoprotein* (LDL) levels enhances the endothelial dysfunction. Ultimately, this leads to the deposition of LDL particles in the intima. These initial steps of atherogenesis are followed by numerous and complex cellular interactions that result in an inflammatory response (Skålén et al., 2002).

A key factor involved in plaque inflammation is the oxidation of subendothelial deposits of LDL by enzyme-mediated and non-enzymatic processes (Witztum and Steinberg, 1991). Oxidized LDL (oxLDL) was shown to be immunogenic by activating PRRs (Hansson et al., 2002). This causes the expression of adhesion molecules on the luminal membrane of endothelial cells and subsequent extravasation of monocytes into the subendothelium (Kume et al., 1992). After differentiation into macrophages, these cells may take up oxLDL via scavenger receptors which elicits intracellular signaling processes that cause the

release of further inflammatory mediators like ROS (Zani et al., 2015). In addition, cholesterol crystals from LDL can activate inflammasomes and thereby promote IL-1 secretion (Rajamäki et al., 2010). It is hypothesized that an ongoing cycle of LDL oxidation (via release of ROS), stimulation of PRRs (by oxLDL), recruitment of monocytes/macrophages (via oxLDL mediated endothelial activation), and progressive intimal lipid deposition ensues. On microscopy, macrophages inside the lesion appear as characteristic so-called *foam cells* due to cytoplasmic accumulation lipid-filled granules.

Mesenchymal cells also respond to the inflammatory reaction in the subendothelial space. Most notably, smooth muscle cells (SMC) are attracted into the lesion. Currently, the origin of these cells is unclear. The SMC may either represent activated SMC stemming from the vessel's media or SMC-precursors invading the lesion from the circulation (Bennett et al., 2016). The cells take on a special secretory phenotype, allowing them to secrete extracellular matrix components. Thereby, the atheroma becomes separated into two distinct parts: a lipid core and a fibrous cap. The fibrous cap is located between the lipid core and the endothelium. The lipid core consists of LDL, oxLDL, macrophages, necrotic cells and debris while the fibrous cap is composed of secretory SMC, collagen and extracellular matrix constituents (Hansson et al., 2002).

The fate of such an atheromatous plaque is diverse. It may remain stable in size, it may progress, or (rarely) regress (Brown et al., 1993). Intuitively, plaque progression is most relevant from a clinical perspective and may occur acutely or chronically. Chronic progression of a plaque (over a period of years) is typically associated with an enlargement of the fibrous cap. As a result, large plaques that cause a lumen compromise of 70% and more are unlikely to rupture since the strong fibrous cap stabilizes the atheroma (Fishbein and Siegel, 1996). On the contrary, smaller plaques often have much smaller caps rendering them more susceptible to rupture (Davies, 2000). The term *rupture* denotes a tearing of the plaque surface which exposes plaque constituents to the blood. Due to the high thrombogenicity of the lipid core, thrombus formation commonly ensues plaque rupture with subsequent hypoperfusion of downstream tissue (Virmani et al., 2006a). Of notice, histological studies suggest that only a subset of myocardial infarctions is related to plaque rupture. On tissue sections of coronary vessels from patients dying due to a myocardial infarction, different morphological patterns can be observed: (1) plaque rupture, (2) plaque erosion, and (3) calcified nodule (Virmani et al., 2006a). The mechanisms by which these different lesions cause an infarction differ. Plaque ruptures are found in ~60% of fatal coronary thromboses and are characterized by direct contact between the luminal thrombus and the necrotic core. In contrast, plaque erosions tend to occur in younger patients and make up the most of the remainder (~30%) of lethal cases of coronary thrombosis. In these instances, there is no direct contact between thrombus and necrotic core due to a thick overlying layer of non-endothelialized fibrous cap. Supposedly, a chronic low-grade inflammation causes a sloughing of endothelium in these lesions which can ultimately promote thrombus formation (Quillard et al., 2017). More detailed investigations revealed that these lesion patterns (rupture vs. erosion) differ by the size of the necrotic core, the number of cholesterol clefts, the extent of macrophage infiltration, the number of vasa vasorum, and hemosiderin-laden macrophages, which are all significantly greater in ruptured plaques (Virmani et al., 2006a). In fact, the pathophysiology of plaque erosion differs markedly from plaque rupture (see below). In plaque erosion, mechanical disruption of the integrity of the endothelial barrier appears to cause a low grade persistent inflammatory response that ultimately leads to luminal thrombus formation. A significant immune cell infiltration is not a feature of these lesions. Macrophages are rarely found while blood-borne neutrophils adhere to activated endothelial cells and then undergo NETosis. This enhances sloughing of the endothelium and stimulates the formation of a thrombus containing large numbers of platelets (Libby et al., 2019).

In atherosclerotic coronary arteries without evidence of a downstream infarction, lesions are often found that are morphologically similar to ruptured plaques, which were termed thin-cap fibroatheromas (TCFA). TCFA have been proposed as the precursor lesions of ruptured plaques (Virmani et al., 2006a).

Internally, TCFA resemble ruptured plaques as indicated by a large necrotic core, a high number of cholesterol clefts, and significant macrophage infiltration. On the contrary, the vasa vasorum density and the number of hemosiderin-laden macrophages is significantly less in TCFA than in ruptured plaques. Still, the number of vasa vasorum was found to be twofold greater in vulnerable plaques than in stable lesions, whereas the vasa vasorum density was fourfold increased in ruptured plaques (Virmani et al., 2005). Based on these findings Virmani et al. (2005) proposed a model that suggests that intraplaque hemorrhage may be responsible for the acute progression of vulnerable TCFA into rupture-prone lesions. The sequence of events may be the following: The local microenvironment within the necrotic core stimulates the ingrowth of blood vessels from the adventitial vasa vasorum through the media into the proximity of the necrotic core. Due to poorly formed vessel walls, hemorrhage into the core ensues. The extravasated red blood cells are then taken up by lesion macrophages. Because of the high cholesterol content of the erythrocyte membrane (Cooper, 1978), this process causes a massive accumulation of cholesterol within the necrotic core and thus underlies its acute enlargement. Hypoxia inside the necrotic core and inflammatory mediators released by activated immune cells have been implicated in the stimulation of angiogenesis (Camaré et al., 2017). Specifically, hypoxia induced by the enhanced metabolism and proinflammatory cytokines stimulate the expression of angiogenic factors while released proteases facilitate endothelial cell migration. Therefore, a high density of intraplaque vessels and hemosiderin-laden macrophages may be indicative of imminent TCFA rupture. Conversely, the size of the necrotic core and macrophage infiltration as potential triggers of angiogenesis may be earlier signs of plaque vulnerability. This model is consistent with pathological and clinical observations which show that an acute increase in plaque size precedes rupture. On histology, the necrotic core occupies about a fourth of the total plaque area in TCFA and between a third to one half in ruptured plaques. Similarly, Stone et al. reported an increase in mean luminal stenosis of lesions from $32.3 \pm 20.6\%$ on a previous angiography to $65.4 \pm 16.3\%$ at the time when the lesion caused a MACE. In fact, the authors found that most lesions responsible for a subsequent MACE caused only mild lumen compromise, initially: 30.2% of these plaques had <30% stenosis, 36.8% <50% stenosis, 28.3% <70% stenosis. In only 4.7% of these cases, the stenosis exceeded 70%.

Due to the pivotal role of monocytes/macrophages in the formation, progression and potential rupture of atherosclerotic plaques (Moroni et al., 2019), numerous studies attempted to gain more detailed insights into the mechanisms by which these cells affect plaque physiology (Nagenborg et al., 2017). Monocytes are bone-marrow derived cells that circulate in the peripheral blood and can differentiate into macrophages or dendritic cells after migration into tissues (León et al., 2005). Traditionally, two monocyte subpopulations are distinguished: A classical subset characterized by strong CD14 and absent CD16 expression ($CD14^{++}/CD16^{-}$) and monocytes that express both CD14 and CD16 on the cell surface (Passlick et al., 1989). The latter group was further subdivided into intermediate and non-classical populations that differ in the strength of CD16 expression. Non-classical monocytes show a stronger CD16 positivity ($CD14^{+}/CD16^{++}$) than intermediate monocytes ($CD14^{++}/CD16^{+}$) (Ziegler-Heitbrock et al., 2010). These different phenotypes are associated with different cell function as indicated by their respective receptor and cytokine profiles. Classical monocytes mainly secrete proinflammatory cytokines and are linked to antimicrobial defense. Intermediate monocytes secrete both pro- and antiinflammatory cytokines. In fact, these cells may be the main source of IL-10 and show the highest expression of MHC class 2 and are thereby able to interact strongly with $CD4^{+}$ T cells. Non-classical monocytes resemble mature tissue-resident macrophages and engage in phagocytic removal of damaged cells (Wong et al., 2011; Skrzeczyńska-Moncznik et al., 2008). Investigations focusing on the impact of the monocyte populations on the fate of atheromas yielded inconsistent results. Findings by Yamamoto et al. (2018) indicate that the number of $CD14^{++}$ $CD16^{+}$ monocytes in the blood is inversely related to coronary plaque cap thickness. Similarly, Rogacev et al. (2012) report that intermediate monocytes were the only subset to

independently predict cardiovascular events in a prospective clinical trial. In contrast, another prospective trial revealed that classical monocytes could predict cardiovascular events even though they were not associated with the extent of atherosclerosis at baseline. This was attributed to potential inflammatory effects caused by these cells that may promote plaque rupture. Additionally, a larger percentage of intermediate monocytes was associated with a smaller carotid intima-media thickness in the same study (Berg et al., 2012). It should be noted, though, that the relationship between macrophages situated within atherosclerotic plaques and the circulating monocytes is currently under debate. Two potential sources of lesional macrophages are proposed. The cells may either derive from circulating monocytes that migrate into the tissue (Swirski et al., 2007) which would suggest a close relation between monocyte subsets in the peripheral blood and lesional stability. Alternatively, local proliferation of tissue resident macrophages may supply a plaque's macrophage population (Robbins et al., 2013). Similar to monocytes, two traditional macrophage subsets are described: "Proinflammatory" M1 and "antiinflammatory" M2 macrophages. However, due to various possible stimuli that can act on macrophages, these cells can take on numerous phenotypes with different cytokine and receptor profiles and thus functional characteristics (Nagenborg et al., 2017). Therefore, the dichotomous M1/M2 concept cannot capture the diverse nature of macrophages. Still, M1/M2-based classifications are commonly used in research to investigate the impact of different macrophage populations on atheromatous lesions. As with monocytes, there have also been conflicting findings regarding the role of the two macrophage subsets with respect to plaque progression and stability. M1 macrophages were found to be associated with progression while M2 macrophages were associated with stable plaques in some clinical and preclinical studies (De Gaetano et al., 2016; Cardilo-Reis et al., 2012). These findings could not be reproduced in a study by van Dijk et al. (2016) where it was shown that both the number M1 and M2 macrophages within atherosclerotic plaques was indicative of histological signs of plaque progression.

Thus, there is evidence that the overall macrophage infiltration or infiltration by certain subpopulations can be indicative of plaque vulnerability. Observational studies suggest that a more detailed characterization of lesional macrophages beyond the traditional subpopulations could provide a superior discrimination of plaque prognosis. Scholtes et al. (2012) report that enhanced expression of *matrix metalloproteinase 12* in carotid plaques is associated with an increased risk of a future MACE. On the same note, the number of $CD163^{+}$ macrophages in carotid atheromas correlates with clinical symptoms (Bengtsson et al., 2020). Hence, different monocyte/macrophage populations may be associated with or contribute to plaque morphology across different vascular territories. Due to the complex and pleomorphic effects of these cells on plaque progression and stability, it is likely that only a precise analysis of a plaque's cellular composition will permit confident conclusions about the fate of a lesion.

To summarize, vulnerable TCFA commonly do not cause a sufficient luminal obstruction to become symptomatic, initially. Later, a rapid expansion of the plaque core may occur which heralds a rupture. The responsible local environmental factor may be hemorrhage into the lesion's necrotic core. Since the release of inflammatory mediators by lesion macrophages plays a crucial role in hemorrhage and thus in the initiation of plaque destabilization, a high macrophage density within the necrotic core may be an early sign of a vulnerable atheroma.

Because of the missing association between size and vulnerability of certain atherosclerotic lesions, many high-risk patients tend to be asymptomatic (Gray et al., 2019). Therefore, clinical tests that assess perfusion are often not sensitive with regards to detection of vulnerable plaques (Stone et al., 2011). Alternative diagnostic tools that are able to discern the internal composition of plaques would allow a more precise conclusion about plaque rupture risks. Accordingly, the visualization of enhanced metabolism, macrophage infiltration, and microcalcifications within the necrotic core have been targets of clinical research projects that aim to identify vulnerable atheromas (see Section 4.6).

1.2.3 Specific Inflammatory Pattern after Angioplasty

The inflammatory pattern that ensues angioplasty is complex and diverse (Tan et al., 2021). From clinical experience it is evident that blood vessels from different vascular territories show a distinct response to endovascular intervention. This finding is hypothesized to reflect the mechanical properties of the affected arteries. Elastic vessels like carotids are less likely to undergo remodeling processes that culminate in restenosis as compared to muscular arteries (Schillinger and Minar, 2005). But even within the group of muscular arteries, lower extremity supplying vessels are significantly more prone to become restenotic than coronaries. Some authors suggest that the type and extent of post-angioplasty inflammation is a central contributor to the difference of the arterial responses across different vascular territories (Schillinger and Minar, 2005; Tan et al., 2021).

The precise mechanisms that govern angioplasty-induced inflammation are still unknown. Studies indicate that endothelial damage and overstretch injury trigger the inflammation. The local release of proinflammatory cytokines activates circulating monocytes which subsequently adhere to the damaged endothelium (Serrano et al., 1997; Tsakiris et al., 1999). Thereby, the cells are recruited into the lesion and, along with resident macrophages, differentiate into certain macrophage subpopulations. As noted above, M1 and M2 macrophage subsets are distinguished. Research indicates that "proinflammatory" M1 macrophages drive the inflammation and subsequent restenosis while the "antiinflammatory" M2 subset may stabilize the lesions (Kosmac et al., 2020; Tan et al., 2021). Overstretch injury leads to an adventitial response which is characterized by collagen deposition and constrictive remodeling (Rud Andersen et al., 1996). This finding is associated with an increase in the local vasa vasorum density (Pels et al., 1999). One of the cytokines involved in this process may be *vascular endothelial growth factor* (VEGF). Different studies indicated conflicting effects of VEGF signaling after angioplasty. Some authors reported antiatherogenic properties while others found a proatherogenic response. These findings may be due to the pleiotropic cellular reponses to VEGF. VEGF stimulates endothelial proliferation and thereby accelerates reendothelialization after endovascular injury. Reendothelialization restores the superficial tissue integrity and thereby may reduce the stimulus for neointima formation. Accordingly, Asahara et al. (1995) showed that intimal thickening could be attenuated by local delivery of VEGF. Conversely, the mechanistic link between VEGF release and enhanced neointima formation may be its effect on monocytes. In vitro studies by Yamada et al. (2003) revealed that exposure of endothelial cells to VEGF stimulates the release of the potent monocyte/macrophage attractant *monocyte chemoattractant protein 1.* In fact, Ohtani et al. (2004) found that inhibition of VEGF signaling inhibited neointima formation which was attributed to a reduction in monocyte recruitement into the damaged arterial wall. These findings highlight the complex nature of the events that occur after angioplasty. This is further emphasized by clinical data. During coronary interventions, drug-eluting stents have become the mainstay of treatment due to their favorable effects on early restenosis (Brar et al., 2009). Conversely, findings were sobering after stenting arterial vessels of the lower extremity. Irrespective of the use of bare-metal or drug-eluting stents restenosis rates remain high relatively shortly after the procedure. A more detailed understanding of the mechanisms underlying restenosis has driven the development of novel treatment strategies for peripheral artery disease. Stents coated with agents that polarize macrophages towards the M2 phenotype may provide more sustained patency rates after endovascular intervention by reducing inflammation as a driver of restenosis (Tan et al., 2021).

1.3 Imaging Concepts of Atherosclerosis and Angioplasty-induced Inflammation

1.3.1 CT

Coronary computed tomography angiography (CCTA) is recommended among the first line diagnostic modalities in patients with chronic coronary syndrome (Knuuti et al., 2019). Accordingly, there has been significant interest to identify criteria that can accurately predict outcomes in patients whose CT findings do not demand that an angiographic intervention be scheluded. This is especially relevant since the majority (>90%) of these CCTA do not reveal any major coronary obstruction (Douglas et al., 2015). Still, in a significant proportion of these patients unstable coronary plaques may exist. Therefore, there is a clinical need to risk stratify patients with unremarkable CCTA findings. A guideline-recommended CCTA marker indicative of cardiovascular risk is coronary calcium scoring (CCS). CCS quantifies the extent of coronary calcification which is associated with the severity of atherosclerotic disease and correlates with cardiac event rates (Greenland et al., 2018). However, based on correlations between CCS and optic coherence tomography (OCT), CCS cannot confidently identify vulnerable atherosclerotic plaques. Ong et al. (2016) report that stable atherosclerotic lesions and ruptured plaques do not differ significantly in their degree of calcification on OCT. Since CCS actually overestimates the extent of calcification seen on OCT (Monizzi et al., 2020), it can be inferred that CCS would be unsuitable to differentiate between stable and unstable lesions. Thus, the current guidelines recommend CCS mainly for overall patient risk stratification whereby the indications for statin or antiplatelet medication can be assessed. In addition, coronary calcification is a largely irreversible process that may actually be enhanced by statin administration (Chironi et al., 2002; Greenland et al., 2007; Dykun et al., 2016). Thus, the CCS cannot capture any statin-induced stabilization of coronary plaques.

More recently, a novel CT marker was developed to evaluate coronary atherosclerotic plaques. Antonopoulos et al. (2017) showed that the perivascular adipose tissue surrounding the coronary arteries responds to inflammatory mediators released from a nearby atheroma. The differentiation of preadipocytes into mature adipocytes was found to be inhibited by the paracrine effect of the secreted cytokines. Because of the lower lipid content in preadipocytes compared to mature fat cells, the x-ray attenuation of the perivascular tissue was assumed to be stronger in close proximity to a coronary plaque and to diminish with increasing distance. Based on this pathomechanism, the authors developed the *fat attenuation index* (FAI) which measures the mean x-ray attenuation in concentric cylindrical volumes around the perimeter of coronary vessels. As predicted, the FAI of culprit lesions was significantly greater than the FAI of uninvolved coronary vessel segments in patients with acute myocardial infarction. Oikonomou et al. (2018) verified these results in large patient cohorts in a prospective study. A higher FAI was significantly associated with increased overall and cardiac mortality within follow-up periods of ~8 years. Further, in a post-hoc analysis Oikonomou et al. (2020) report that the FAI supersedes the predictive value of other CT markers of high risk plaques. A low FAI reflected a low cardiac mortality within the above timeframe irrespective of the presence or absence of other high risk features found on CCTA. Conversely, a high FAI was associated with a significantly increased cardiac mortality. In the presence of additional CCTA high risk markers, mortality rates were even greater. Still, it is not clear whether the FAI can specifically detect those atherosclerotic lesions that evolve into future culprit lesions.

1.3.2 PET

The major advantage of Positron emission tomography (PET) over CT or MRI is its high sensitivity allowing the detection of even minimal sources of signal. In the case of molecular imaging (see below), picomolar concentrations of contrast agent can be reliably detected (Tarkin et al., 2016). Due to the limited spatial resolution of ~5 mm, PET images are generally coregistered with CT or MRI to improve resolution. Among the PET contrast agents to image the inflammatory response in atherosclerosis is ^{18}Fluorodeoxyglucose (^{18}FDG). The enhanced metabolic activity due to the ongoing inflammatory processes inside atherosclerotic lesions is the pathophysiological basis for accumulation of ^{18}FDG. Both coronary (Wykrzykowska et al., 2009; Rogers et al., 2010) and carotid plaques (Menezes et al., 2011) could be detected clinically by ^{18}FDG PET-CT. It was shown by Rogers et al. that ^{18}FDG enhancement predominantly localizes to areas of atherosclerotic activity. Further, it was possible to detect a gradation of tracer deposition depending on the state of the underlying atheroma. Plaques stented for acute coronary syndromes exhibited stronger enhancement than recently and remotely stented stable plaques. This finding is in line with the concept that the progression of hemodynamically irrelevant plaques into rupture prone lesions is a highly inflammatory process while stable lesions demonstrate less inflammation (Virmani et al., 2005). However, the study could not resolve whether the inflammatory activity responsible for ^{18}FDG enhancement preceded the acute coronary event or was its consequence. To address the issue of temporality, Fernández-Friera et al. (2019) performed a cross-sectional study on subjects from the general population where the presence of atherosclerosis and vascular inflammation was coregistered by PET-MRI. The authors investigated the carotid, iliac, and femoral arterial territories. They report that vascular inflammation was present in 48.2% of individuals with a median of 2 sites of tracer accumulation. Interestingly, the majority (~89%) of PET-enhanced sites were not associated with the presence of atheromas as seen on MRI. It was hypothesized that this finding reflects different stages in the development of atheromas. Early lesions that are not yet noticeable on MRI may be characterized by a significant amount of inflammation while established plaques are quiescent and thus devoid of ^{18}FDG PET detectable inflammation. Therefore, the remaining 11% of plaques that were colocalized with inflammatory signs were of particular interest. They tended to be larger, showed features of positive remodeling, and commonly presented with MRI characteristics of a large lipid core. These plaque morphologies are associated with a tendency to rupture (Choudhury et al., 2002) which, again, is consistent with the notion that inflammation heralds high risk lesions. In addition, it provides presumptive evidence that inflammation detected by Rogers et al. after acute coronary syndromes is, at least in part, due to the underlying atheroma rather than being solely caused by plaque rupture. It should be noted, though, that the imaging of coronary atherosclerosis is challenging due to the avid ^{18}FDG uptake by the myocardium. To reduce myocardial enhancement relative to plaque enhancement, patients need to be placed on a special preparatory diet prior to PET-scanning (Wykrzykowska et al., 2009).

In addition to ^{18}FDG, other PET-tracers are available that aim to identify certain cellular and functional components relevant to atherogenesis. Among these are *Somatostatin receptor 2* (SSTR-2) analogues and ^{18}F sodium fluoride (^{18}F-NaF). SSTR-2 analogues specifically bind to monocytes/macrophages and thereby allow the visualization of monocyte/macrophage-dense regions of atherosclerotic plaques (Syed et al., 2019; Tarkin et al., 2016). Thereby, vulnerable coronary and carotid lesions could be detected with higher sensitivity than using ^{18}FDG tracers (Tarkin et al., 2017). ^{18}F-NaF has also been used to visualize atherosclerosis *in vivo*. ^{18}F-NaF binds to plaque-associated microcalcifications. This type of imaging provides additional diagnostic value as compared to conventional coronary calcium scoring due to its ability to identify plaques that undergo active calcifications. As noted in Section 1.3.1, the mere presence of calcification is not a specific sign of vulnerable plaques. Rather, actively calcifying lesions may be at an increased risk for rupture (Shi et al., 2020). Accordingly, (Dweck et al., 2012) found that

increased lesional ^{18}F-NaF uptake was associated with elevated risk as determined by clinical prognostic scores while coronary calcium scoring was not. Further, Joshi et al. (2014) found that culprit plaques reponsible for myocardial infarctions exhibited stronger ^{18}F-NaF enhancement than non-culprit lesions. Additionally, carotid endarterectomy specimens with ^{18}F-NaF uptake were characterized histologically by microcalcifications, macrophage infiltration and necrosis which are all features of vulnerable plaques (Virmani et al., 2006a; Howard et al., 2015).

Despite the proven clinical applicability of PET to detect atherosclerotic lesions, a number of downsides of PET imaging need to be considered. First, it is a costly method that inherently requires exposure to radiation. Thus, patients younger than age 50 were excluded in the study by Joshi et al. to prevent long-term adverse effects from radiation exposure. Next, the almost exclusively used radionuclide is ^{18}F. Due to its short half-life of ~110 minutes, imaging of longer processes like cell migration is not possible (Wüst et al., 2019). Further, regarding the use of ^{18}FDG to image coronary atherosclerosis, Wykrzykowska et al. report that the preparatory diet was ineffective at diminishing myocardial contrast enhancement in about 25% of patients, mainly due to non-adherence to dietary restrictions. Similarly, results from Joshi et al. show that suppression of myocardial ^{18}FDG uptake could not be achieved in 15% of patients. Still, proper interpretation of the coronary ^{18}FDG uptake was possible only in less than half of the examined arterial territories due to spillover of residual myocardial enhancement. Moreover, Wykrzykowska et al.; Dweck et al.; Joshi et al. excluded patients with insulin dependent Diabetes mellitus in their studies. Finally, enhancing PET-imaging by using multiple tracers is a challenging procedure that often requires long examination times and is highly susceptible to noise (Kadrmas and Hoffman, 2013).

1.3.3 MRI

Nuclear Magnetic Resonance

Nuclear magnetic resonance (NMR) is a property of atoms of certain elements whose nucleus is composed of an uneven number of protons and neutrons. Among such atoms are the ^{1}H-hydrogen atom, the ^{19}F-fluorine atom, and the ^{31}P-phosphorus atom (Koutcher and Burt, 1984). Due to a quantum-mechanical phenomenon these atoms generate small magnetic fields. Therefore, they are conceptually similar to bar magnets (Longmore, 1989). Exposed to strong magnetic fields, the atoms align along field lines of the magnetic field. But in contrast to bar magnets, not all atoms are oriented in the same direction within the external magnetic field. Rather, the atoms may be oriented parallel or antiparallel to the magnetic field. However, the atoms oriented in parallel exceed those oriented oppositely by a tiny fraction (Longmore, 1989; Van Geuns et al., 1999). Thus, the entirety of atoms generates a magnetic field by itself whose strength is dependent on the external magnetic field strength. The magnetic field due to this slight imbalance between orientations is very small, though, compared to the externally applied magnetic field and thus cannot be measured (Van Geuns et al., 1999). Still, elaborate manipulation of the magnetic field created by the atoms allows an amplification to a detectable level (McGowan, 2008). From this signal, MR images can be constructed. Virtually all MR-scans performed in routine patient care detect signal arising from hydrogen atoms due to their abundance within tissues (McMahon et al., 2011). In principle, though, any other atom exhibiting nuclear magnetic resonance can be used for image generation (Koutcher and Burt, 1984; Henderson, 1983).

^{19}F-MRI

The source of signal for ^{19}F MR imaging are fluorine atoms. However, the amount of fluorine inside most tissues is virtually zero. Therefore, ^{19}F imaging requires the administration of fluorine-containing contrast agents. The dependence of ^{19}F imaging on contrast administration has the advantage that it makes the ^{19}F MRI a highly specific imaging modality as any detectable signal is due to contrast agent accumulation (Flögel et al., 2008). Because resultant images only show the contrast agent, ^{19}F imaging is typically coupled with conventional ^{1}H-based imaging to relate the ^{19}F signal to anatomic structures seen on ^{1}H images (Rothe et al., 2019). Further, combination of ^{19}F contrast agents and Gadolinium is possible such that data derived from native ^{1}H imaging and from both contrast agents may be used for diagnostic purposes (Bönner et al., 2015).

The most commonly used contrast agents in ^{19}F imaging are Perfluorocarbons (PFC). PFC are hydrophobic fluorine-containing carbohydrates which can be administered intravenously after phospholipid nanoemulsification (Bouvain et al., 2020). A PFC suitable for clinical use is Perfluorooctylbromide (PFOB). Due to its ability to bind oxygen it has been evaluated as an artificial blood substitute in clinical trials and was shown to be safe for use in patients (Spahn et al., 2002). After intravenous administration in humans, PFOB nanoemulsions are phagocytosed almost exclusively by monocytes, with minor amounts being taken up by B-lymphocytes and neutrophils. PFOB then remains within the phagocytes without inducing any appreciable change in their function (Nienhaus et al., 2019). The lipid layer used for emulsification is gradually broken down after cellular uptake, allowing the hydrophobic PFOB to diffuse back into the blood where it is bound by plasma lipids. Thereby, PFOB is transported to the lungs and eliminated by exhalation. Its half-life is about 3-4 days (Spahn, 1999).

The reason why PFC-enhanced ^{19}F MR imaging has become a focus of research is due to the fact that PFC nanoparticles accumulate inside phagocytic cells after intravenous administration. By exploiting this property, specific visualization of inflammation is possible using the ^{19}F-MRI. As noted in Section 1.2.1, leukocytes from the circulation frequently enter inflammatory foci due to the local activation of endothelial cells. Thereby, the phagocytes carry the internalized PFC into the inflamed area and thus set the stage for ^{19}F imaging. It should be noted, though, that any tissue with a sufficient number of nanoparticle-loaded cells will become contrasted on ^{19}F imaging. Therefore, ^{19}F-signal can generally be observed in tissues harboring many phagocytic cells such as liver, spleen, lymphatic tissue, and bone marrow (Flögel et al., 2008). Thus, imaging these organs themselves or tissue closeby is challenging. Experimental studies in mice proved that various inflammatory conditions (including myocardial infarctions, pneumonia, graft rejection, and atherosclerosis) can be visualized with the ^{19}F MRI (Ebner et al., 2010; Flögel et al., 2011; Jacoby et al., 2014a; Van Heeswijk et al., 2015; Bouvain et al., 2020). While these results prove that it is in principle possible to detect many sources of inflammation, notice that these experiments were performed using special MR-scanners that generate magnetic field strengths of 9.4 T. Most clinical scanners in current use operate at 1.5 to 3 T. Therefore, translational studies are necessary to verify the findings at clinical field strengths.

In a pig model, it was shown that the inflammatory reaction after myocardial infarctions can be detected and localized by ^{19}F imaging both *ex vivo* and *in vivo* at 3 T (Bönner et al., 2015; Rothe et al., 2019; Bönner et al., 2022). Inflammation after myocardial infarction is intense, however (Frangogiannis, 2012). The capability of the ^{19}F MRI at 3 T to visualize smaller and less severely inflamed foci requires further research. A valuable future target for ^{19}F imaging would be atherosclerosis-associated inflammation. As noted in Section 1.2.2, a quantitative assessment of the inflammation within atheromas could be a means to determine the rupture risk of certain types of atherosclerotic plaques.

USPIO-enhanced MRI

A promising MRI-based approach to visualize atherosclerotic inflammation besides ^{19}F imaging makes use of ultrasmall paramagnetic particles of iron oxide (USPIO). In clinical research, it was possible to visualize carotid atherosclerosis using USPIO (Howarth et al., 2009; Trivedi et al., 2006). Similar to ^{19}F nanoparticles, USPIO accumulate inside monocytes/macrophages and are carried by these cells into foci of inflammation. These particles can be detected by MRI since they induce inhomogeneities inside the magnetic field that enhance T2-relaxation and thereby lead to hypointensities in the image (Makela et al., 2016). A major advantage of USPIO compared to ^{19}F nanoparticles is the higher sensitivity of MR-scanners for USPIO. In principle, single murine iron-loaded cells can be detected by MRI both *ex vivo* (Shapiro et al., 2007) and *in vivo* (Heyn et al., 2006). In these studies, however, larger iron oxide particles were used as the MRI sensitivity for larger particles is greater than for USPIO (Zarghami et al., 2018). Since some of these larger particles are not biodegradable (Makela et al., 2016), their use is limited to preclinical studies, though. In contrast, ~10^3-10^5 PFC loaded cells are necessary inside a given voxel for detection by ^{19}F MRI. The specific number is dependent on the amount of nanoparticles inside the cells (Makela et al., 2016). Bönner et al. (2022) report an *in vivo* detection threshold of 70000 cells/voxel at 3 T in a porcine model of myocardial infarction.

1.4 Histological Validation Concepts of Vascular Inflammation

The evaluation of the data generated in our experiments involved the extraction of a number of features from digital images. Therefore, below we provide a brief overview of the concepts underlying the methods used for feature extraction.

1.4.1 Digital Images

Digital images are composed of picture elements (pixels). A pixel is a small square located at a specific point in an image. Each pixel is associated with one or more numeric values encoding, for example, the color of the pixel. The alignment of all pixels in their respective locations yields a complete image.

Most of the images we analyzed were RGB-images. These are composed of three 8-bit channels that store red, green, and blue light intensities for each pixel. In most instances, the goal of any processing done on the images was the conversion of the RGB input into a binary output. Binary images are single channel images whose pixel values are either 0 or 1. These binary values ideally encode whether a pixel belongs into one of two classes.

1.4.2 Digital Image Processing

Digital image processing involves the deliberate alteration of pixel values to allow an easier or automated extraction of certain information from the image (Furness, 1997). Commonly, image segmentation is the goal of image processing. Image segmentation is a term that denotes the classification of pixels within an image. That is, each pixel is assigned to one of an arbitrary number of classes. Each class then contains those pixels that make up certain structures or objects within an image. Often, the last step of image segmentation is the thresholding of the image (described below). Forms of image processing relevant to image analyses presented in Section 2.2.3 are outlined next.

Color Deconvolution

The color deconvolution method was developed to determine the contribution of a distinct stain to each pixel in histological images (Ruifrok et al., 2001). Histological specimens are commonly stained with multiple dyes. These dyes bind to molecules (such as proteins or DNA) in a specimen. Different dyes may bind to molecules in the specimen which are so close to each other that the transmitted light in

brightfield microscopy contributes to a single pixel's value in the digital image. In that case, the amount to which each dye determines the pixel value is unknown. Color deconvolution attempts to separate the individual contributions of each of the dyes to the pixel's value.

Histological stained specimens constitute a light absorbing medium. Monochromatic light traveling through an absorbing medium satisfies Lambert-Beers' law (Van der Laak et al., 2000):

$$I(\lambda) = I(\lambda_0) * e^{-A*c(\lambda)} \tag{1}$$

That is, the intensity of the transmitted light ($I(\lambda)$) relative to the intensity of the light which entered the medium ($I(\lambda_0)$) is nonlinearly dependent on the amount of stain present per unit area of the specimen (A) and on a stain-specific wavelength dependent absorption factor ($c(\lambda)$). The intensity of the transmitted light then determines the RGB-values of the pixels in the digital image. Since the RGB-values depend on the concentration of the stain in a nonlinear way (the exponential part of Equation 1), the intensity values of the image cannot be used directly to separate different stains if they contribute to the RGB-value of a pixel (Ruifrok et al., 2001). Rearranging the above equation yields:

$$OD = -\ln \frac{I(\lambda)}{I(\lambda_0)} = A * c(\lambda) \tag{2}$$

where OD denotes the optic density of a channel. Since the OD is linearly dependent on the concentration of a stain, it can be used for separation of stains. The optic density of each stain and of each of the three channels (RGB) can be obtained experimentally by preparing microscopy slides stained with only one of the stains of interest. Plugging the incident light intensity and the measured transmitted light intensity for each channel into the above equation, yields channel specific ODs. The three optic densities for a given stain can be considered a 1x3 vector:

$$\begin{pmatrix} R_{\text{Stain 1}} & G_{\text{Stain 1}} & B_{\text{Stain 1}} \end{pmatrix}$$

Because the actual values of this vector depend on the amount of stain used while preparing the single stained slides, normalization is necessary. This is done by dividing all three components of the vector by its length. The color deconvolution algorithm proposed by Ruifrok et al. (2001) requires 3 such stain vectors (see below). For slides stained with three dyes, stain vectors can be determined for each of the dyes. If fewer dyes are used, one stain vector can be determined from unstained slides. After normalization of the three stain vectors, the following matrix can be set up:

$$\begin{bmatrix} \hat{R}_{\text{Stain 1}} & \hat{G}_{\text{Stain 1}} & \hat{B}_{\text{Stain 1}} \\ \hat{R}_{\text{Stain 2}} & \hat{G}_{\text{Stain 2}} & \hat{B}_{\text{Stain 2}} \\ \hat{R}_{\text{Stain 3}} & \hat{G}_{\text{Stain 3}} & \hat{B}_{\text{Stain 3}} \end{bmatrix}$$

After orthogonal transformation and inversion, multiplication of the matrix with a 3x1 vector containing the optic densities of the red, green, and blue channel at a given pixel as its elements yields the amount of individual stain present at this pixel. Since the matrix is multiplied with a 3x1 vector of RGB optic densities, a 3x3 matrix is required to return a 3x1 output. Therefore, three stain vectors are necessary.

As it allows the separation of stains, color deconvolution is a widely used tool for analysis of histological specimens (Haub and Meckel, 2015). Notice though, the theory of color deconvolution is based on Lambert-Beers' law which holds only under conditions of monochromatic light. This condition is usually not given on histopathological imaging and therefore, there can be significant error with the use of this method on histological specimens (Haub and Meckel, 2015). Still, comparison of manual scoring of carcinoma-specimens by pathologists with automated scoring using color deconvolution showed high correlations (Rizzardi et al., 2012). This indicates good performance of the method in light microscopy despite the fact that its theory is based on prerequisites that do not hold under polychromatic lighting conditions.

Thresholding

In image processing, thresholding denotes the conversion of images of certain types into binary images. In the case of an 8-bit image, it implies setting each pixels' value (ranging from 0 to 255) to either zero (black) or 1 (white). This involves finding a threshold which serves as the cutoff value for setting pixel values to 0 or 1. The goal of thresholding is to separate two classes of pixels. For that purpose, a suitable threshold has to be found.

Thresholding can be performed in numerous ways. A simple thresholding method could be to set all pixel values to zero if they exceed a given number (such as the mean of all pixel values), and otherwise set the pixel value to 1. Many sophisticated thresholding methods exist which use different approaches to determine a single threshold value, perform serial thresholdings, or apply local thresholds for smaller regions within an image. The theory that underlies such thresholding methods can be illustrated on histograms of the pixel values of images (Figure 1).

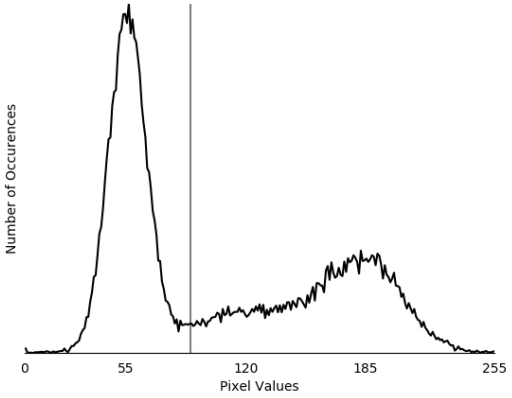

Figure 1: Image thresholding. Simulated histogram data with illustration of a potential threshold value (gray bar).

Thresholding methods attempt to identify populations of pixels and then determine thresholds that separate these populations best. In the Figure, the indicated threshold value separates the large cluster of pixels to the left of the threshold from the remainder of the pixels. Of notice, this single threshold is not capable of separating the second minor population of pixels in the right part of the histogram from the values lying in between the two populations. Thresholding being based on evaluation of histograms gives rise to an important issue: If the number of pixels belonging to a population is not sufficiently large to form a peak in the histogram, thresholding may not adequately assign these pixels to their respective populations. For example, from the histogram in the Figure it would be impossible to extract a population of pixels that lies within the major peak to the left of the indicated threshold. To allow segmentation in such cases, further image preprocessing may be necessary (Fisher et al.).

Image Convolutions Image convolutions are integral parts of convolutional neural networks (see Section 2.2.3). There are different types of convolutions. Convolutions relevant to our discussion include discrete convolutions and transpose convolutions. Convolutions constitute linear combinations of input data which is useful to identify both low- and high-level features inside the input data in a neural network. Dumoulin and Visin (2016) give an overview of convolutions and pooling operations.

To illustrate discrete convolutions, the left part of Figure 2 shows a 4x4 single channel image as an array of pixels (light blue). Performing a 3x3 convolution on this image involves sliding a 3x3 array (dark blue, called the kernel) over the image. In the Figure, the kernel starts in the upper left corner. With each stride, it moves one column rightwards until it gets to the last column. Then, it returns to the first column but moves down one row. This process continues in this fashion over the whole image. What happens during each stride of the kernel is that the values stored in the kernel are multiplied elementwise with the image's pixels values that the kernel is hovering over. The result is added up and stored inside an output array (shown in green). Thereby, a 3x3 convolution of an image yields an array with two fewer rows and columns than the input image. Below is a numeric example of a 3x3 convolution of a 4x4 image.

$$\begin{bmatrix} 26 & 30 \\ 12 & 12 \end{bmatrix} = \begin{bmatrix} 1 & 2 & 0 & 1 \\ 2 & 4 & 4 & 3 \\ 1 & 0 & 0 & 2 \\ 4 & 3 & 0 & 1 \end{bmatrix} conv \begin{bmatrix} 1 & 0 & 1 \\ 2 & 4 & 1 \\ 1 & 0 & 0 \end{bmatrix} \tag{3}$$

Features that can be changed in discrete convolutions include the *stride* and *padding*. In the example shown in the Figure, the kernel moves by one column or by one column and row with each stride. This is a stride of 1. Increasing the stride causes a greater size reduction of the output. Next, to avoid a size reduction of an image after a convolution, zero-padding may be added around the image. That is, if two rows and columns with value 0 are added symmetrically around the image (yielding a 6x6 image), a 3x3 convolution would return a 4x4 image and would thereby preserve input image size. To perform a discrete convolution on multichannel images, kernel size has to increase by one dimension. Thereby, a separate kernel can be slid over each of the channels, returning a separate output array. Typically, the pixel values of the output arrays are then added up elementwise.

Transpose convolutions can be considered the inverse operation of discrete convolutions. For example, a 3x3 discrete convolution of a 4x4 input yields a 2x2 output. To get from a 2x2 input to a 4x4 output, the transpose convolution is used. This is illustrated in Figure 2. Zero-padding the 2x2 input (shown in blue) with four rows and columns and convolving with a 3x3 kernel (gray) outputs a 4x4 array (green).

Pooling Operations Pooling is also used inside convolutional neural networks. Similarly to convolutions, it involves sliding a kernel over an input array. Kernel size and stride can also be chosen as desired. Depending on the type of pooling, different operations are executed on the values the kernel hoveres over. In the case of max pooling (Figure 3), the maximum value is stored inside the output array. Average pooling constitutes another example of a pooling operation. Padding of input is not a common feature in pooling operations since usually the goal of pooling is downsampling of the input (that is, a reduction of input size).

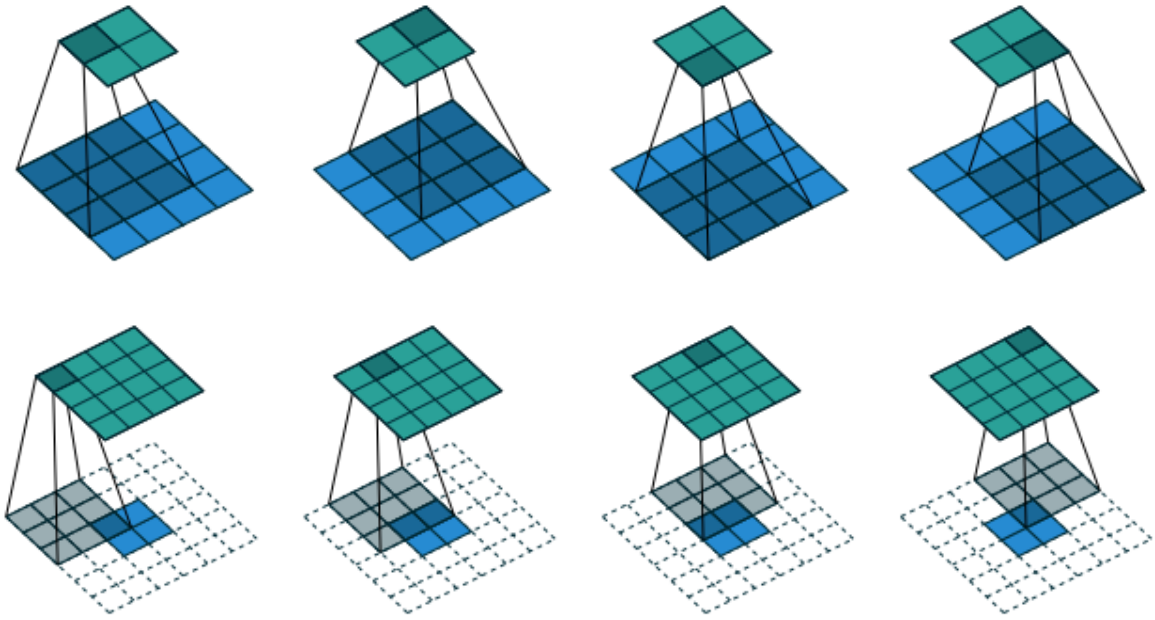

Figure 2: Image convolutions. A schematic discrete convolution is shown in the top row, a transpose convolution in the bottom row. Reproduced with permission from (Dumoulin and Visin, 2016).

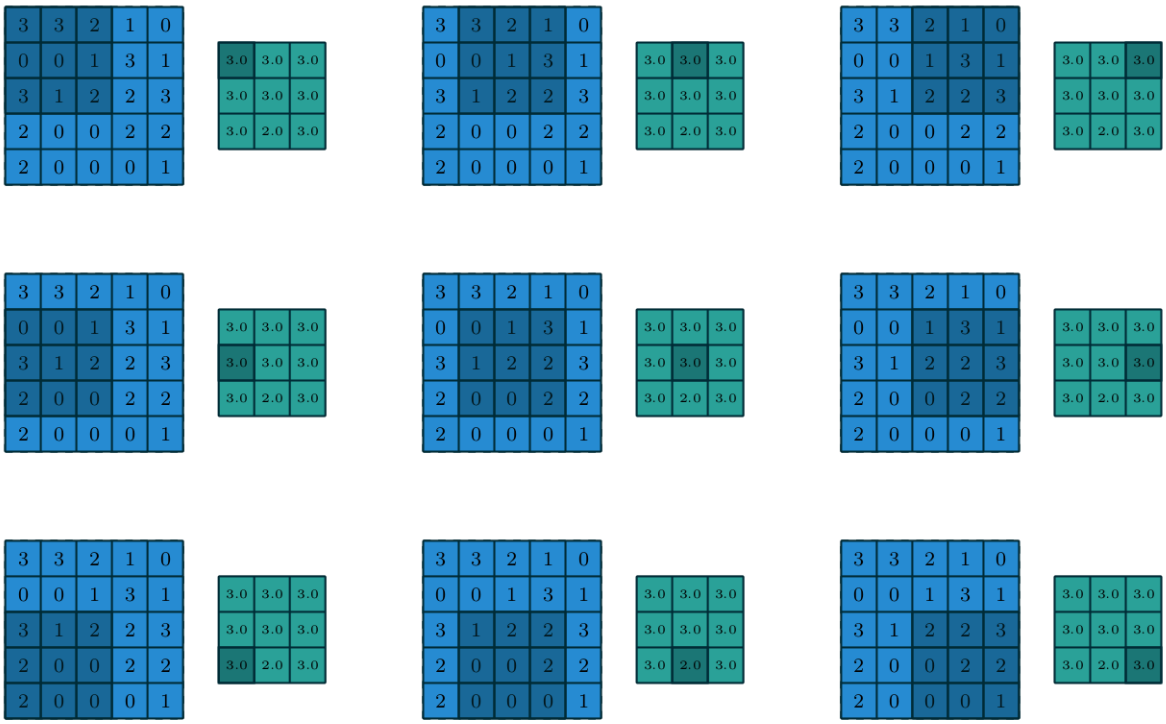

Figure 3: Max pooling. Shown is an example of the max pooling operation applied to a 5x5 image with a kernel of size 3x3. Reproduced with permission from (Dumoulin and Visin, 2016).

1.5 Central Hypothesis and Study Goals

As noted throughout this Section, clinicians currently do not have a non-invasive, widely available diagnostic tool at their disposal that would allow the detection of unstable atherosclerotic plaques in asymptomatic patients. Since high-risk plaques are associated with active inflammatory processes, the Perfluorocarbon contrast-enhanced ^{19}F MRI is a promising imaging modality for the above purpose because of its inflammation-sensitivity and -specificity. In order to determine whether the ^{19}F MRI can identify small sources of inflammation within blood vessel walls at clinical magnetic field strengths (3 T), we propose an experimental model of angioplasty-induced vascular inflammation. This model may serve as a proof of concept before investigating the ^{19}F MRI-based detection of inflammation within atherosclerotic plaques.

Thus, the central hypothesis was that the inflammatory response ensuing angioplasty of porcine carotid arteries can be detected by ^{19}F MR imaging. Further, we aim to find a quantitative relationship between the intensity of ^{19}F enhancement and the severity of inflammation as seen on histology.
We decomposed this goal into the following questions:
(1) What is the extent of vascular inflammation induced by carotid artery angioplasty as outlined in Section 2?
(2) What are the histopathologic signs of inflammation on a cellular level?
(3) Are there histopathologic signs of vascular remodeling?
(4) Is ^{19}F enhancement reflective of the severity of inflammation and of tissue infiltration by macrophages?
(5) What cell types mediate the transfer of Perfluorocarbon nanoparticles from the blood into the arterial wall?
These questions will guide through the following sections.

2 Material and Methods

2.1 Experimental Design

Experiments were performed in 8 Aachen mini pigs. The animals were treated in accordance with the national guidelines on animal care and were approved by the state authority "Landesamt für Natur-, Umwelt- und Verbraucherschutz"(file notes 84-02.04.2018.A154 and 81-02.04.2019.A379). All procedures occurred under inhalational anesthesia and involved a venipuncture for basic hematologic and metabolic panels as has been described previously (Rothe et al., 2019; Bönner et al., 2022).

Anesthesia and Analgesia

Pigs were fasted overnight before surgery. While in their quarters, pigs were sedated with Stresnil®(5 mg/kg BW IM, Elanco Lilly Deutschland GmbH, Bad Homburg, Germany) followed by Ketamin (10 mg/kg BW IM, Ketaset Zoetis, Berlin, Germany) and Atropinsulfat (0.5 mg IM, Braun, Melsungen, Germany) with an additional dosage of Diazepam (10 mg IM, Ratiopharm GmbH, Ulm, Germany). After 10-20 minutes a cannula was introduced into a superficial vein of the ear and complete anesthesia was induced with sodium thiopental (4 mg/kg IV initially and then demanding on effect, Rotexmedica GmbH, Trittau, Germany). Orotracheal intubation of the pigs was performed using a size-matched tube (7.5-8.5 mm tube) with pigs being in supine position. Anesthesia was maintained with a mixture of isoflurane (1.5-2.0 Vol%, Piramal Critical Care Deutschland GmbH, Hallbergmoos, Germany) solved in 100% oxygen. Pigs were ventilated with a respirator (Sulla 808 V, Dräger, Lübeck, Germany) at a rate of 10 to 12 breaths per minute, tidal volume was 450 ml (range 400-550 ml). For cooling protection, the animals were positioned in supine position on a heating mat on the operating table. Biomonitoring was assured by continuous monitoring of ECG, blood pressure, oxygen saturation (Monitor Eagle 4000, Marquette Heilige GmbH, Freiburg, Germany) and intermittent analysis of arterial blood gases. To maintain, preload stability, normal saline (2 mL/kg hourly, Braun, Melsungen, Germany) was infused through the venous cannula in the auricular vein during surgery. Every 20 to 30 minutes the pigs received a bolus of Fentanyl thereby maintaining analgesia (0.0075 mg, Rotexmedica GmbH, Trittau, Germany).

Model of Vascular Injury

The pigs were assigned at random into two subgroups: a mild (n=4) and a severe injury (n=4) group. Vascular injury was induced in all animals in the left or the right carotid artery with either a combination of Fogarty balloon denudation and balloon oversize injury modified according to previous protocols (Granada et al., 2011; Ishii et al., 2006; Busnelli et al., 2013, 2009) (severe injury) or with balloon oversize injury alone (mild injury). In detail, the femoral artery was exposed by surgical incision and preparation under sterile conditions. A 6F introducer sheath was inserted into the artery followed by administration of a heparin bolus (100 IU/kg). A guidewire (Emerald Guidewires 260 cm 0.032 inch, Cordis, Santa Clara, CA, USA) was placed in the carotid artery trunk and pre-injury carotid angiography was obtained by rapid administration of a iodine-containing contrast agent (Accupaque, General Electronic Healthcare, Solingen, Germany) using a 6F JR 4.0 SH guiding catheter (Medtronic, Inc., Minneapolis, MN, USA). In the severe injury subgroup, a 10 mm Fogarty over-the-wire embolectomy catheter (LeMaitre Vascular Inc., Burlington, MA, USA) was placed in one of the carotid arteries about 5 cm above the carotid artery trunk. The Fogarty balloon was then fully inflated and endothelial denudation was performed five times in a row by pulling the inflated balloon down to the carotid artery trunk. Afterwards, a Passeo 35 over-the-wire angioplasty balloon (10/40 mm, Biotronik, Berlin, Germany) was placed in the denudated area and oversize injury was performed three times in a row by fully inflation of the balloon to 7 atm for each 5 minutes. Treatment in the mild injury group was limited to inflating the

angioplasty balloon three times. Post-injury angiography was obtained again as described above. After surgery all external material was removed and the wound was closed.

Production of PFOB-Nanoemulsion

PFOB-NE was prepared as described elsewhere (Flögel et al., 2008; Bönner et al., 2015; Jacoby et al., 2014b). Briefly, 18.369 g purified egg lecithin (E 80 S, 4% wt/wt, Lipoid GmbH, Ludwigshafen, Germany) was dispersed in 284.508 g phosphate buffer (10 mM, pH 7.4) with 2.5% Glycerol by magnetic stirring at room temperature. Then 322 g PFOB (AtoChem, Puteaux, France) was added. Emulsions were stabilized by adding a semifluorinated alkane, which is a mixed fluorocarbon/hydrocarbon diblock compound (C6F13C10H21, F6H10) equimolar to the E 80 S lipid. Afterwards, the dispersion was pretreated with a high-performance disperser (T18 basic ULTRA TURRAX, IKA Werke GmbH & CO. KG, Staufen, Germany) at 14000 rpm for 2 minutes. This pre-emulsion was further emulsified by high-pressure/shear homogenization (1000 bar, 30 minutes) using a microfluidizer (Microfluidizer M110P, Microfluidics Corp., Newton, MA, USA). Particle size was determined using photon correlation spectroscopy (PCS) on a Zetatrac (Betatek, Toronto, Canada) device. Afterwards, the NE was autoclaved (30 minutes at 121°C) using a program to autoclave pure liquids and stored at 4°C.

Application of PFOB-Nanoemulsion

At day 3 after vascular injury a body weight adjusted volume of PFOB-NE (5 ml/kg body weight) was administered intravenously. For that purpose, pigs were anesthetized again as described above. PFOB-NE was infused via a cannula placed in a superficial ear vein with an infusion rate of 80-150 ml/h. Up to 24 hours after the infusion, animals were checked for any side effects (increased breathing, vomitus, or other signs of an allergic reaction).

Invasive Assessment of Vascular Injury

At day 6 after surgery, carotid artery injury was assessed invasively by angiography and intravascular ultrasound (IVUS). Again, pigs were anesthetized and angiographic images of the carotid arteries were obtained as described above. The degree of carotid artery stenosis was determined by calculation of diameter stenosis. Blood flow was assessed visually. Afterwards, an IVUS catheter was introduced into the carotid artery via a 0.035 in balanced middleweight (BMW) guidewire (Abbott Laboratories, Chicago, Illinois, USA). IVUS and colour flow IVUS was performed in both the injured and the non-injured artery. Lumen size and neointima thickness was measured. Blood flow and wall abnormalities were analyzed visually.

^{1}H and ^{19}F Cardiac Magnetic Resonance (CMR)

For cardiovascular magnetic resonance (CMR), pigs were anesthetized as described above. Anesthesia was maintained with a mixture of isoflurane (1.5 2.0% v/v, Piramal Critical Care Deutschland GmbH, Hallbergmoos, Germany) dissolved in 100% oxygen. Adequate anesthesia was monitored by testing the interclaw reflex. During CMR, heart rate was monitored. When necessary, additional anesthesia was provided by administering fentanyl (7.5 µg every 30 minutes, Rotexmedica GmbH, Trittau, Germany) or ketamine (Ketaset 100 mg/ml, Zoetis, Berlin, Germany). CMR was performed at day 6 after vessel injury using a whole-body 3.0 T Achieva X-series MR scanner (Philips Healthcare, Best, the Netherlands). In vivo CMR was performed according to previously established animal handling, anesthetic and CMR workflow protocols (Bönner et al., 2015; Jacoby et al., 2014b). For ^{1}H measurements two flexible double array surface coils of 14 x 17 cm and 20 cm diameter (SENSE Flex M and SENSE Flex L surface coil, Philips Healthcare, Best, the Netherlands) were used. The CMR scan consisted of a ^{1}H protocol including contrast enhanced angiography, phase-contrast velocity encoded (VENC) measurements, and

high-resolution T2-weighted black blood sequences for vessel wall assessment.

Angiography of the carotid arteries was performed using a three-dimensional (3D) turbo spin-echo (TSE) during systole and diastole periods. TSE TRANCE imaging was performed using the following parameters: repetition time (TR), 1 beat; echo time (TE), shortest; flip angle, 90°. Furthermore, segmented gradient-echo phase contrast CMR (PC-CMR) was performed at the proximal, middle and distal part of the carotid artery. The velocity encoding range was set at 150 cm/s in a through-plane direction. After acquisition of ^{1}H reference scans, the pigs were removed from the magnet bore without losing the isocenter information, and the ^{19}F coil was placed on the chest between sternum and the left leg. Thereafter, pigs were repositioned into the scanner at the same isocenter position, which was confirmed by repeating ^{1}H reference scans. ^{19}F imaging was performed using a balanced Fast Field Echo (bFFE) sequence with steady state free precession read-out, as described in a previous applicability study (Rothe et al., 2019).

After *in vivo* CMR scans were accomplished, pigs were sacrificed inside the scanner with potassium chloride and an overdose of pentobarbital (Narcoren, Boehringer Ingelheim, Ingelheim am Rhein, Germany). Heparin (10000 I.E. Heparin-Natrium 25000, Ratiopharm GmbH, Ulm, Germany) was injected to prevent coagulation. Thereafter, in situ scans were made including a high resolution ^{1}H 3D Scan and the same ^{19}F protocol as above. These *in situ* acquisitions were performed to exclude signal loss or signal spill-over due to cardiac movements and different image resolutions.

Analysis of CMR Datasets

^{1}H MR angiography of carotid arteries as well as ^{19}F images and ^{1}H/^{19}F overlay were visualized using Horos^{TM} version 3.3.6 (Horos project, Annapolis, MD, USA). Carotid artery flow was assessed by Q flow MR images and automatically analyzed using Circle CVI 42 version 5.11 (Circle Cardiovascular Imaging Inc., Calgary, AB, Canada). For calculation of ^{19}F Signal to noise ratio (SNR) *in vivo*, all slices with ^{19}F signal were included into the analysis. In every slice, SNR was calculated from the ratio of the mean of a region of interest (ROI) and the standard deviation of the noise of a ROI in a different slice located beside any tissue of the same data set. *In vivo* SNR was then calculated as the mean SNR of every slice included into the calculation.

For *ex vivo* assessment of ^{19}F signal intensity, SNR was calculated for every cross-sectional image as the mean of a region of interest (ROI) and the standard deviation of the noise of a ROI in a different slice located beside any tissue of the same data set. Distance from bifurcation was obtained simultaneously and a profile of ^{19}F SNR in dependence of slice location was plotted.

2.2 Histology

2.2.1 Specimen Preparation

Both carotid arteries and the carotid trunk were excised *in toto* and stored in 4% paraformaldehyde (PFA). Notice here, that there is a difference between local porcine and human anatomy that is relevant to our discussion: In pigs, a single carotid trunk branches off from the aorta, termed the *common carotid artery*. A short distance downstream (some centimeters), at the carotid bifurcation, the trunk splits into a left and right carotid artery. Each of these vessels in turn branches into an internal and external carotid. Thus, throughout this text, the term *carotid bifurcation* denotes the site of separation of the common carotid artery into the left and right carotid artery. After PFA-incubation for at least 7 days, the carotid arteries underwent *ex vivo* ^{19}F scans. The arteries were then cut in short axial slices with a medium thickness of 5 mm. The mean length of the explanted arterial segments was 78.7 mm (minimal length: 48 mm, maximal length: 110 mm). In general, regarding the treated carotids, the length of the vessel segment exceeded the longitudinal extent of injury to the artery. That is, these vessels were composed of

a catheter-exposed part located close to the bifurcation and a more distal part untouched by the catheter. Thereafter, slices were embedded in paraffin. The sections of one pig were marked with a surgical suture (size 10-0) at the top. Thereby, specimens could be embedded into paraffin-blocks with preservation of orientation. That is, the parts of the sections pointing in the same direction in each paraffin-block also pointed in the same direction in the intact vessel. Embedding the sections in orientation allowed three-dimensional reconstruction of cell densities in the vessel wall (see Section 3.4). For further histological processing, sections of 4 µm thickness were cut with a microtome (Jung Biocut 2035, Mikrotom, Leica Instruments GmbH, Nussloch, Germany).

2.2.2 Staining Procedures

Hematoxylin & Eosin Staining

The Hematoxylin & Eosin stain is a standard stain based on the components Hematoxylin and Eosin. Hematoxylin is a blue-colored cationic stain which binds to negatively charged components inside a specimen (especially phosphate groups of DNA and RNA) and therefore causes these components (predominantly the nuclei of cells) to take on a blue color. Eosin is a red-colored, negatively charged acidic stain which binds cationic groups of proteins (mainly Lysine, Arginine, and Histidine) found in the cellular cytoplasm.

Protocol:

Step 1: Heat sections at 60°C; 30 minutes

Step 2: Deparaffinize in xylene or substitute media (ROTICLEAR®, Carl Roth GmbH & Co.KG, Karlsruhe, Germany); two changes; 5 minutes each

Step 3: Rehydrate in Ethanol or Isopropanol of descending concentration (100%, 100%, 96%, 70%; 5 Minutes, 5 Minutes, 3 Minutes, 3 minutes, respectively)

Step 4: Transfer into deionized water; 5 minutes

Step 5: Nuclear staining in Gill's 2 Hematoxylin (Carl Roth GmbH & Co.KG, Karlsruhe, Germany); 1 minute

Step 6: Transfer into deionized water; 5 seconds

Step 7: Differentiate in 0.1% hydrochloric acid solution (Merck KGaA, Darmstadt, Germany) to prevent overstaining; 2 seconds

Step 8: Rinse in running tap water for bluing; 1 minute

Step 9: Cytoplasmic staining in 0.5% Eosin (Carl Roth GmbH & Co.KG, Karlsruhe, Germany); 1 minute

Step 10: Dehydrate in Ethanol or Isopropanol of ascending concentration (70%, 96%, 100%, 100%); 1 minute each

Step 11: Dehydrate in xylene or substitute media (ROTICLEAR®); two changes; 10 minutes each

Step 12: Coverslip slides with an organic mounting agent (ROTI®Histokitt, Carl Roth GmbH & Co.KG, Karlsruhe, Germany)

Immunohistochemical Staining

Immunohistochemical staining (IHC) makes use of antibodies (immunoglobulins) to specifically stain certain cells or molecules as determined by the specificity of the antibody. Antibodies are glycoproteins produced by B-lymphocyte derived plasma cells and are an integral part of an organism's defense against pathogens. Immunoglobulins exert their effect by binding to proteins, refered to as antigens, which, for example, can be located on an invading microorganism but also on host cells. Importantly, most immunoglobulins bind only a few protein structures with high affinity allowing them to selectively adhere to these structures. This feature can be exploited for IHC staining: Antibodies directed against antigens located on cells or structures of interest are introduced onto tissue sections whereby their target-antigens are tagged with the antibody. Different techniques exist to visualize the binding of the immunoglobulin to an antigen on a tissue section. Reviews of the underlying principles of IHC and examples of the procedure can be found in Hofman (2002) and Hsu et al. (1981).

In brief, enzymes that convert chromogenic substrates can be directly attached to or brought into contact with antibodies that bind the antigen of interest. After introducing the antibody and the mentioned substrate onto tissue sections, the antibody-associated enzymes convert the substrate such that it becomes visible on light microscopy. In addition, this process causes the substrate to precipitate at the site of conversion. Thereby, antibody-bound cells are stained specifically. The strength of cell staining depends on the amount of substrate that is converted by the enzyme. Substrate conversion and precipitation that occurs at sites remote from antibody binding leads to background staining. Depending on the employed technique, the sensitivity (staining intensity) and specificity (background staining) of the method may vary.

In our experiments, the Antibody-Biotin-Complex (ABC) technique was used due to its high sensitivity (Hofman, 2002). We used antibodies directed against CD163 to identify monocytes/macrophages by IHC. CD163 is a marker restricted to monocytes/macrophages. It is a scavenger receptor associated with the internalization of haptoglobin-hemoglobin complexes. It is hypothesized to have anti-inflammatory effects by removing these complexes and by inducing the anti-oxidative enzyme heme oxygenase-1. Expression of CD163 is regulated by cytokines such as IL-10 and Macrophage colony stimulating factor. One of the most commonly used markers for IHC-based detection of macrophages is CD68 (Virmani et al., 2006a; Howard et al., 2015; Zheng et al., 2019). Because of differences in antigenic structures between species, the commercially available antibodies directed against CD68 did not bind the porcine CD68 antigens in our study. Therefore, we used CD163 as an alternative marker to delineate macrophages in tissue sections.

Protocol:

Step 1: Heat sections at 40°C; 20 minutes

Step 2: Deparaffinize in xylene or substitute media (ROTICLEAR®, Carl Roth GmbH & Co.KG, Karlsruhe, Germany); two changes; 5 minutes each

Step 3: Rehydrate in Ethanol or Isopropanol of descending concentration (100%, 100%, 96%, 70%; 5 minutes, 5 minutes, 3 minutes, 3 minutes, respectively)

Step 4: Transfer into deionized water; 5 minutes

Step 5: Antigen retrieval: Place slides in plastic Coplin jar filled (9:1) with deionized water and antigen retrieval solution (Invitrogen™ eBioscience™ IHC Antigen Retrieval Solution - High pH (10x), Fisher Scientific GmbH, Schwerte, Germany); heat slides in pressure cooker to 100°C for 10 minutes; turn down heat to 80°C; heat for another 20 minutes

Step 6: Rinse in tap water; 1 minute

Step 7: Place slides in Dulbecco's phosphate buffered saline (PBS) (Sigma-Aldrich Chemie GmbH, Taufkirchen, Germany); two changes; 5 minutes each

Step 8: Block non-specific binding: Place slides in 3.5% H_2O_2 (Carl Roth GmbH & Co.KG, Karlsruhe, Germany) in PBS; 20 minutes

Step 9: Place slides in PBS; 5 minutes

Step 10: Place slides in a humidified chamber

Step 11: Cover first half of the specimens with 50 µl of 1% primary antibody (Clone EDHu-1, 1 mg/ml, Novus Biologicals LLC, Centennial, CO, USA) in PBS

Step 12: Cover second half of the specimens with 50 µl of 0.285% control antibody (kappa isotype) (Vector Laboratories Inc., Burlingame, CA, USA) in PBS

Step 13: Incubate slides in the humidified chamber; 1 hour

Step 14: Place slides in PBS; two changes; 5 minutes each

Step 15: Place slides in the humidified chamber

Step 16: Cover specimens with 50 µl of 0.4% secondary antibody (Vector Laboratories Inc., Burlingame, CA, USA) in PBS

Step 17: Incubate slides in the humidified chamber; 40 minutes

Step 18: Place slides in PBS; two changes; 5 minutes each

Step 19: Place slides in the humidified chamber

Step 20: Cover specimens with 50 µl of 0.125% Horseradish Peroxidase conjugated Streptavidin (Vector Laboratories Inc., Burlingame, CA, USA) in PBS

Step 21: Incubate slides in the humidified chamber; 35 minutes

Step 22: Place slides in PBS; two changes; 5 minutes each

Step 23: Place slides in the humidified chamber

Step 24: Cover specimens with 50 µl AEC (AEC Substrate Kit ab64252, Abcam plc., Cambridge, UK)

Step 25: Incubate slides while observing a slide under a microscope for red-staining cells

Step 26: Once cells become visible, place slides in tap water

Step 27: Place slides in Gill's 2 Hematoxylin (Carl Roth GmbH & Co.KG, Karlsruhe, Germany); 5 seconds

Step 28: Place slides in water for bluing; 3 minutes

Step 29: Place slides in water for bluing; three changes; 1 minute each

Step 30: Coverslip slides with an aequeous mounting agent (VectaMount® AQ Mounting Medium, Vector Laboratories Inc., Burlingame, CA, USA)

2.2.3 Microscopic Analysis

Microscopic analysis of slides and acquisition of images was performed using the Leica Dm 4000 M microscope (Leica Microsystems GmBH, Wetzlar, Germany) and the Leica application suite X software. The following analyses were done on all sections of all pigs.

Assessment of Thickness of Vessel Wall Segments

In most instances, microscopic sections were too large to fit into a single field of view of the microscope's camera. To obtain a digital image of the sections as a whole, multiple images at 25-fold magnification (25x) were captured from H&E stained slides. These images were stitched into a single image showing the whole vessel segment at 25x. Stitching was performed with the ImageJ software (Schneider et al., 2012) using the MosaicJ plugin (Thévenaz and Unser, 2007). At 25x, three of the four components of the artery were easily discernible: The adventitia, media, and lumen. The intima could not be reliably distinguished at this magnification. The outer margins of adventitia, media, and lumen were manually encircled using ImageJ. An approximation of the thickness of adventitia, media, and lumen was made based on the measured areas.

To determine the intimal thickness, images of the intima were obtained at 400x or 500x from each quadrant of the vessel wall. Intimal thickness was measured at three points in each image using ImageJ. The mean of these three measurements was used as an estimate of the intimal thickness for each image.

Assessment of Overall Cell Counts

Overall cell counts were evaluated on H&E stained specimens. 200x images were captured at either 4 or 8 locations of the media and adventitia. Four images were analyzed in most pigs. In this case, one image was taken of each quadrant (black squares in Figure 4).Of the one pig, whose specimens were embedded in orientation, eight images were obtained for three-dimensional reconstructions (see sections 2.2.1 and 3.4). Here, one image of each octant was taken (black and red squares in Figure 4). In these images, the cell count was determined using the Fiji distribution (version 2.0, Schindelin et al., 2012) of ImageJ by counting up the number of Hematoxylin-stained nuclei. Automated cell counting was performed using Fiji-functions. Results were evaluated by visual inspection of the count. The general outline of the approach to automate cell counting is summarized next. Principles underlying the image analyses can be found in Section 1.4. In the following descriptions, text in Sans Serif style denotes ImageJ functions and tools; text in *italics* is used for image files opened in Fiji.

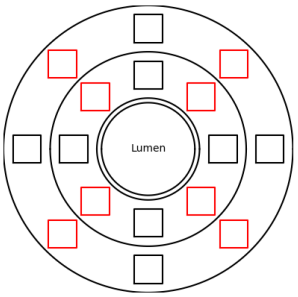

Figure 4: Sites of image acquisition.

Step 1: Load image into Fiji (*Image 0*)

Step 2: Run Color Deconvolution with the preset H&E deconvolution matrix. This outputs three images: *Image 1*, *Image 2*, *Image 3*. The pixel values of *Image 1* approximate the contribution of Hematoxylin staining to each pixel in *Image 0*. The pixel values of *Image 2* approximate the contribution of Eosin staining to each pixel in *Image 0*. The pixel values of *Image 3* approximate the contribution of background staining to each pixel in *Image 0*.

Step 3: Run Auto Threshold (Landini et al.) on *Image 1*; select an appropriate thresholding method beforehand by visual inspection. This function yields a binary image.

Step 4: Run Analyze Particles on the binary image. Size and circularity restrictions are chosen such that nuclei in the *Image 0* are counted best. Analyze Particles is used to measure the absolute number of

nuclei, the number of nuclei per square millimeter, the fraction of the whole image-area covered by the nuclei, and the area in square millimeters covered by the stained nuclei.

Assessment of CD163$^+$ Cell Counts

The number of CD163$^+$ macrophages was assessed by IHC. As for H&E stained sections, 200x images were taken from each quadrant or octant of the adventitia and media. A neural network based method was used to analyze cell counts in IHC slides. A brief outline of the internal workings of the network is given next. For a more detailed description, we refer the reader to Gurney (2018) and Stevens et al. (2020) in addition to the literature cited below.

The reason, a neural network based approach was chosen, is that these networks can approximate highly non-linear functions. The underlying assumption is, that the probability that an image's pixel belongs into a certain class (such as CD163$^+$ or CD163$^-$) is characterized by a function. Since this function is unknown, a method is needed for its approximation which is provided by the neural network.

Because this section is about the analysis of RGB images, the following description details the mechanics of neural networks with regards to RGB image data. But with appropriate modifications, the description is also applicable to any other input data type. As noted in Section 1.4, an image consists of pixels with each pixel storing three intensity values (for red, green, and blue). A simple means to input these values into a neural network would be to flatten the pixel values into a single vector as shown in Equation 4. The basic building block of a neural network is called a perceptron. A perceptron has an input which it manipulates, and generates an output. In our case, a perceptron may receive the flattened vector of an image as input. Manipulation of the input data involves calculating a linear combination of the input vector. That is, each component of the vector is multiplied by a weight and then all the resultant products are added up (amounts to calculating the scalar product). Finally, a so-called bias is added (Equation 4). Importantly, the resultant value is not the output of the perceptron yet. This is due to the fact that performing a linear combination of the input data only allows for modeling of linear functions. To introduce the necessary non-linearity, the computed value is passed into a non-linear function (the activation function) which returns the output of the perceptron. A full neural network consists of multiple layers composed of multiple perceptrons.

$$y = bias + \begin{pmatrix} w_1 \\ w_2 \\ w_3 \\ ... \\ ... \\ ... \\ w_n - 2 \\ w_n - 1 \\ w_n \end{pmatrix} \bullet \begin{pmatrix} R_1 \\ G_1 \\ B_1 \\ ... \\ ... \\ ... \\ R_n \\ G_n \\ B_n \end{pmatrix} \tag{4}$$

The way a neural network approximates the mentioned function which is able to transform input images into a desired output is by computing linear combinations of the data with the *right* set of weights. But since the function is unknown, this particular set of weights is also unknown initially. Therefore, networks require a training phase to determine the necessary set of weights. Often networks are intialized with random weights. Training the network then involves iteratively passing data into the network, calculating the output of the network using the current set of weights, and comparing this output to the desired output which has to be provided to the network during the training phase. The process of comparing the calculated to desired output involves computing a value termed *loss*. An appropriate method needs to be chosen to calculate a meaningful loss. Then, the weights in the neural network are automatically

optimized to reduce the loss. Given sufficient data to train on, often the loss can be minimized to obtain a set of weights which approximates the underlying function as closely as possible.

There are a number of factors to consider regarding the above description of the training process of a network. First, this process is not guaranteed to minimize the loss. Second, optimization of weights occurs with respect to the data input during training. If there is a major difference between training data and the data the model is supposed to analyze, the network's output may be far from the desired output. Third, optimization of weights can occur to an extent that ever more features of the training data are included in the optimization of the weights. But if these features are not general features of the data that is fed to the model but rather only occur in the training data, then an overoptimization regarding the training data ensues with reduced performance on other input data. This is termed *overfitting*.

Based on the function the network is supposed to perform, different architectures exist. These architectures determine the calculations that run inside the model. Here, images were analyzed via a convolutional neural network. The architecture of the network is known as *Unet* and was first published in 2015 by Ronneberg et al.. It proved to be a competition winning image segmentation architecture. The high-level structure of *Unet* is shown in Figure 5. It performs a number of convolutions on an input image. A convolution is a special linear combination of the input data which can be of different types (see Section 1.4). The values stored inside the convolution matrix serve as the weights of the convolutional neural network. In brief, Unet performs serial 3x3 convolutions followed by applying the non-linear activation function (ReLU in the figure). After two of these convolutions max pooling is used for downsampling. Notice that 64 convolutions with 64 different sets of weights occur in each of these steps. *Unet* repeats these operations four times, after which it starts upsampling the data using transpose convolutions. So called skip connections add less convolved representations of the data to the output of the transpose convolution. Training a *Unet* based network leads to an optimization of the weights which ultimately allows the detection of structures of interest in an image.

Implementation of *Unet* was done using the Pytorch module (Paszke et al., 2017) for Python (see Section 6.1). The model was trained on 18 images which were segmented by hand ($CD163^+$ cells were colored in black, the remainder of the image was colored white). Since input image size was too large to fit into a single model, images were split into subparts 500 x 500 pixels in size. Because width and height of input images were not multiples of 500 white padding was added symmetrically around the images to allow the splitting up into subparts as outlined above. After training, RGB images 500 x 500 pixels in size could be fed into the model. The resultant output was an 8-bit grayscale image. The intensity of the grayscale values can be interpreted as a probability that a given pixel belongs into one of the classes in question.

The 8-bit layout of the *Unet* output required a final conversion into a binary image such that each of the two classes ($CD163^+$ and $CD163^-$) was mapped to black or white. The threshold for binary conversion was determined using one of Fiji's Auto Thresholds. Thereafter, cell counting was performed on the binary images. This, again, involved the Analyze Particles function of Fiji as outlined for H&E stained cells. Figure 6 gives an example of cell counting output by the neural network.

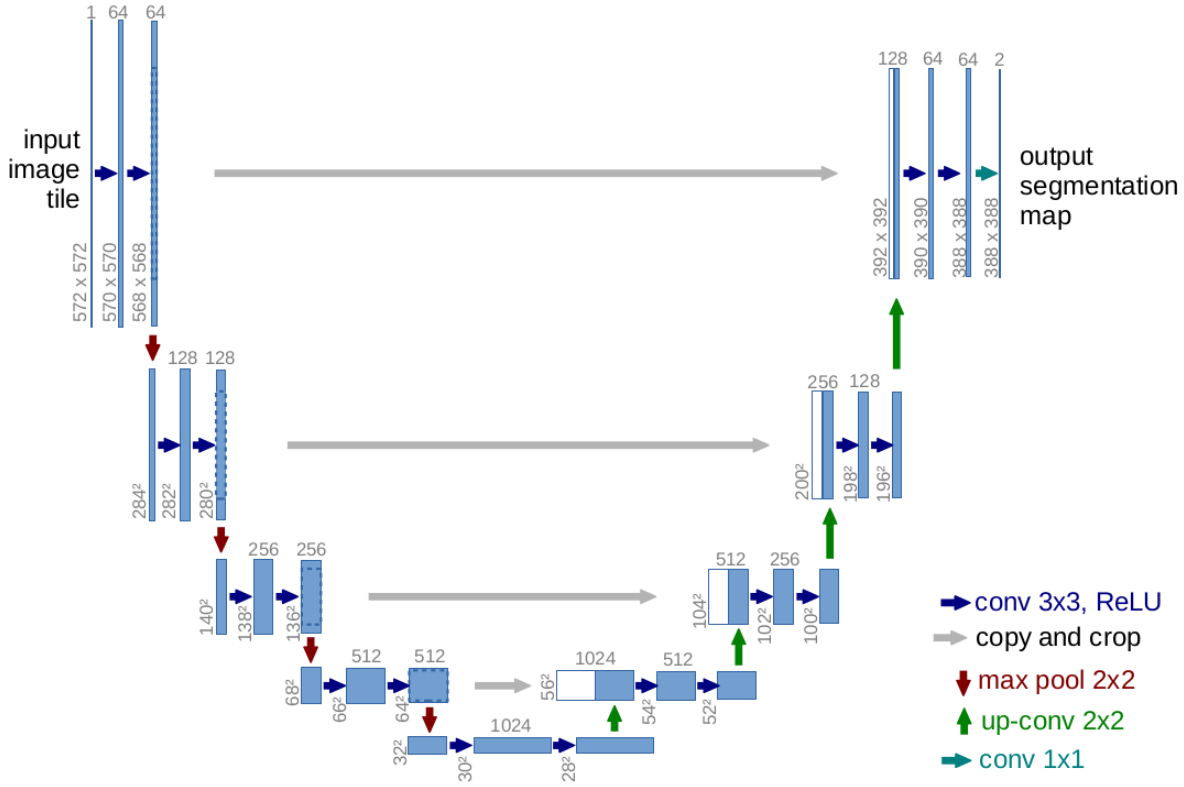

Figure 5: Unet architecture. The figure schematically shows the operations that are performed on input data within a Unet neural network (reproduced with permission from Ronneberg et al., 2015).

2.3 Flow Cytometry

2.3.1 Principles

Flow cytometry is a method that can be used to quantify and characterize cells. Internally, a flow cytometer performs hydrodynamic focusing of cells and laser-based measurements. Hydrodynamic focusing is a process in which cells are brought into motion within a tube. The diameter of the tube becomes continuously smaller which elicits a lining-up of cells. Each cell in the line is then exposed to the laser beam individually.

The most basic measurements performed in a flow cytometer are *Forward Scatter* (FSC) and *Side Scatter* (SSC) measurements. Scatter is the result of the diffraction of the laser beam when it hits molecules on and within a cell. The light can be diffracted in different directions. Light diffracted in a more forward direction hits a detector which measures the FSC, whereas light diffracted more to the side hits the SSC-detector. FSC is a rough approximation of a cell's size, SSC is a surrogate for a cell's granularity.

Additionally, modern flow cytometers contain further lasers which can excite certain fluorescent probes. These lasers striking the fluorescent probes causes an excitation of the probe and subsequent emission of light of a specific range of wavelengths. Detection of the emitted light indicates that a certain fluorescent probe passed through the cytometer. Moreover, the intensity of the emitted light correlates with the amount of probe that passed through. Attaching such fluorescent probes to antibodies or nanoparticles allows the morphologic and functional characterization of different cell types. For that purpose, cells are incubated with antibodies or nanoparticles labeled with a fluorescent probe. Binding of antibodies to a cell or phagocytosis of nanoparticles by a cell tags the cell with the probe. Thereby,

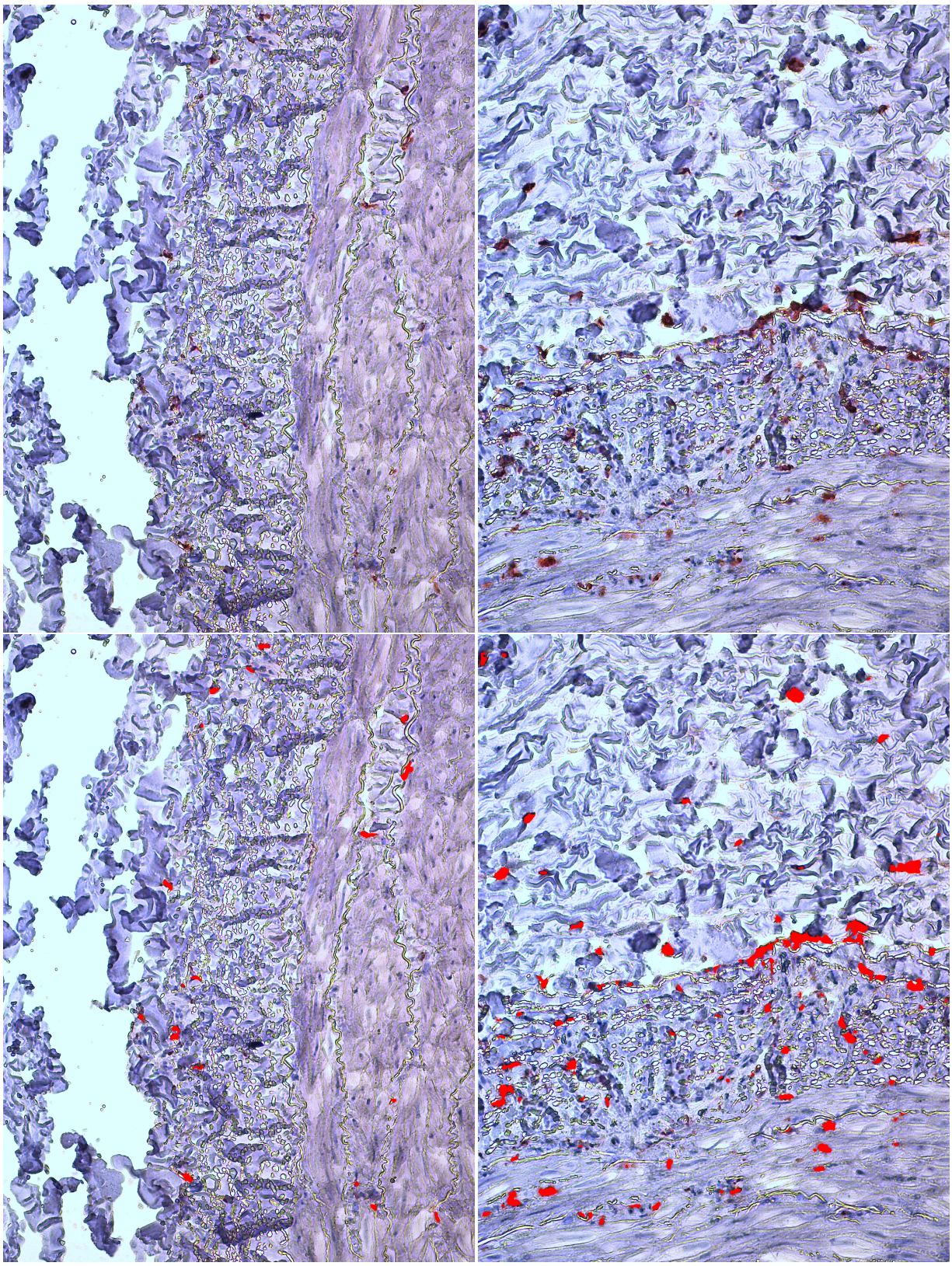

Figure 6: Unet-based cell counting. Shown are the adventitia and outermost part of the media in two sections of the same vessel; $CD163^+$ cells are stained red (upper panel). The cell count output by the neural network with counted cells highlighted in red (lower panel). Magnification 200-fold.

the flow cytometer can determine the amount of probe associated with each cell passing through. In the experiments outlined below, porcine blood was incubated with Perfluorocarbon (PFC) nanoparticles which were labeled with the FITC fluorochrome. The amount of nanoparticles taken up by blood cells

could then be inferred via flow cytometry.

2.3.2 Specimens

In our study, the phagocytic uptake of PFCs into peripheral blood leukocytes was evaluated by flow cytometry. We restricted the analysis to leukocytes because of their mechanistic relevance to the experiment: PFCs are transported into foci of inflammation inside leukocytes (see Section 1.3.3). Recruitment of leukocytes to these foci is induced by mediators of inflammation such as those released after angioplasty (Section 1.2.3). Blood samples of the pigs undergoing carotid angioplasty were measured at four time points: (1) before PTA, (2) before and (3) immediately after PFC-nanoparticle infusion, and (4) before MR imaging. *In-vitro* assessment of leukocyte PFC uptake was conducted by incubating the blood samples for different durations (see below) with the PFC-labeled nanoparticles. Thereby, the time course of nanoparticle phagocytosis could be evaluated with regards to the time at which nanoparticle uptake first becomes measurable, the dynamics of particle internalization, and the time at which there is a saturation of uptake.

2.3.3 Specimen Preparation and Incubation

Porcine blood samples were incubated with fluorecent (FITC) labeled PFC nanoparticles for periods of 0, 8, 16, 32, 64, 128, and 160 Minutes. Nanoparticles were added to the blood in a ratio of 1:20 (200 µl of nanoparticle solution were added to 4 ml blood). For comparison, a control sample not exposed to nanoparticles was also prepared. After each of the above time steps, incubation was stopped by mixing a sample of the blood with ammoniumchloride lysis buffer. Leukocytes were then purified prior to flow cytometry by lysis of erythrocytes in the samples.
Protocol:

Step 1: Prepare isotonic ammoniumchloride lysis buffer pH 7.4 (1 ml deionized water, 8.29 mg ammoniumchloride, 1 mg potassiumhydrogencarbonate, 0.0375 mg ethyldiaminotetraacetic acid (EDTA))

Step 2: Preapare FACS buffer (500 ml Dulbecco's phosphate buffered saline (Sigma-Aldrich Chemie GmbH, Taufkirchen, Germany), 300 mg EDTA, 10 ml fetal calf serum)

Step 3: At the intervals given above, mix 200 µl blood with 5 ml of ammoniumchloride lysis buffer in a 15 ml plastic tube (CELLSTAR-TUBE 15 ml, Greiner AG, Kremsmünster, Austria); incubate for 15 minutes

Step 4: Mix with 5 ml FACS buffer

Step 5: Centrifuge (ROTINA 38R, Andreas Hettich GmbH & Co.KG, Tutlingen, Germany) for 7 minutes (500 RCF at 4°C)

Step 6: Discard supernatant and mix cells at the bottom of the tube with ammoniumchloride lysis buffer; incubate for 15 minutes

Step 7: Mix with 5 ml FACS buffer

Step 8: Centrifuge for 7 minutes (500 RCF at 4°C)

Step 9: Discard supernatant and mix cells at the bottom of the tube with ammoniumchloride lysis buffer; incubate for 15 minutes

Step 10: Mix with 5 ml FACS buffer

Step 11: Centrifuge for 7 minutes (500 RCF at 4°C)

Step 12: Discard supernatant and mix cells at the bottom of the tube with 100 µl FACS buffer; transfer into a tube suitable for use with a flow cytometer (Sarstedt AG & Co.KG, Nümbrecht, Germany)

Step 13: After lysis of red blood cells in all specimens, incubate for 10 minutes with 1 µl of CD14 antibody, anti-human APC-Vio 770 (Miltenyi Biotec B.V. & Co.KG, Bergisch Gladbach, Germany)

Step 14: Mix with 1 ml FACS buffer

Step 15: Centrifuge for 7 minutes (500 RCF at 4°C)

Step 16: Discard supernatant and mix cells at the bottom of the tube with 250 µl FACS buffer

Step 17: Analyze in a flow cytometer

2.3.4 Flow Cytometry Measurements

Cells were measured with a flow cytometer (BD FACSVerse^{TM}, Becton Dickinson GmbH, Heidelberg, Germany). To ensure proper measurements, the required performance QC was conducted using the performance beads supplied by the manufacturer (BD FACSuite^{TM} CS&T Research Beads, Becton, Dickinson and Company, Franklin Lakes, NJ, USA) before starting the measurements. Each specimen was measured until 100000 events were registered by the cytometer. Identification of different leukocyte populations was performed via visual inspection of the recorded events on Forward- and Side Scatter plots.

2.4 Statistical Analysis

Histology samples were subgrouped into three groups as outlined in Section 2.1. The vast majority of measurements obtained on microscopic imaging were not normally distributed. Therefore, the non-parametric Mann-Whitney-U test (Mann and Whitney, 1947) was used to determine statistically significant differences between the analyzed subgroups. 95% confidence intervals around the median will be shown in Section 3 to give an indication of the spread of the presented data. Confidence intervals were calculated according to the approach proposed by Campbell and Gardner (1988) for data not following a normal distribution. In brief, the method suggested to determine confidence intervals involves a series of steps: (1) The values within a sample of data are sorted numerically, (2) each value of the sorted sample is given an index which specifies its position within the sorted sample. (3) The cumulative distribution function of a binomial distribution with probability of 0.5 is calculated for each index. (4) The index whose output value of the cumulative distribution function is closest to 0.025 is chosen as the index for the lower boundary of the confidence interval. Likewise, the output value of the index marking the upper boundary is the one closest to 0.975. (5) Those values of the sorted sample which sit at the position of the lower and upper index constitute the margins of the 95% confidence interval. Notice, due to the non-parametric nature of computation, the reported confidence intervals only approximate the 95% range (a true 95% confidence interval would cover the range from 2.5% to 97.5%). The maximal lower boundary of an interval given in Section 3 was at 2.75%, the minimal upper boundary was at 97.25%. The minimal range covered by a single confidence interval was 94.50%, the maximal range was 96.04%. Notice, for highly skewed data, some oddly appearing confidence intervals can arise. For example, the lower boundary of the interval, the median, and the upper boundary may all fall on the same numeric value.

Nominal outcome parameters such as presence or absence of thrombosis or endothelial denudation on microscopy were evaluated for statistically significant differences between subgroups using the non-parametric Chi square test (McHugh, 2013).

For purposes of correlating microscopic markers of inflammation with MRI ^{19}F signal intensity measurements, a least squares linear regression was performed. The reported p-values indicate whether the computed regression slope differed significantly from 0.

Similar to data from histology specimens, flow cytometry measurements were generally not normally distributed. Thus, 95% confidence intervals were calculated as described above.

p-values <0.05 were considered to indicate significant differences between groups. All computation was done in Python using the Scipy package (Virtanen et al., 2020).

3 Results

3.1 Markers of Injury

In order to compare carotid artery injury between untreated vessels and vessels in the mild and severe injury subgroups, several parameters were evaluated on histology sections to quantify the extent angioplasty induced damage. Luminal thrombosis, intimal destruction, structural remodeling, and cellular infiltration were considered to be indicators of the presence and severity of injury.

Complete luminal thrombosis was present in all pigs in the severe injury subgroup while only one vessel in the mild injury group was completely occluded in a few sections. The other three of the four pigs in the mild injury group had mainly no thrombosis and occasionally a thrombus causing partial luminal obstruction. No thrombosis, partial thrombosis, and complete thrombosis were found in 68.88%, 26.66%, and 6.66%, respectively, of all sections in the mild injury subgroup. After severe injury, the frequencies were 5.19%, 15.58%, and 79.22%. The difference of thrombus formation in the two subgroups was statistically significant (Chi^2: $p<0.001$).

Microscopic intimal denudation was diagnosed when the intima could not be discerned at 400- or 500-fold magnification. In these instances, either the internal elastic lamina or even the media bordered the vascular lumen. Microscopic intimal denudation was seen in all pigs in the severe injury group (in 55.52% of slides overall) while microscopic denudation was absent in the vast majority of slides (96.74%) in the mild injury subgroup (Chi^2: $p<0.001$).

3.2 Angioplasty Induced Carotid Artery Inflammation

In the sections below, the terms *cell counts*, *cellularity*, and *cell density* will be used interchangeably and denote the number of cells per unit area within a given wall segment. Overall cell counts were determined from H&E stained slides, $CD163^+$ cell counts were obtained from IHC slides (see Section 2.2.3).

3.2.1 Adventitial Response to Injury

Overall Cell Counts Comparison of treated and untreated carotids showed a highly significant ($p<0.001$) increase in overall cell counts in the adventitia. The median cell density in untreated vessels was 528.58 cells per square millimeter with a 95% confidence interval (CI) ranging from 490.98 to 562.56. In treated arteries, median cellularity increased by more than twofold to 1341.26 cells/mm^2 (95% CI 1229.36 - 1469.73).

Stratification of the vessels according to the severity of injury showed a severity dependence of the number of cells present in the adventitia. That is, after mild injury, median cell counts increased to 1258.74 (95% CI 1095.20 - 1357.50). In the severe injury subgroup, there was an even larger increase in cellularity to 1493.21 cells/mm^2 (95% CI 1277.23 - 1704.30) than in the mild injury group. The difference in median cell counts was significant between all subgroups ($p<0.001$). Refer to Figures 7 and 9 for an illustration of the analyses and representative images.

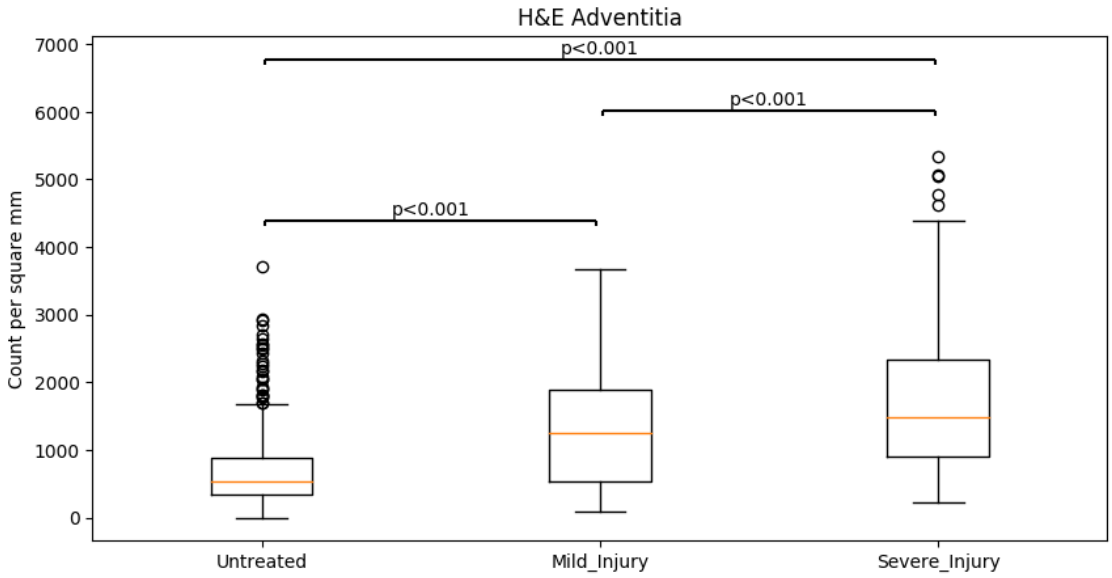

Figure 7: Overall cell counts (H&E) in the adventitia. The boxplots show the count of H&E stained cells/mm^2 in each of the 3 subgroups.

CD163$^+$ Cell Counts Comparison of treated and untreated vessels showed an even more striking difference with regards to CD163$^+$ cells. At baseline, a median of 91.13 CD163$^+$ cells/mm^2 were found in the adventitia (CI 84.03 - 98.60). This number increased about fivefold following catheterization (450.60, CI 410.20 - 487.02).

Stratifying for injury severity, revealed a similar relationship as for the overall cell counts: In the mild injury subgroup, median cellularity increased to 281.12 cells per mm^2 (CI 236.29 - 317.40). After severe injury, the increment was larger with a median of 705.11 (CI 634.86 - 766.51). Again, all differences of medians were highly significant (p<0.001). Thus, there was an about threefold and eightfold increase in cell counts in response to mild and severe injury, respectively. These ratios underline the clear injury dependence of the cellular infiltration ensuing PTA (see Figure 8).

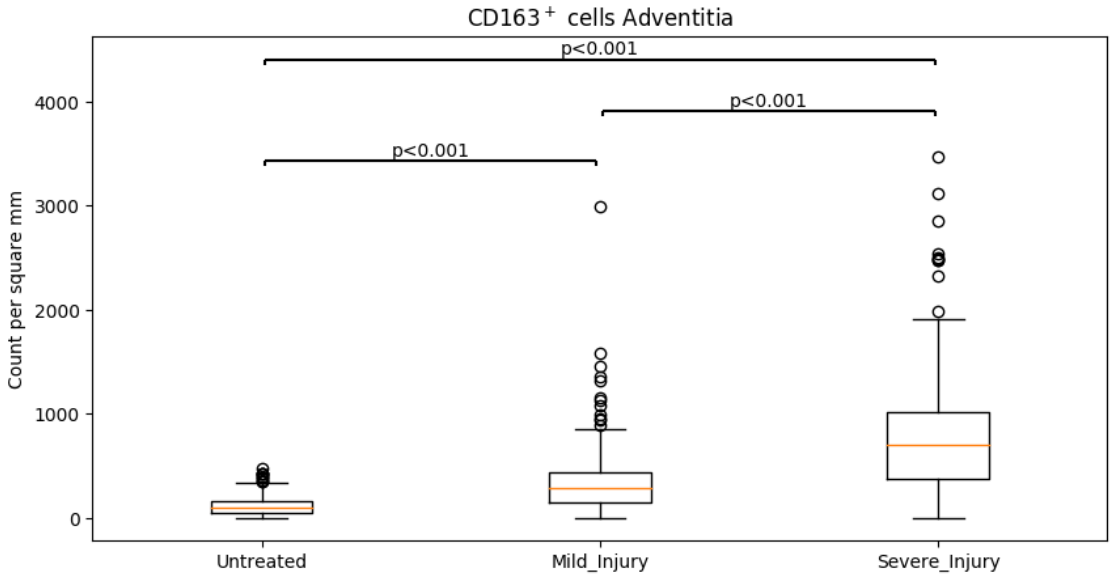

Figure 8: CD163$^+$ cell counts in the adventitia. The boxplots indicate the count of CD163$^+$ macrophages/mm^2 stratified by subgroup.

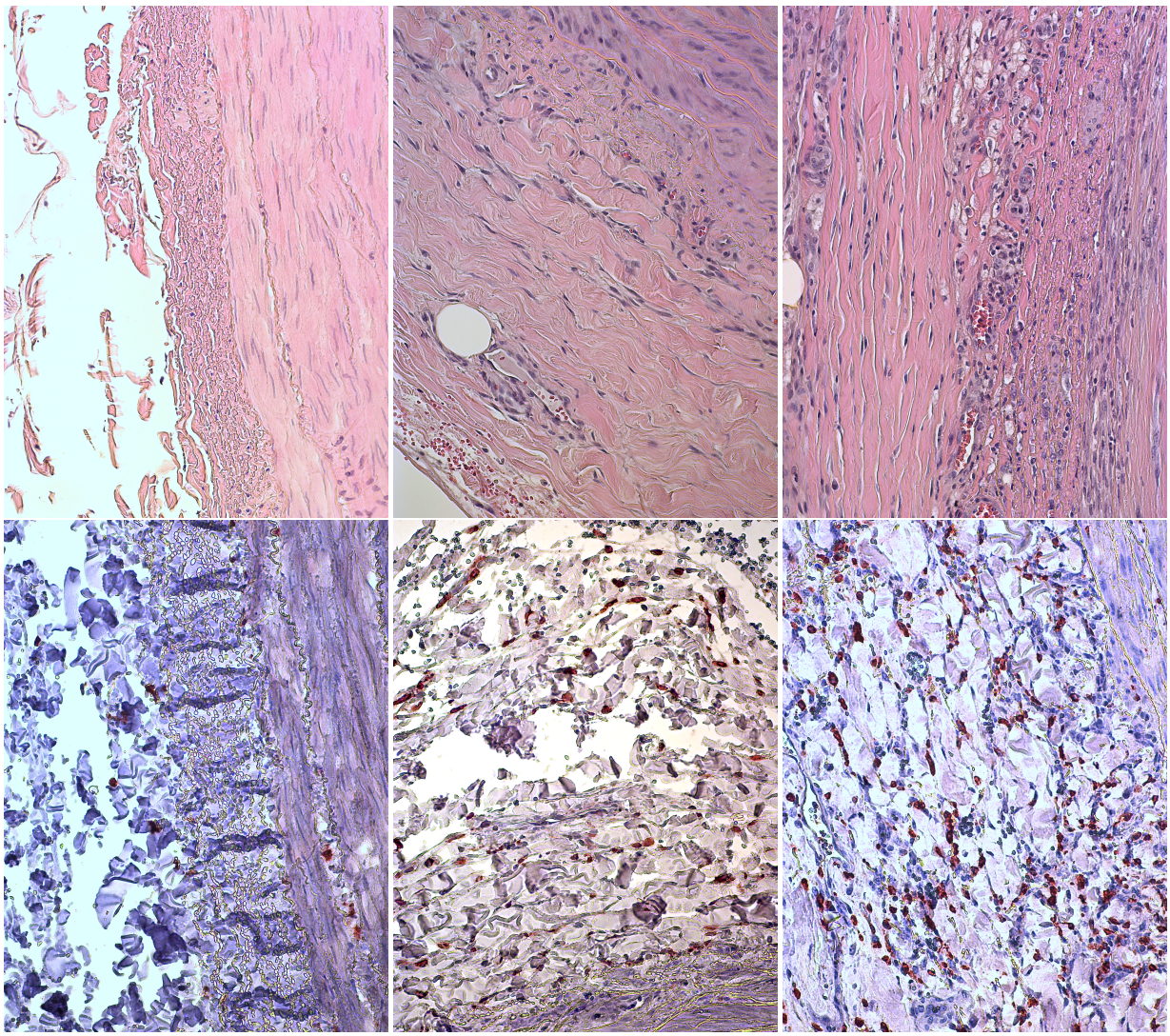

Figure 9: Microscopic images of cells in the adventitia. Cells overall (upper panel) and $CD163^+$ (lower panel) in the adventitia of untreated (left), mildly injured (center), and severely injured (right) arteries. Magnification 200-fold.

3.2.2 Medial Response to Injury

Overall Cell Counts Cell counts in treated and untreated medias also differed significantly. The median number of cells/mm^2 was 1665.40 in untreated carotids (95% CI 1593.28 - 1744.40). After angioplasty, the count increased to 2037.01 cells per mm^2 (95% CI 1930.65 - 2117.62). These findings were highly significant ($p<0.001$) even though the difference in cellularity in untreated arteries and vessels after treatment was much less than in the adventitia.

In contrast to the changes seen in the adventitia, overall cell counts did not show a clear severity-dependence with respect to the severity of angioplasty-induced injury. In mildly injured vessels, median cell density increased to 2144.37 cells/mm^2 (95% CI 2043.70 - 2243.72) while in severely injured vessels there were 1909.63 cells/mm^2 (95% CI 1801.49 - 2065.44). Both of these counts differed significantly from the baseline cell count, but the difference in cellularity in mildly and severely injured carotids was not statistically significant ($p=0.272$). The above values amount to a 25% increase in cell density in the media (compare to the 2- to 3-fold increase in the adventitia). Results of the findings are presented in Figure 10. In Figure 13, photographs of H&E and IHC stained sections of the media are shown.

Of notice, changes in morphology of smooth muscle cells in the media were commonly seen after PTA

(see Figure 11). At baseline, these cells had dense elongated nuclei. In response to injury, nuclear shape and appearance changed, causing the nucleus to become more oval and hematoxylin staining to become less homogeneous. This finding is consistent with a functional activation of the smooth muscle cells which is associated with an increase in nuclear euchromatin. Notice the gradient of activation in the left image of Figure 11: Close to the lumen, part of which is seen in the upper right corner of the image, cells exhibit the changes described above. Conversely, with increasing distance from the site of injury, cells appear more similar to the cells at baseline shown in the right image of the Figure.

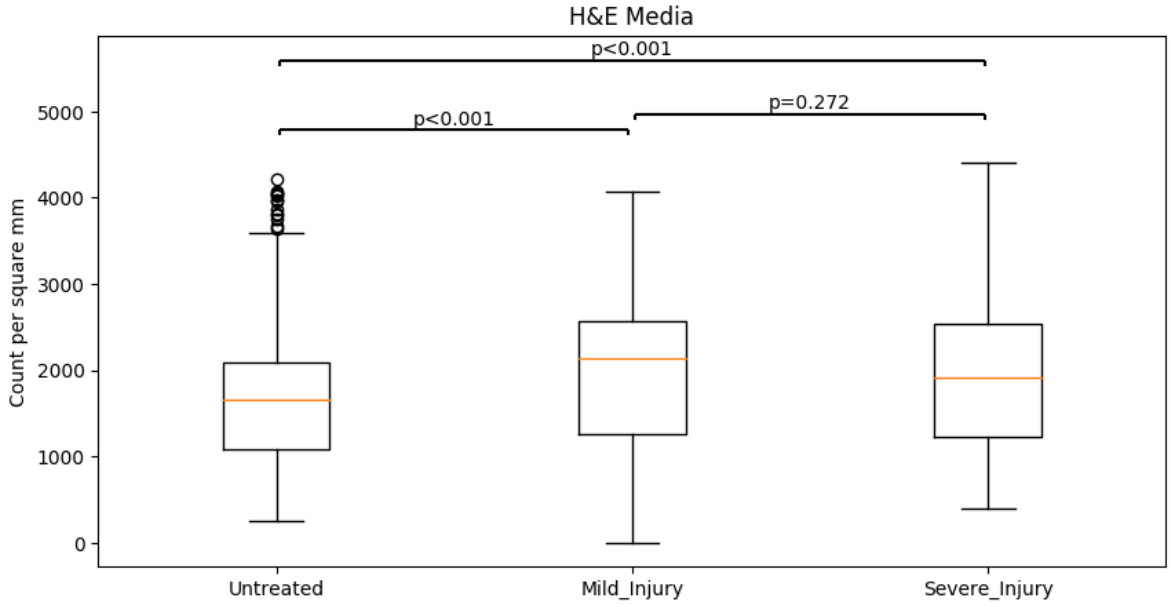

Figure 10: Overall cell counts (H&E) in the media. The boxplots show the count of H&E stained cells/mm^2 in each of the 3 subgroups.

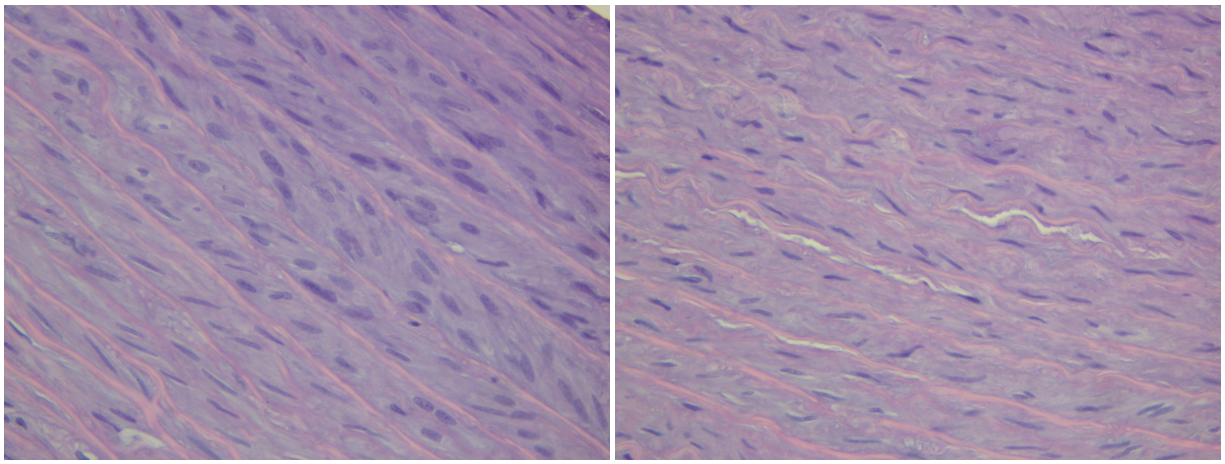

Figure 11: Smooth muscle cell morphology. Appearance of smooth muscle cells after mild injury (left); quiescent smooth muscle cells in an untreated artery (right). Magnification 200-fold.

CD163$^+$ Cell Counts The number of CD163$^+$ cells increased vastly in response to PTA. At baseline, immunostained cells were scarcely seen in the media with a median cell density of 0 cells/mm^2 (95% CI 0.00 - 0.00, see Section 2.4). The mean cell count was 11.41 cells/mm^2. Comparing these numbers to the number of smooth muscle cell nuclei on H&E staining emphasizes that CD163$^+$ cells comprised a negligible fraction of all cells in the media in untreated arteries. The median count increased greatly after treatment to 30.43 cells/mm^2 (95% CI 19.20 - 46.76). Notice here, that despite this major increase, cellularity in the media after treatment was still much smaller than the median number of CD163$^+$ cells found in the adventitia of untreated arteries. Thus, medial cellularity rose from a virtually undetectable baseline level to a very minor population of cells. Further, most CD163$^+$ cells were seen in the part of the media adjacent to the adventitia and diminishing counts were observed in closer proximity to the intima.

As opposed to overall cell density in the media, the CD163$^+$ cell counts did show a severity dependence with respect to the severity of PTA induced injury (see Figure 12). In mildly injured arteries, the cell count remained close to 0 (median cellularity of 0 cells/mm^2, 95% CI 0.00 - 0.00). In contrast, severely injured vessels had a median cell density of 86.17 (95% CI 69.75 - 105.55). The mean cell count was even higher at 236.94 cells/mm^2. Notice, that even after severe injury, the cell infiltration was only at about the same level as the baseline cell density of CD163$^+$ cells in the adventitia. This finding highlights, that a significant degree of injury was necessary to induce a measurable increase in the number of CD163$^+$ cells in the media. Still, the absolute number of cells remained small compared to the cell infiltration seen in the adventitia.

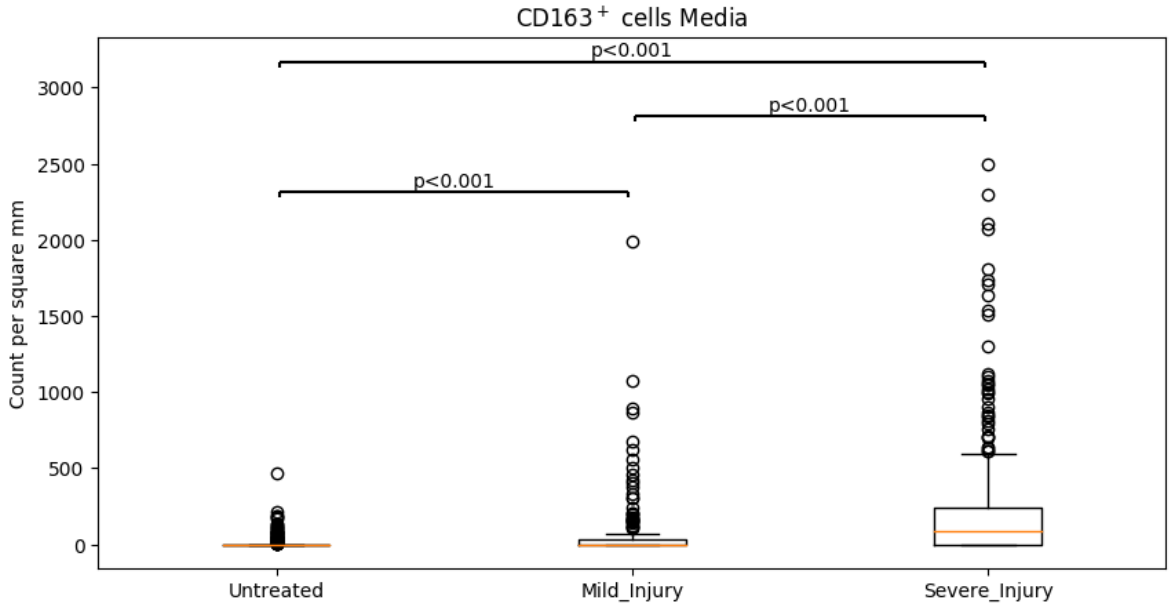

Figure 12: CD163$^+$ cell counts in the media. The boxplots indicate the count of CD163$^+$ macrophages/mm^2 stratified by subgroup.

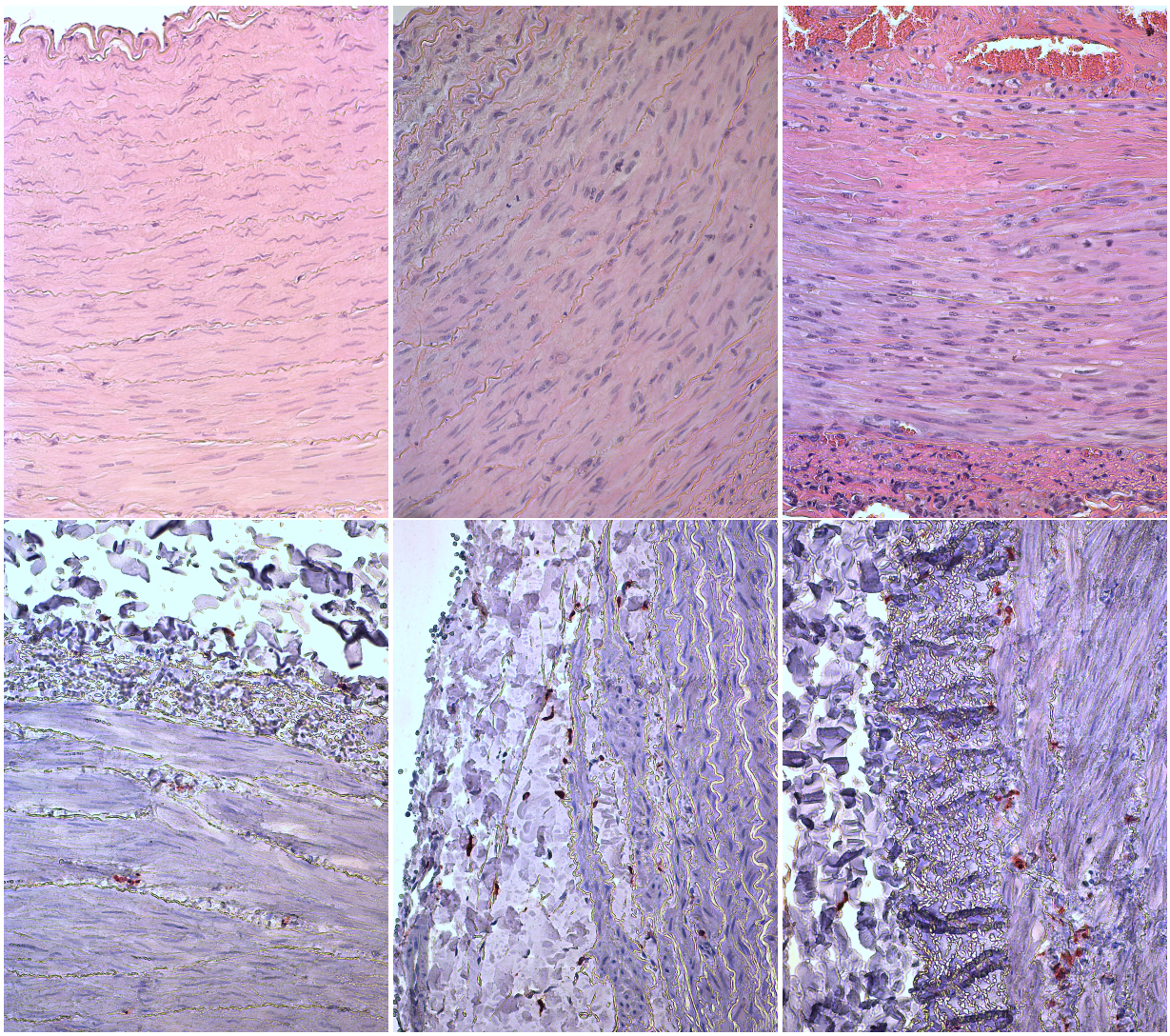

Figure 13: Microscopic images of cells in the media. Cells overall (upper panel) and CD163$^+$ (lower panel) in the media of untreated (left), mildly injured (center), and severely injured (right) arteries. Magnification 200-fold.

3.3 Angioplasty Induced Vascular Remodeling

Angioplasty of the carotid artery lead to a characteristic pattern of changes within the vessel wall. These changes were part of the structural transformation occurring after endoluminal injury. Collectively, we will refer to this process as vascular remodeling. Since our point of observation of the remodeling process is fixed at seven days after angioplasty, the changes described next were considered to be part of the early vascular remodeling.

The main features of early remodeling constitute luminal thrombosis, luminal and adventitial enlargement, and intimal reactions (see Figure 14). All of these features were related to the severity of injury. In brief, mildly injured vessels showed typically no thrombosis (less commonly, there were partial and complete luminal occlusions), vessels in the severe injury subgroup consistently had a complete luminal thrombosis. Similarly, luminal enlargement was restricted to the severe injury subgroup. Increases in adventitial radius were independent of the extent of injury, while intimal thickening was observed only in the mildly injured arteries. These vascular remodeling processes will be presented in greater detail below.

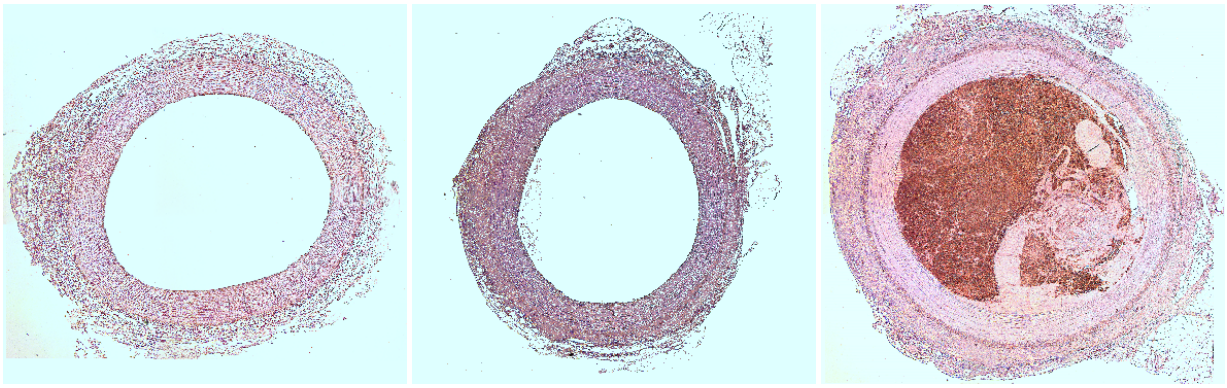

Figure 14: Microscopic overview of carotid sections. The figure shows H&E stained sections of untreated (left), mildly injured (center), and severely injured (right) arteries at 25-fold magnification.

3.3.1 Wall Segment Radii

Angioplasty caused marked alterations of the geometry of the carotids. The findings are summarized in Figure 15. Refer to this figure during the following discussion. A priori, an intuitive assumption about the effect of endoluminal distension on a vessel's geometry could be the following: (1) It will cause an increase in luminal radius, (2) injury will be greatest close to the lumen, and thus (3) the strongest structural reponse will be seen in the inner wall layers.

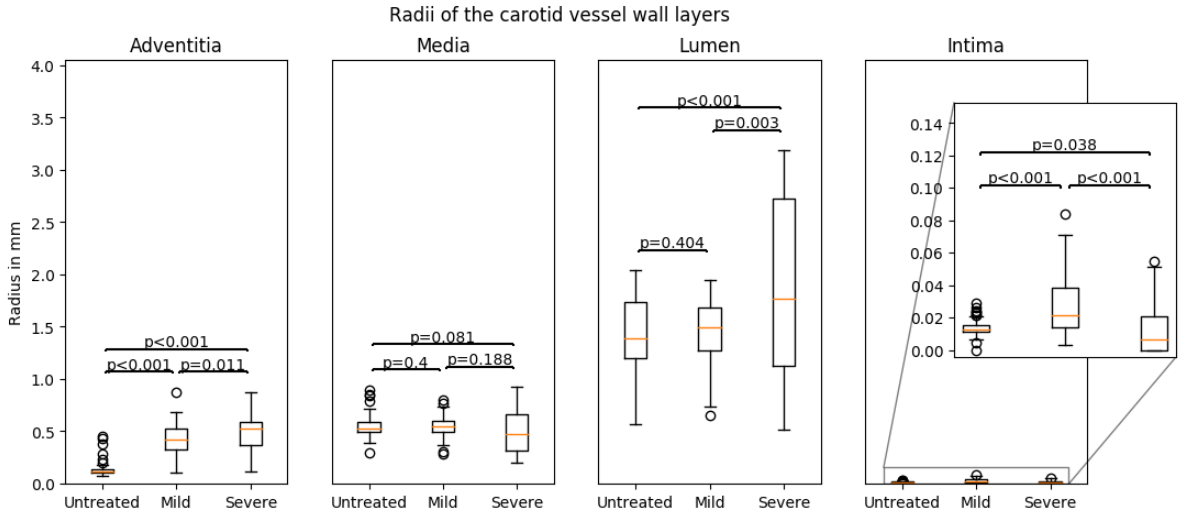

Figure 15: Carotid wall segment radii. The radii (in mm) of the four carotid artery segments are presented stratified by severity of injury: Adventitia (leftmost panel); Media (left inner panel); Lumen (right inner panel); Intima (rightmost panel), the inset shows the details of the plot on a separate scale.

Consistent with the first hypothesis, we noted an increase in luminal radius in treated arteries with respect to their uninjured counterparts. After stratification into the severe and mild injury subgroups, only the severely injured vessels proved to be responsible for the increase in luminal diameter. The median radius in those arteries was 1.76 mm (CI 1.63 - 2.12) which was significantly different from both untreated and mildly injured vessels with radii of 1.38 mm (CI 1.34 - 1.55) and 1.50 mm (CI 1.31 - 1.60), respectively. The difference of medians of the latter two subgroups was not significant (p=0.40). Notice here, without treatment, the luminal radius of the carotids remained within a fairly narrow range. Catheter intervention causing mild injury did not disturb this finding to a significant extent while severely injured vessels showed a major increase in the range of radii (see Figure 15). Recall, that the explanted

arteries were typically composed of segments directly exposed the catheter and other segments without immediate exposure. Therefore, a recurring feature regarding changes in radii was an increase in the spread of measured values after treatment since structural responses were more pronounced in greater proximity to the site of injury. Further, the finding that luminal enlargement was restricted to the severe injury subgroup is consistent with our observations regarding thrombosis and endothelial abrasion of the vessels. When the catheter did not distend the vessel sufficiently to cause a measurable increase in luminal radius, there was also no major endothelial injury. Thus, only a small fraction of the mildly injured carotids exhibited a complete abrasion of the endothelium. Without endothelial abrasion, there was no exposure of thrombogenic subendothelial tissue to the bloodstream. Consequently, thrombosis was seen far less frequently (33% of all sections) than in severely injured vessels (79% of sections).

But as opposed to the second hypothesis stated above, the adventitia was affected most by structural remodeling processes despite being located furthest from the site of injury. Adventitial remodeling in terms of radial enlargement occurred independent of the severity of injury. The median baseline radius of the adventitia was small at 0.11 mm (CI 0.11 - 0.12) with the adventitia being composed of a small layer of loose connective tissue with few resident cells seen within. Treatment led to an about threefold thickening with median radii averaging 0.42 mm (CI 0.36 - 0.48) and 0.52 mm (CI 0.47 - 0.57) in mildly and severely injured vessels, respectively. This increase in size was associated with deposition and consolidation of connective tissue in addition to the increase in cellularity described previously (shown in Figure 9).

There was a curious relationship between the intimal pattern of injury and the severity of catheter irritation. As already noted, in severely injured vessels, the intima was completely abraded in many sections, effectively rendering its size to zero there. The median radius was 0.006 mm (CI 0.000 - 0.017) which was significantly less ($p=0.038$) than the radius of untreated vessels at 0.013 mm (CI 0.012 - 0.013). Notice the major increase in the range of values compared to untreated vessels. This finding is in line with the above observation that treated arteries were composed of parts directly exposed to injury, parts adjacent to sites of injury, and parts remote from injury such that the reported range of intimal radii contains intimal measurements with differing degrees of catheter exposure. In about half the sections the intima was abraded while in the other half the intima remained quiescent or showed a mild thickening. In the abraded sections, intimal regeneration was not an observed feature seven days following endovascular injury. Conversely, after mild injury, we noted some slight intimal hyperplasia with an increase in radius (median 0.022 mm, CI 0.018 - 0.034) as compared to contralateral untreated arteries and severely injured arteries. The difference to the median intimal radius of the other two subgroups was significant ($p<0.001$). This finding highlights, that there is an intimal response as early as a week after endovascular injury. But this response (1) required the presence of an intima and (2) was by no means strong enough to cause any degree of luminal compromise.

Regarding medial size it is again noteworthy that its radius remained within a narrow range throughout most sections in the absence of treatment. The median radius was 0.53 mm (CI 0.51 - 0.56). Mild injury did not cause any significant change in radius (0.54 mm, CI 0.53 - 0.57, $p=0.40$) and the narrow range of radii was preserved. Following severe injury, median medial radius was smaller at 0.47 mm (CI 0.40 - 0.61) and the observed range of values increased to some extent. The lesser radius was not significant compared to untreated and mildly injured vessels ($p=0.081$ and $p=0.188$, respectively). Of notice, medial necrosis could be observed frequently in severely injured carotids (see Figure 13).

Figure 16 gives an overview of the changes in radius seen in the individual wall segments along the longitudinal extent of one vessel of each subgroup. The three plots in the figure summarize the structural remodeling processes outlined previously: The wall segments of untreated vessels were stable in size, only the luminal radius tapered along the course of the artery. Mild injury mainly evoked an adventitial reponse, whereas severe injury caused an irregular luminal enlargement. Neighboring the enlarged lumen, a radius-reduced media can be seen. Adventitial thickening was widespread and not

limited to the immediate surroundings of catheter contact.

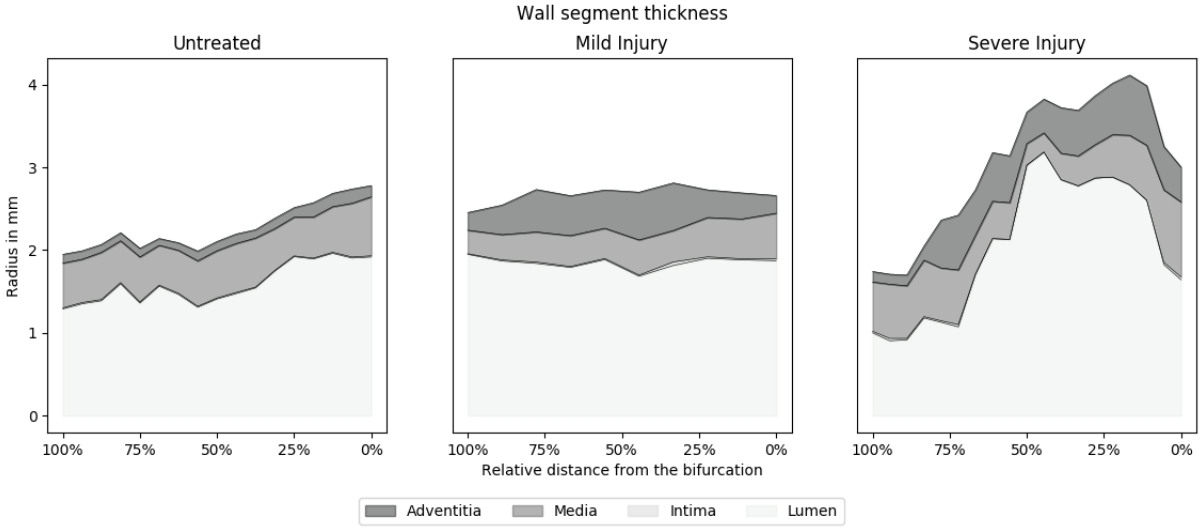

Figure 16: Longitudinal changes of wall segment radii. The radii (in mm) of the four carotid artery segments are shown along the longitudinal extent of an untreated (left), mildly injured (center), and severely injured vessel (right).

3.3.2 Shape Complexity

The focus of the previous section were changes in radius of the individual segments of the arterial vessel wall. In this discussion, the possibly complex shapes of the carotids were compressed into a single value, disregarding any alterations in geometry other than radial enlargement. That is, the carotids, and therefore also the individual wall segments, do not constitute perfectly circular structures but may show deviations from this ideal shape. The goal of this section is to quantify such changes in shape. Section 6.2 delineates the assumptions underlying the use of the radius as a descriptive value for non-circular structures.

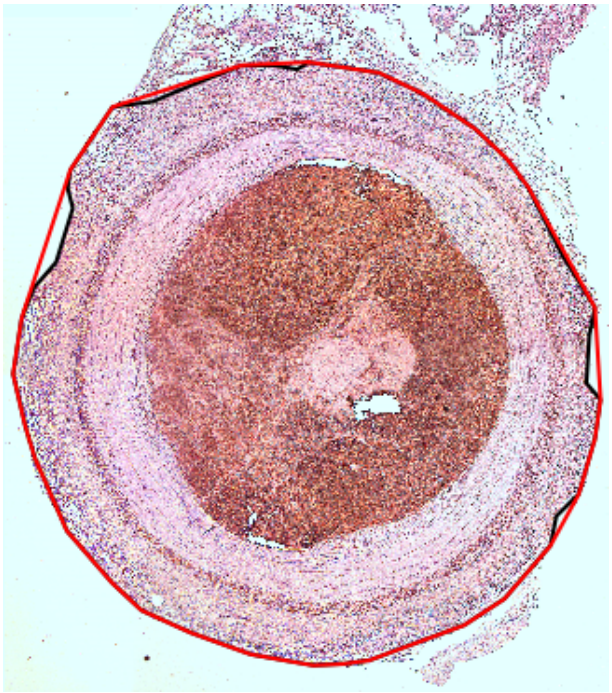

Figure 17: Adventitial shape complexity. The contour of the adventitia is outlined in black and its convex hull in red. Magnification 25-fold.

Shape complexity measurements attempt to quantify the intuitive notion of complexity of a shape. Features that distinguish complex shapes from simpler ones (such as circles or squares) include among others the number and magnitude of changes in direction and orientation of a shape's circumference. Directional changes constitute the presence of angulations between adjacent edges which define the contour of the shape. Orientational changes are dependent on the angle between two arbitrary edges and the angle preceding this given angle. That is, the preceding two edges may be oriented such that moving from the first edge to the second edge requires a left turn. If moving from the second edge to the next one then requires a right turn, a change in orientation occurred.

A simple measure of shape complexity makes use of convex hulls. A convex hull is the smallest convex

polygon that encompasses a shape of interest. The term convex refers to the fact that there are no changes in orientation in the contour of the convex hull. The larger the area needed for a convex hull to encompass a shape the greater the shape's complexity. Therefore, to quantify the complexity of the carotid's shapes the following calculation was employed: $1 - \frac{Area(Shape)}{Area(ConvexHull)}$. Figure 17 compares the convex hull of the contour of the adventitia to the adventitial contour itself.

Without treatment, the complexity of media and adventitia was low since these structures were convex in the vast majority of sections (rendering their shape complexity close to 0, see Figure 18). Luminal shape was more complex than medial and adventitial shape at baseline. After treatment, there were no significant changes in medial and luminal shape complexity. In contrast, the adventitia showed a significant increase ($p<0.001$) in complexity. Of notice, this increase occurred irrespective of the severity of injury. There was no statistically significant injury-severity dependence of adventitial shape complexity ($p=0.216$ comparing mildly and severely injured vessels). As already noted, these findings were not mirrored by likewise increases in the medial and luminal shape complexity. This suggests that the structural changes found in the adventitia after injury were not the result of passive propagation of injury from lumen through the media into the adventitia but originated in the adventitia itself. In line with the findings presented in the previous sections, the following sequence of events ensued endoluminal injury: (1) Immune cells and other cell types accumulated in the adventitia, (2) the connective tissue surrounding the adventitia consolidated causing (3) an irregular radial enlargement. Thus, early vascular remodeling involved active processes in the adventitia while the other wall layers predominantly showed the direct effects of injury like medial necrosis, endothelial denudation and subsequent thrombosis with fewer features of an active response pattern leading to changes in morphology.

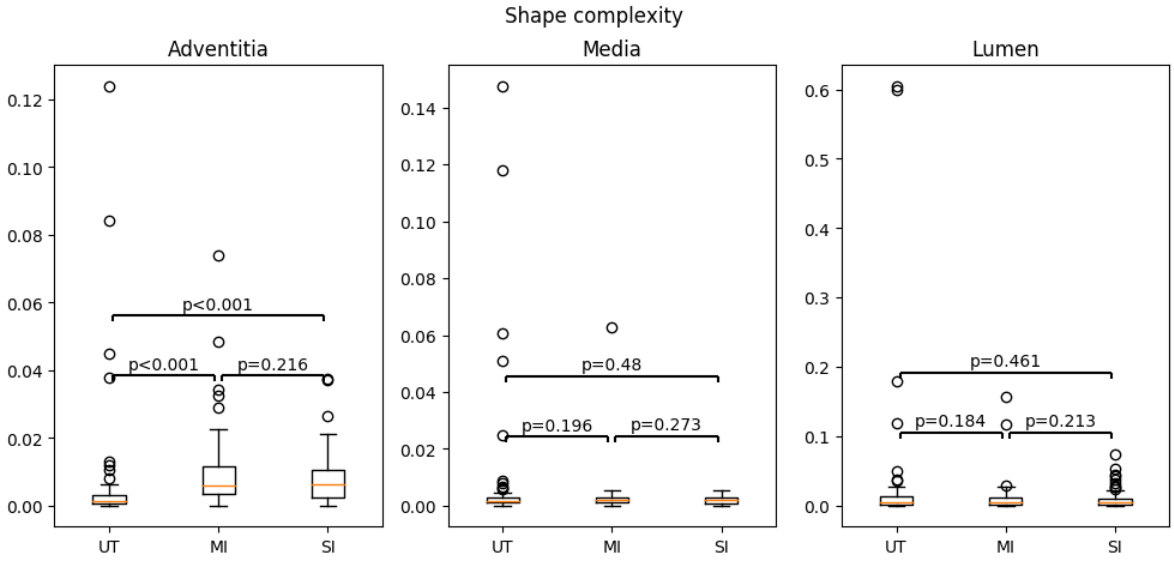

Figure 18: Shape complexities of the individual wall layers. Shown are the shape complexities of the adventitia, media, and lumen in untreated (UT), mild injury (MI), and severe injury (SI) subgroups. The shape complexities are unitless and were calculated using the equation given in the text.

3.4 Relation between ^{19}F Enhancement and Tissue Response to Injury

In this section we return to our primary goal which is to show that the inflammatory response induced by angioplasty can be detected by ^{19}F MR imaging. Further, we claimed that there was a quantifiable relationship between inflammation as measured by MRI and inflammation seen on histology. Recall, that the source of the signal which is detected by ^{19}F MRI are the fluorine atoms inside the nanoparticle infusion administered to the pigs. These nanoparticles are then taken up by phagocytic cells inside the blood and are then transported inside these cells to sites at which the phagocytes leave the bloodstream. A sufficient accumulation of phagocytes at a focus of inflammation evokes a measurable MRI signal.

Relation to Injury Severity Ex vivo ^{19}F enhancement was detected in 8 of 8 pigs. In both the severe and the mild injury subgroups, all four treated vessels exhibited contrast enhancement. None of the untreated vessels accumulated sufficient nanoparticles (and thus phagocytes) for a detectable signal to arise. Even though all of the vessels in the mild injury group showed ^{19}F enhancement, there was a noticeable difference in signal intensity depending on the severity of treatment: The mildly injured arteries accumulated significantly less contrast agent than the four carotids in the severe injury group ($p<0.001$, see Figure 19). Ex vivo MRI scans of two carotid arteries are shown in Figure 20. Merging the signal from conventional ^{1}H images and ^{19}F signal clearly localizes the source of the ^{19}F signal within the treated vessels whereas untreated arteries do not exhibit any contrast enhancement.

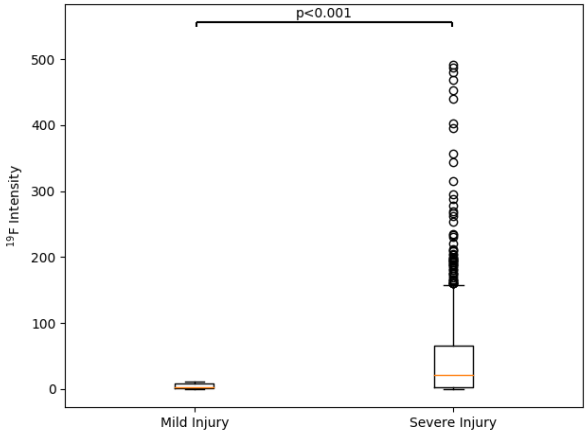

Figure 19: ^{19}F signal intensity. Boxplots of the ^{19}F signal intensity measured in cross-sections of vessels the mild and severe injury subgroups.

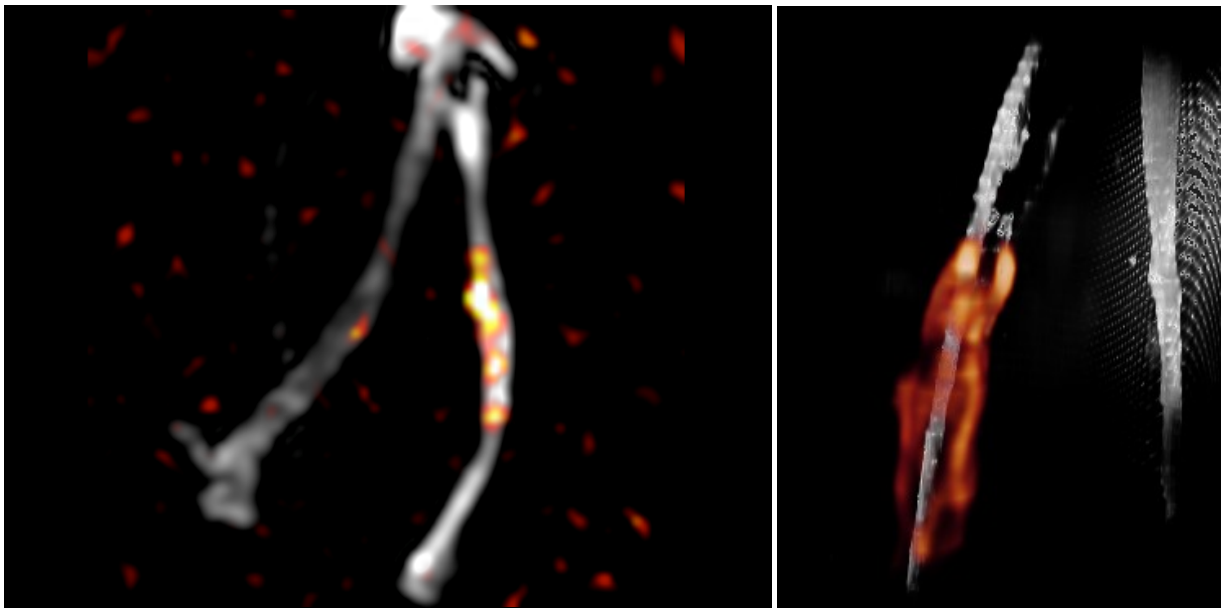

Figure 20: MRI scans of explanted carotid arteries. The figure shows the overlay of the ^{19}F signal (red) and ^{1}H signal (gray) from two arteries. Overview of the bifurcation and both carotids (left panel), close-up view of ^{19}F enhancement in the distal part of a treated vessel (right panel).

Relation to Mean Cell Counts Figure 21 illustrates the association between mean ^{19}F intensities and mean cell counts for each pig individually. Both, the mean number of all cells and of CD163$^+$ cells in the adventitia correlated with the mean ^{19}F signal. Regression yielded an increase in signal intensity of 4.32 and 9.63 units for every 100 cells in the adventita, respectively. Both values were barely not significant (p-values of 0.10 and 0.09). Of notice, only the number of CD163$^+$ cells in the media showed a significant positive correlation with the ^{19}F signal. Here, linear regression showed a ^{19}F increment of 18.33 units for every 100 CD163$^+$ cells per square millimeter ($p<0.001$). In our opinion though, it is doubtful that this finding reflects a true association. Rather, the location of the rightmost value in the plot relative to the remaining values gives rise to the relation. In fact, if that rightmost value is excluded from the regression analysis, the association becomes much smaller (2.08 units ^{19}F increment/100 cells) and statistically insignificant ($p=0.73$). There was no significant association between ^{19}F signal intensity and the overall cell count in the media ($p=0.56$).

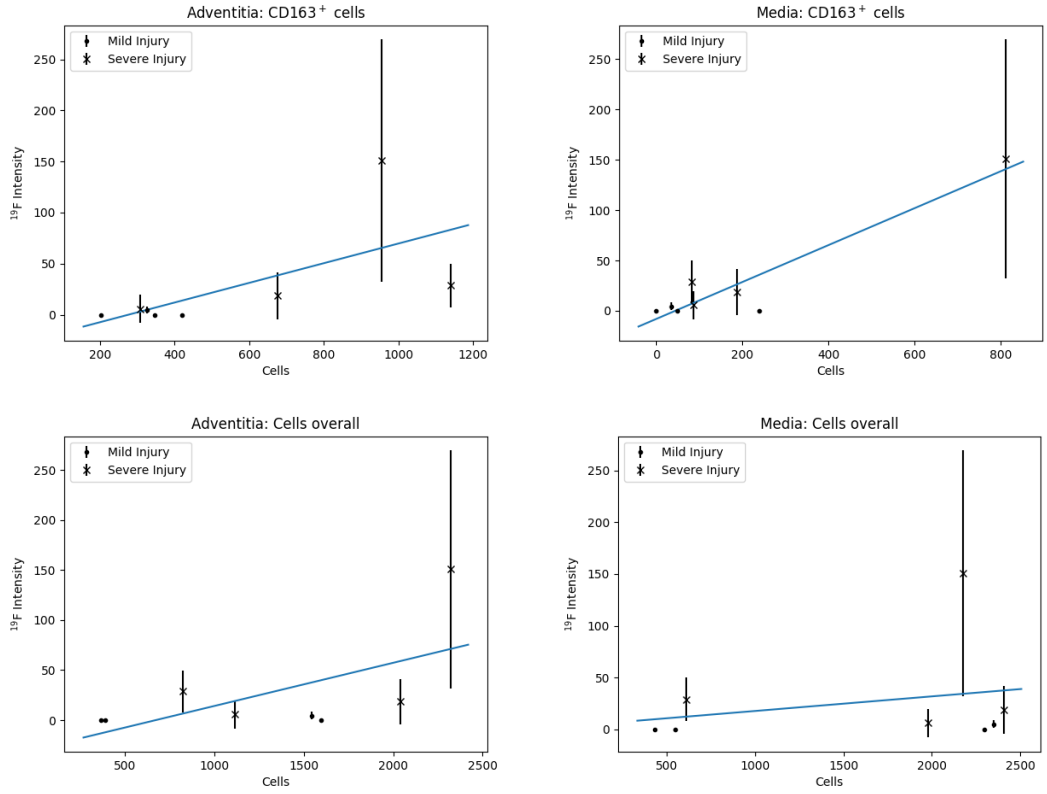

Figure 21: Correlation of mean cell counts with mean ^{19}F signal. Plots of the mean ^{19}F signal intensity against the mean number of CD163$^+$ cells/mm^2 (upper panel) and overall cells/mm^2 (on H&E stain, lower panel) in the adventitia (left) and media (right) for each pig. The solid lines were derived from linear regression of cell counts on ^{19}F signal.

Relation to Local Cell Counts For a more intricate analysis of the relationship of cell counts and ^{19}F signal, the approximate origins of both values were matched. That is, the distance from the carotid bifurcation was determined for each measurement of MRI signal and for each histology section. Thereby, associated values could be graphed in a scatter plot as shown in Figure 22. Linear regression performed separately for the mild and severe injury subgroups yielded a strong positive association between CD163$^+$ cells and ^{19}F signal in the severe injury group while only a minimal association could be found after mild injury. In the latter subgroup, there was an increase of 0.2 and -0.2 units of ^{19}F intensity for a 100 CD163$^+$ cell/mm^2 increment in the adventitia and media, respectively ($p=0.38$ and $p=0.54$). Conversely, in response to severe injury, ^{19}F signal intensity increased on average by 4.8 units in the adventitia and

8.9 units in the media for every 100 $CD163^+$ cells/mm^2 (p=0.003 and p<0.001).

Regarding the association between ^{19}F intensities and the overall cell counts in adventitia and media, findings were similar. After mild injury, the regression slope was near 0 at 0.2 (p=<0.001) and 0.1 (p=0.003) for adventitia and media, respectively. Following severe injury, both the cell count in the adventitia and in the media were significantly associated with ^{19}F signal (p<0.001). The association was stronger in the adventitia with an increment of 5.6 units of ^{19}F intensity per 100 cells/mm^2. The increment in the media was about half at 3.4 units for each 100 cells per mm^2.

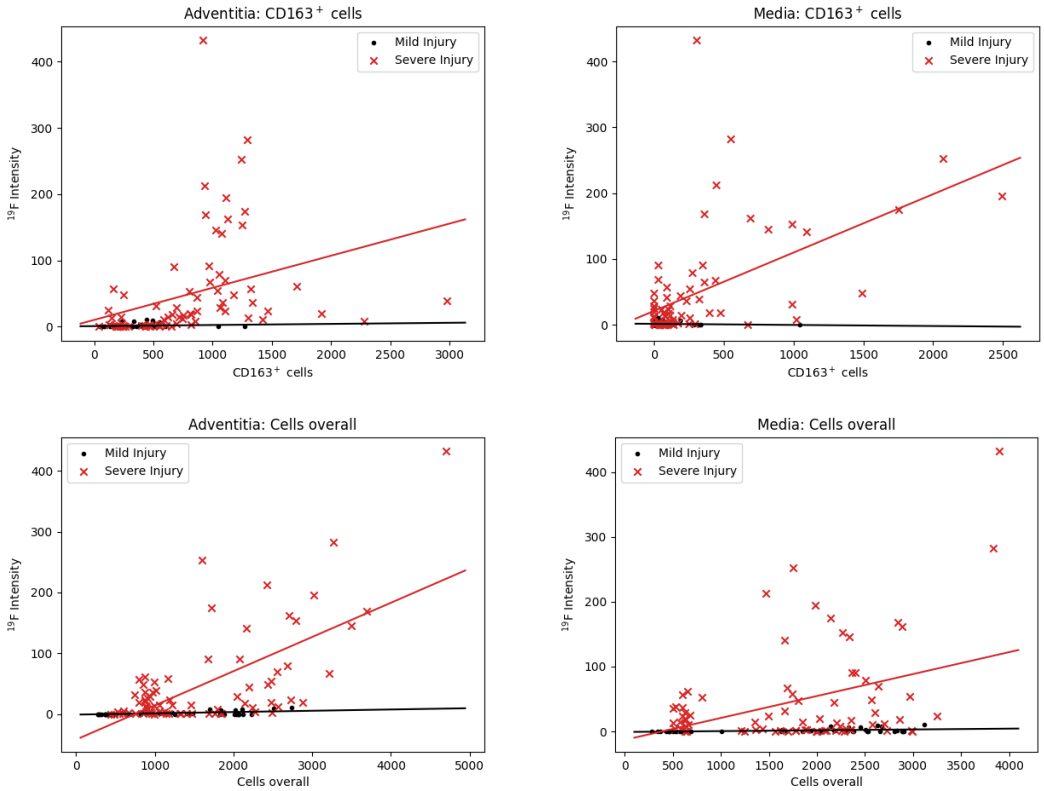

Figure 22: Correlation of cell counts and ^{19}F signal. The ^{19}F signal intensity of a given MR cross-section is plotted against the mean number of $CD163^+$ cells/mm^2 (upper panel) and overall cells/mm^2 (lower panel) in the adventitia (left) and media (right) of each histology slide located within the extent of the MR cross-section. The solid lines are based on a linear regression of cell counts on ^{19}F signal.

Colocalization of ^{19}F Signal and $CD163^+$ Cells The data presented above, constitutes aggregate data originating from all arteries in which *ex vivo* ^{19}F signal was detected. But we did not motivate our discussion by claiming that there was a quantifiable correlation between ^{19}F intensity and inflammation averaged over a number of different vessels. Rather, we set out to show that inside a single vessel this quantifiable relation exists. Figure 23 highlights that, in fact, such correlations can be found with respect to $CD163^+$ cells in the adventitia. The Spearman correlation coefficients of the data underlying the two plots were 0.72 and 0.81 (p=0.003 and p<0.001, respectively). Notice, that not in all arteries cell counts and MRI signal intensities showed a match this convincing. In the severe injury subgroup, the other correlation coefficents were 0.46 (p=0.049), 0.55 (p=0.009), -0.12 (p=0.627). Hence, in three of the four pigs in the severe injury group and in one pig in the mild injury group there was a statistically significant correlation. In these pigs, correlation coefficients indicated the presence of a moderate to high amount of correlation between *ex vivo* ^{19}F signal intensity and $CD163^+$ cells in the adventitia. Measurements of cell density from the media and overall cell counts in the adventitia were not associated in a similar fashion with ^{19}F signal intensities.

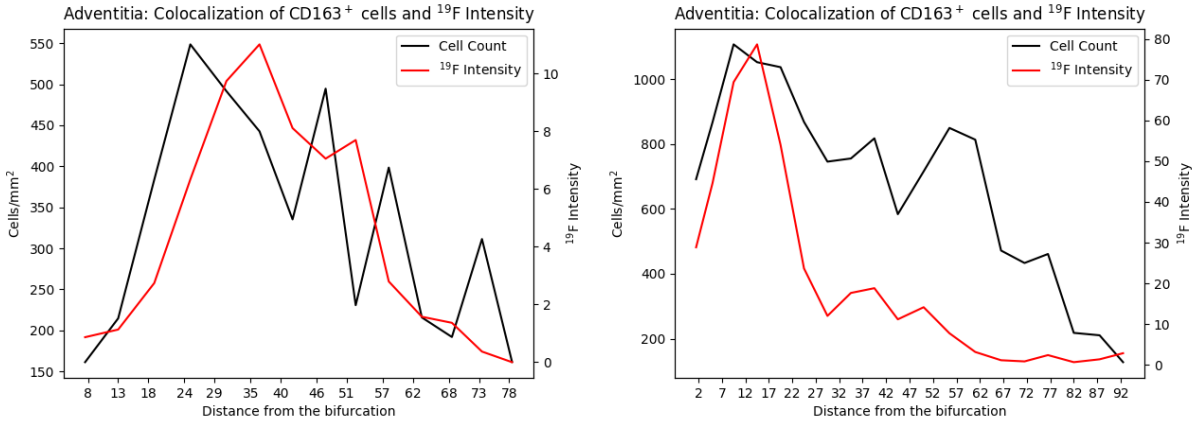

Figure 23: Longitudinal correlation of CD163$^+$ cells in the adventitia and ^{19}F signal intensity. Mean cell counts/mm^2 located within the extent of one MR cross-section and the ^{19}F signal intensity of the given section are plotted against the distance of the measurements from the bifurcation. Left panel: Mild injury subgroup, Right panel: Severe injury subgroup.

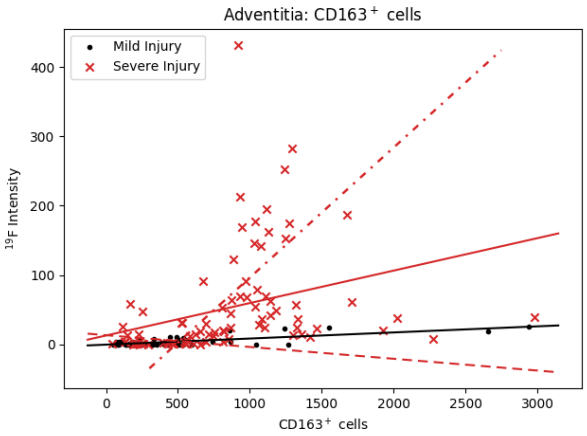

Figure 24: ^{19}F colocalization threshold. The same data is plotted as in Figure 22. Two additional regression lines are included. The dashed line is based on a linear regression of cell counts <350/mm^2 on ^{19}F signal intensities. The dotdashed line shows the linear regression of cell counts between 350 and 1300/mm^2 on ^{19}F signal.

To visualize the colocalization of ^{19}F signal and CD163$^+$ cells in the tissue, Figure 25 contains three-dimensional reconstructions of these measurements for the carotid shown in the right part of Figure 23. Cell counts were sampled along the length of the artery in 19 sections at 8 locations each. ^{19}F signal intensities were also measured along the length of the vessel and for those intensities that were located within the extents of a histology section, the mean was taken. Thereby, each intensity cound be matched with a cell count. Cell counts and intensity measurements were then used to populate a three-dimensional array for graphical reconstruction. Comparing the center and right plot of Figure 25 to the right plot in Figure 23, notice the peak in ^{19}F intensity close to the bifurcation. Cell counting also reveals its maximum in this part of the artery. But while ^{19}F intensities taper off rapidly, the logitudinal extent of elevated cell counts is much larger. The discrepancy between cell counts and ^{19}F signal likely reflects the MRI detection threshold. Towards the distal end of the artery, cell counts also taper off to the finally return to the range of cell counts found in the untreated side. The potential presence of a ^{19}F detection threshold can also be noted in Figure 24. Shown is the same data as in the left upper panel of Figure 22. Here, two additional regression lines were included. The dashed line shows the association between ^{19}F signal intensity and CD163$^+$ cell counts <350/mm^2 while the dashdotted line relates cell counts between 350 and 1300/mm^2 to the signal measured by MRI. For cell counts <350/mm^2 we found a nonsignificant (p=0.81) negative association of -1.70 units of ^{19}F/100 CD163$^+$ cells. On the contrary, higher cell counts were strongly correlated to ^{19}F signal (18.8 units/100 cells, p<0.001).

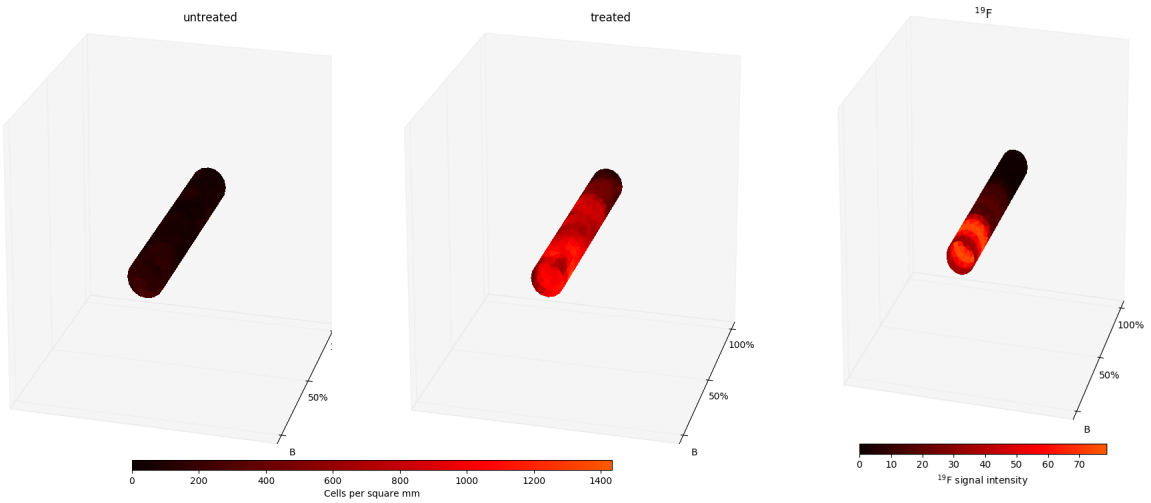

Figure 25: 3D reconstruction of CD163$^+$ cell densities and ^{19}F signal. The density of CD163$^+$ cells in the adventitia of an untreated (left) and treated (center) carotid artery is shown in shades of red along the longitudinal extent of the vessels. The ^{19}F signal measured along the distance of the treated artery is shown for comparison (right).

3.5 Nanoparticle Uptake by Porcine Leukocytes

Perfluorocarbon-containing nanoparticles were administered to the pigs as an MRI contrast agent. To assess the capability and extent of nanoparticle phagocytosis by different leukocyte subtypes *in vitro*, flow cytometry was used. Different cell types were identified and gated on Forward- and Side-Scatter plots generated by the flow cytometer. Perfluorocarbon uptake was quantified using fluorescent labeled nanoparticles. Blood samples of eight pigs were included in the following results.

3.5.1 Nanoparticle Phagocytosis

Monocytes and neutrophils from porcine blood samples showed a statistically significant nanoparticle uptake. The extent of nanoparticle uptake was similar in these two cell types. Lymphocytes showed only a marginal increase in FITC intensity, consistent with minimal nanoparticle uptake. As shown in Figure 26, these findings were consistent for each day of measurement. Referring to both Figures 26 and 27, there is a noticable difference in the dynamics of particle phagocytosis between neutrophils and monocytes. The curves suggest a more rapid (potentially exponential) uptake in neutrophils which saturates after about 30 to 60 minutes, while monocytes seem to engage in a more constant uptake pattern which saturates later at around 60 minutes.

To determine the effects of the angioplasty and nanoparticle infusion on nanoparticle phagocytosis, measurements were conducted prior to angioplasty, prior to nanoparticle infusion, following the infusion, and prior to MRI. The first study was used as a measure of baseline phagocytic capacity. Of notice, both angioplasty and the infusion of nanoparticles had an impact on monocyte and neutrophil phagocytosis. This can be seen in the central and right panels of Figure 27. Especially the infusion of the particles lead to a significant increase in phagocytic capacity *in vitro*. Angioplasty also enhanced uptake. Even though the measured effect of angioplasty on phagocytosis was less than the one observed for the infusion, recall that flow cytometry was performed three days after angioplasty on blood samples drawn just ahead of the infusion. After another three day recovery period between the infusion and MR Imaging, phagocytic capacity approached its baseline value.

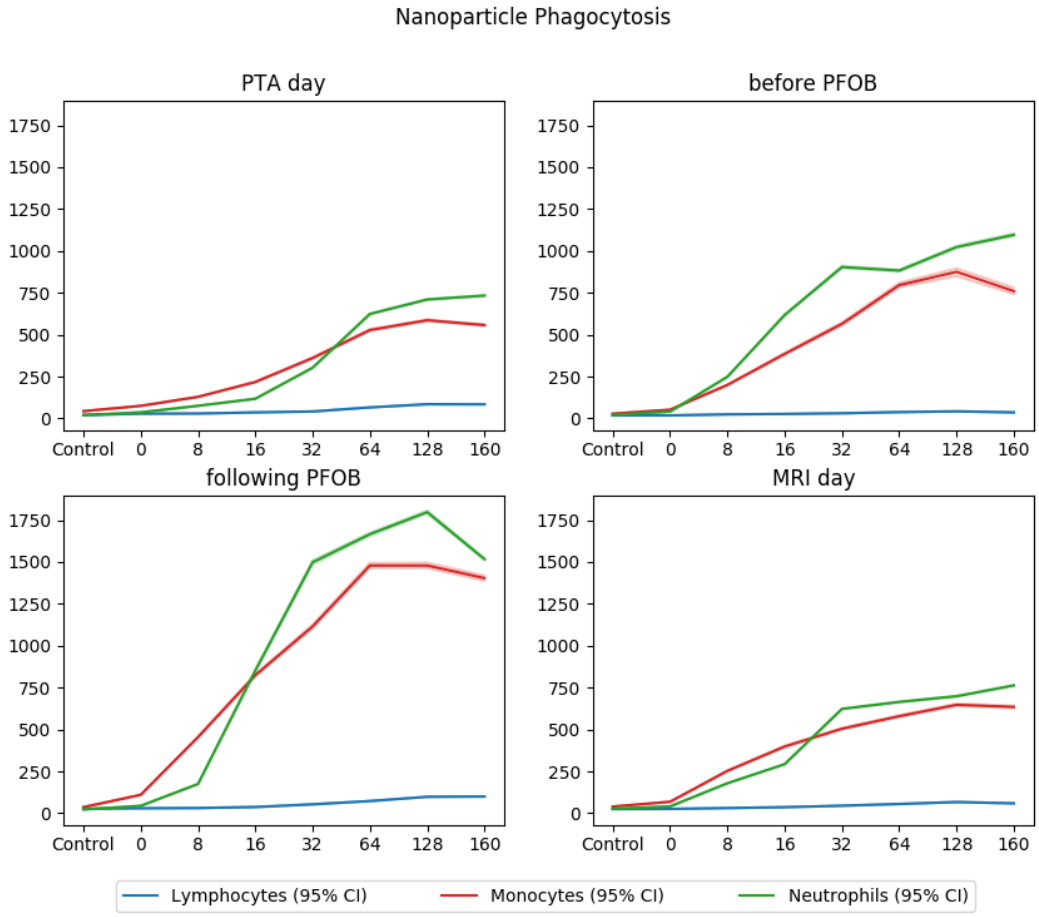

Figure 26: Time course of nanoparticle phagocytosis. The *in vitro* uptake of PFC (based on FITC fluorescence intensity) by different porcine leukocyte subtypes is shown over the course of 160 minutes. Values are grouped by the day at which the measurement was performed. The shaded areas around the curves indicate the 95% confidence intervals.

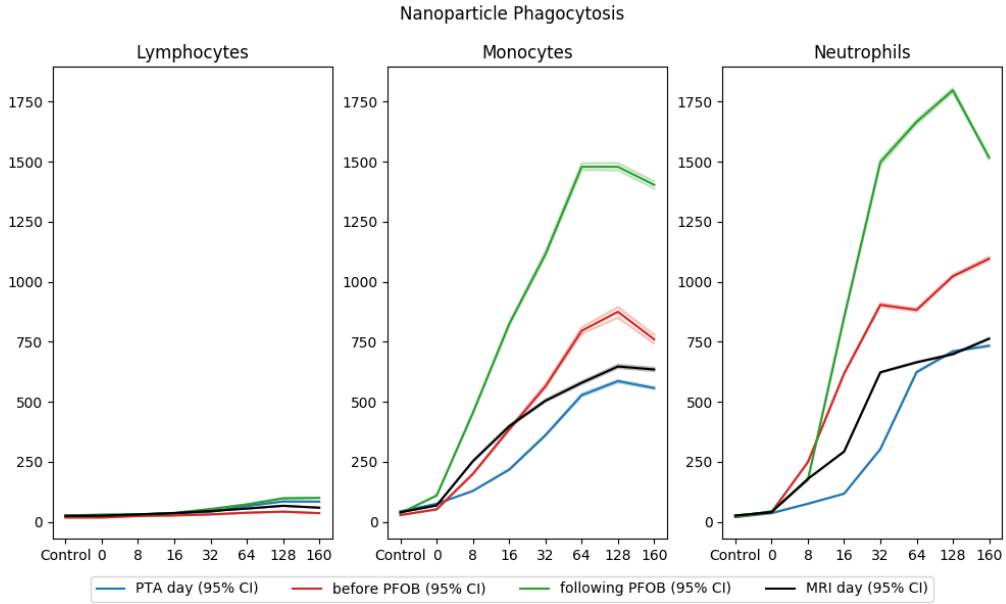

Figure 27: Time course of nanoparticle phagocytosis. The *in vitro* uptake of PFC (based on FITC fluorescence intensity) by different porcine leukocyte subtypes is shown over the course of 160 minutes. Values are grouped by the investigated cell populations. The shaded areas around the curves indicate the 95% confidence intervals.

3.5.2 Cell Granularity

Cell granularity was used as a further marker indicating the extent of nanoparticle uptake. Notice, that there is an interesting property of granularity as opposed to measuring *ex vivo* fluorescent labeled nanoparticle uptake: Assessment of granularity allows a retrospective estimation of nanoparticle phagocytosis *in vivo*. This is due to the fact that PFC-nanoparticles phagocytosed *in vivo* remain as granules inside the cellular cytoplasm without undergoing major metabolic processes. These granules then cause a diffraction of the flow cytometer's laser as cells pass through the instrument leading to increased side scatter (reported as granularity in Figure 28).

Cell granularity differed depending on cell type, time at which the blood sample was drawn, and duration of *in-vitro* incubation with Perfluorocarbon nanoparticles. Lymphocyte granularity did not show major alterations after prolonged *in vitro* PFOB incubation or in relation to angioplasty. Infusion of PFOB caused a minor increase in granularity suggesting a low amount of *in vivo* particle uptake. In contrast, monocytes showed both a significant increase in granularity with prolonged *in vitro* incubation and in blood samples drawn immediately after PFOB infusion. The latter finding is indicative of marked *in vivo* uptake since only samples drawn after the infusion exhibited this change from baseline granularity. Neutrophil granularity did not show a discernible pattern regarding *in vitro* incubation, angioplasty, or nanoparticle infusion.

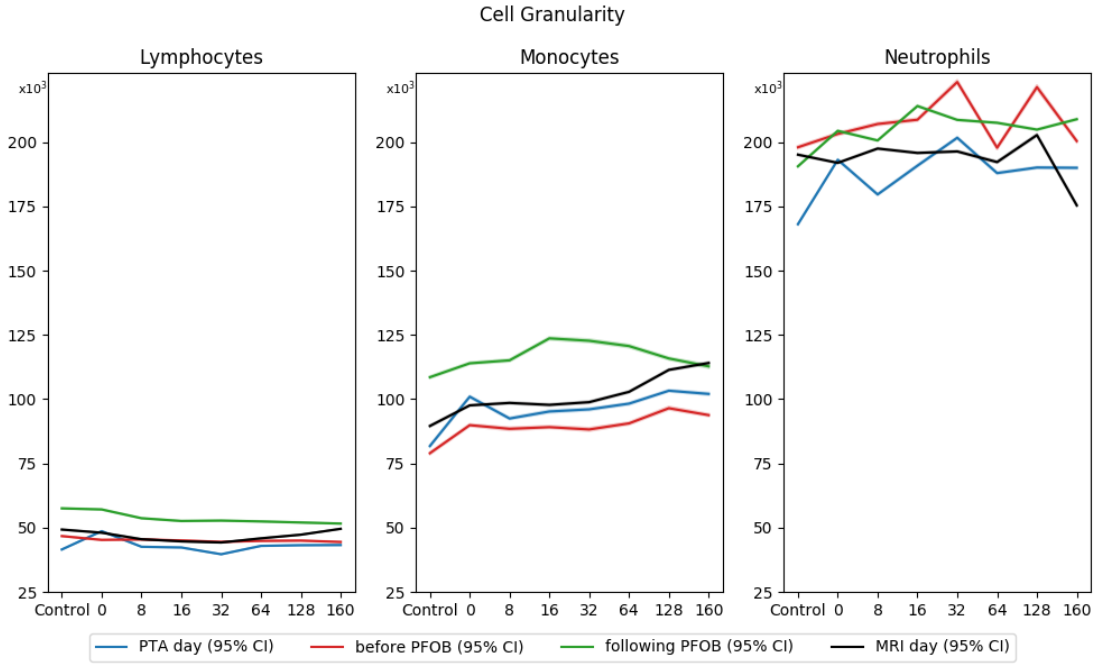

Figure 28: Granularity of porcine leukocyte subtypes. Changes in cell granularity (based on Side scatter) measured *in vitro* after different durations of exposure to PFC are shown, grouped by leukocyte population. The shaded areas around the curves indicate the 95% confidence intervals.

4 Discussion

The proposed pig model of vascular injury clearly showed that carotid angioplasty evokes a significant inflammatory response within the vessel wall. The severity of inflammation correlated strongly with the degree of endovascular injury. Further, we found that the histological markers of inflammation were associated with the magnitude of the measured ^{19}F signal intensity.

4.1 Use of a Porcine Model

As noted in section 1.3.3, the applicability of the ^{19}F-MRI to visualize inflammation has been validated extensively in murine models of various inflammatory conditions. MR imaging in mice is usually performed in experimental scanners capable of generating high magnetic field strengths of 9.4 T. This is opposed to clinical scanners which typically use field strengths of 1.5 T to 3 T. At higher magnetic field strengths the signal to noise ratio increases. The result is a proportional increase in spatial resolution (Ladd, 2007). This improves detection of small sources of signal. In contrast, pig models are more resemblant of a future clinical application because magnetic resonance imaging of pigs is performed in clinical scanners and, as the body size of pigs is larger, it becomes more challenging to handle MR receiver coils in a fashion that sufficient signal is detected by the scanner.

Despite these technical challenges, differences in physiology between species suggest greater ^{19}F signal intensities in pigs than in mice when imaging similar pathological processes. For example, mice show a much greater resilience to inflammation. That is, the inflammatory reaction induced by equivalent stimuli is smaller in murine than in porcine/human tissues. This difference may be due to a tradeoff between susceptibility to pathogens and the limitation of damage induced by inflammation (Warren et al., 2010; Seok et al., 2013). Additionally, the extent of perfluorocarbon (PFC) nanoparticle uptake differs markedly between porcine and murine monocytes. The latter were shown to internalize significantly smaller amounts of PFC than pig monocytes. While the amount of PFC uptake in pigs is closer to values demonstrated for human monocytes, the uptake is still distinctly lower than in human monocytes (Bönner et al., 2015).

4.2 Induction of Inflammation by Angioplasty

The primary goal of our experiments was to show that angioplasty-induced inflammation can be detected by ^{19}F MR imaging. The results clearly show that endovascular treatment as described in Section 2.1 led to a significant amount of inflammation in the carotids. In line with current mechanistic concepts observed across virtually all tissues (Chen et al., 2018; Frangogiannis et al., 2002; Libby, 2007), we considered two histological features to be the main indicators of an inflammatory response: (1) Immune cell infiltration and (2) activation of resident non-immune cells. Activation of vascular resident cells (mainly myofibroblasts) after PTA is characterized by a major proliferation of these cells (Labinaz et al., 1999; Scott et al., 1996; Shi et al., 1996). Both immune cell infiltration and resident cell proliferation were unequivocally identified in our microscopic specimens.

In addition, cellular infiltration after coronary artery PTA was shown to follow a certain time course (Okamoto et al., 2001). Typically, the first type of immune cell noted in the blood vessel wall were neutrophils while some time later macrophages constituted the main leukocyte population. Both cell types were found predominantly in the adventitia of the artery. As early as 30 minutes after injury, there was an accumulation of neutrophils which peaked at about six hours and disappeared by day seven. Macrophages showed a delayed pattern of infiltration with appearance, peaking, and disappearance occurring at 1, 3, and 14 days after injury, respectively. Other authors report the persistence of a mononuclear cell infiltrate in the adventitia of porcine coronary arteries until day 21 post PTA (Rud Andersen et al., 1996). Since our

point of histological observation was the seventh day after injury, we could not observe the early changes described above. Still, the pattern and time course of inflammation induced by carotid angioplasty was consistent with the findings by Okamoto et al.: (1) Immune cells were rarely encountered in untreated vessels, (2) after injury, macrophages were observed in large numbers in the vessel wall, (3) there was a major increase in $CD163^{-}$ cells indicating a resident cell response, (4) both macrophage infiltration and resident cells were predominantly located in the adventitia with significantly smaller increases in cellularity noticeable in the media.

The relative magnitude of the resident cell reaction in our experiments was comparable to findings after coronary angioplasty by Shi et al. (1996). The authors report a near doubling of cells in the adventitia after coronary angioplasty. We found a two- to threefold increase in median cell counts. Of notice, the baseline cellularity in the coronary arteries was markedly higher at 3880 cells/mm^2 (compare to 528/mm^2 in our experiments). Thus, the absolute magnitude of the inflammatory response was much larger in the coronary territory. Since our experiments involved carotids, it is worth pointing out that the tissue response to angioplasty was shown to differ significantly between carotid and coronary blood vessels (Badimon et al., 1998). Thrombosis and intimal hyperplasia developed to a greater extent in cardiac vessels than in the carotids. This finding was hypothesized to be due to differences in anatomy (muscular vs. elastic arteries) and blood flow patterns (turbulent vs. laminar flow) in the two vascular territories. Because the degree of intimal hyperplasia is positively correlated with the local extent of inflammation (Kornowski et al., 1998), it can be assumed that the PTA-induced inflammatory response tends to be greater in coronary vessels than in the carotids. This observation may explain why the absolute cell density in the found in coronary arteries exceeds the density measured in our experiments.

The absolute numbers of cell counts after endovascular injury provide little insight into their clinical significance, however. It may therefore be useful to set them into perspective by comparison to a known pathological process. As stated in Section 1.2.2, a future clinical application of our research could be the imaging of inflammatory reactions associated with atherosclerotic plaques as an increased macrophage density was found in plaques prone to rupture (Virmani et al., 2006a; Howard et al., 2015; Moroni et al., 2019). Thereby, with ^{19}F imaging, it may become possible to distinguish vulnerable lesions from stable ones and guide management accordingly. Currently, we could identify only three papers which report absolute numbers of immune cells per unit area in atherosclerotic plaques. Two studies determined the number of macrophages/mm^2 in human carotid endarterectomy specimens. Zheng et al. (2019) report that macrophage counts in carotid endarterectomy specimens differed depending on the pathological assessment of the stability of the plaque. 44, 79, 297, and 157 macrophages/mm^2 were found in the cap of plaques characterized as definitely stable, probably stable, probably unstable, and definitely unstable, respectively. Endarterectomy specimens examined by Joshi et al. (2014) harbored between ~24 and 840 macrophages/mm^2. The cell density differed depending on the presence of ^{18}F-NaF enhancement on PET imaging in the vessel region containing the histological section. Cell counts from tissue that exhibited ^{18}F-NaF uptake were significantly higher at 350 cells/mm^2 (IQR 172-840) as compared to regions without tracer uptake (145/mm^2, IQR 24-362/mm^2). ^{18}F-NaF enhancement was shown to be be related to clinical and histological signs of plaque instability (see Section 1.3.2). Homma et al. (2008) measured the macrophage density in the left anterior descending coronary artery (LAD) and in the thoracic and abdominal aorta of individuals between 15 and 34 years of age who died of unrelated causes. 96, 59, and 46 macrophages/mm^2 were found in the thoracic aorta, abdominal aorta, and LAD, respectively, of these adolescents and young adults. From the above data, we conclude that vulnerable plaques contain roughly 200 to 400 macrophages/mm^2. For reasons outlined in Section 4.4, the ^{19}F signal intensity evoked by human macrophages may be ~1.5 times greater than the respective porcine macrophage-induced signal. Hence, we make the assumption that unstable human atherosclerotic plaques give rise to ^{19}F signal equivalent to a cell density of approximately 300 to 600 porcine macrophages/mm^2. The median number

of $CD163^+$ cells in our experiments were 281/mm^2 in the mild injury group and 705/mm^2 in the severe injury group. Comparing these numbers to those measured by Zheng et al., Joshi et al., and Homma et al., suggests a similar order of magnitude for macrophage counts in the mild injury group and counts found in the cap of microscopically unstable carotid plaques. This finding highlights that the ^{19}F MRI may be capable of visualizing such unstable lesions. Given that our assumption holds and human macrophages do evoke greater ^{19}F signals than their porcine counterparts, ^{19}F signal intensities induced by atherosclerotic plaques may actually exceed the signal measured in our mild injury group. Conversely, the density of macrophages in stable carotid plaques and in arteries of presumably healthy individuals was much lower. Thus, we would assume that unstable atherosclerotic lesions containing ~300 macrophages/mm^2 evoke a measurable ^{19}F signal in a future clinical setting while insignificant and stable lesions would remain below the detection threshold or generate a considerably weaker ^{19}F signal.

4.3 Vessel Wall Remodeling

In the era before the routine use of drug-eluting stents for treatment of relevant arterial stenoses, a major setback of endovascular intervention was the high rate of restenosis development after the procedure (Serruys et al., 1993; Brar et al., 2009). Restenosis was attributed to the structural remodeling processes induced by balloon-angioplasty or bare-metal stenting. Therefore, the underlying cellular mechanisms of restenosis were a major focus of research at that time (Rud Andersen et al., 1996; Labinaz et al., 1999; Mæng et al., 2001; Okamoto et al., 2001; Scott et al., 1996; Shi et al., 1996). Today's drug-eluting stents led to a change in the tissue response to the mechanical stress induced by the intervention. Therefore, the current mechanisms of restenosis differ markedly from those at play after angioplasty or bare-metal stenting (Shlofmitz et al., 2019). Because the predominant clinical domain of angiographic interventions are the coronary arteries (Statistisches Bundesamt, 2018; Fleck et al., 2020), most experimental investigations concerning angioplasty-induced remodeling in porcine models focused on coronary vessels while data involving carotid arteries is less abundant.

In our context, the term *vessel wall remodeling* was used to denote any structural changes within the compartments of the carotid wall. Remodeling processes are functionally important since the resultant structural changes of the vessel wall can ultimately cause a narrowing of the arterial lumen. Therefore, some authors denote by *remodeling* specifically those changes that lead to a luminal compromise (Labinaz et al., 1999). Previous studies show that the major feature of early coronary arterial remodeling after angioplasty is the formation of a neoadventitia created by massive deposition of collagen and proteoglycans by myofibroblasts (Rud Andersen et al., 1996; Labinaz et al., 1999; Shi et al., 1996). Neoadventitial development could be noted as early as day 3 after treatment. By day 7, the neoadventitial thickness plateaued in most studies (Labinaz et al., 1999; Mæng et al., 2001; Shi et al., 1996). Results by Mæng et al. indicate that after long follow-up periods (56 days post-intervention) adventitial thickness begins to decline. Development of a neointima was found to occur later in the remodeling process than neoadventitial formation. Typically it was first noted 7 days after injury, and by day 14 it was well developed (Labinaz et al., 1999; Mæng et al., 2001). The finding that neoadventitia development preceded the intimal changes led to the hypothesis that there may be a migration of cells from the adventitia towards the lumen which are then involved in the formation of the neointima. Experiments by Scott et al. support this concept.

Our findings blend in well with previous research on this topic. Endovascular injury almost invariably led to a thickening of the adventitia characterized by a strong stromal reaction with deposition of large amounts of connective tissue and extracellular matrix. Further, the vast majority of $CD163^+$ cells were located in the adventitia while the few cells found in the media were mainly seen in close proximity to the adventitia, possibly indicating a migration towards the lumen. The lack of a relevant amount of inti-

mal hyperplasia in our experiments may be due to two potential causes: (1) As noted above, neointima formation could occur in a later phase of vessel remodeling, (2) in carotid arteries intimal hyperplasia may develop to a lesser extent than in coronaries (Badimon et al., 1998).

4.4 Nanoparticle Phagocytosis

Ex vivo nanoparticle phagocytosis can be demonstrated in porcine blood samples by both monocytes and neutrophils. Thus, both cell types can serve a carriers for nanoparticles into foci of inflammation. In human blood samples, however, significant nanoparticle uptake is only measurable in monocytes (Nienhaus et al., 2019). Despite this difference in physiology, we do not consider neutrophils to be a major source of ^{19}F signal at day 7 after PTA. This is due to the sequential pattern of immune cell infiltration into the vessel wall after injury described in Section 4.2: Within a few days neutrophils disappear from the tissue. Consequently, monocytes/macrophages likely constitute the main nanoparticle-loaded cell type within the carotid wall at day 7 after treatment and thus are the predominant source of ^{19}F. Therefore, we regard the cell density proposed in Section 4.2 as a solid estimate of the number of monocytes/macrophages in human tissues that would suffice to generate a reproducible ^{19}F signal.

However, even though ~300 macrophages/mm^2 may be an accurate quantitative estimate of the number of cells necessary for detection by the ^{19}F MRI in our experiment, the amount of nanoparticles inside these cells could be greater than measured by *ex vivo* flow cytometry. During the resolution of inflammatory processes macrophages internalize apoptotic neutrophils in a process termed efferocytosis (Sugimoto et al., 2016; Nathan, 2006). Thereby, the local macrophages would also take up the nanoparticles within the neutrophils causing each cell to generate a greater ^{19}F signal than predicted *ex vivo*. This point is especially noteworthy since neutrophils commonly outnumber macrophages by two orders of magnitude at inflammatory foci (Nathan, 2006). Efferocytosis is an established mechanism that can impair MRI-based cell tracking using particles of iron oxide (Winter et al., 2010). Hence, ^{19}F imaging of human tissues could require a much larger macrophage infiltration due to the missing contribution of nanoparticle uptake by efferocytosis. However, taking into account differences in elimination kinetics, it appears unlikely that the effect of efferocytosis demonstrated for particles of iron oxide also applies to PFC nanoparticles: After macrophages take up perished neutrophils into phagosomes, the phagosomes are fused with lysosomes in order to degrade their contents (Boada-Romero et al., 2020). At this point, the fate of PFC and iron oxide nanoparticles probably differs: Lipids (and thus the lipid coating of PFC) are broken down by lysosomal enzymes (Xu and Ren, 2015). This liberates the PFC which can then diffuse into the blood to be finally released by exhalation (see Spahn (1999) and Section 1.3.3). On the contrary, the results by (Winter et al., 2010) indicate that either the iron oxide particles or their iron content remain inside the phagocytes for longer time periods. Thus, from a mechanistic point of view point, the effect of efferocytosis on the measured signal in our experiments is likely small. Notice, that there is yet another factor to take into consideration: The capacity for nanoparticle uptake by different phagocyte subsets is species dependent. Bönner et al. (2015) reported that human monocytes internalized about 1.5-fold as many nanoparticles as porcine monocytes. Since the amount of nanoparticles inside a tissue is proportional to the measurable ^{19}F signal (Rothe et al., 2019), human macrophages would induce about 1.5 times as much ^{19}F enhancement as the same number of porcine macrophages. Therefore, we argue that actually fewer human nanoparticle-loaded macrophages would suffice to evoke the same amount of ^{19}F signal as compared to the pig model.

Another mechanism at play in ^{19}F based detection of inflammation was demonstrated in a preclinical study by Zhang et al. (2011): ^{19}F nanoparticles diffused into atherosclerotic lesions through the endothelial barrier. Accordingly, ^{19}F enhancement as seen on MRI may also reflect nanoparticle diffusion into the vascular wall rather than exclusive transport by immune cells. While we cannot exclude that passive

processes caused or contributed to the nanoparticle accumulation in the carotids after PTA, in our regard, it is not likely from a histologic point of view. If nanoparticle accumulation were due to passive diffusion, we would expect much less of an association between ^{19}F signal intensity and the number of macrophages within the vessel wall. Since we found a positive correlation between the two parameters, we regard active transportation of nanoparticles by phagocytes as the more plausible mechanism underlying ^{19}F enhancement than diffusion.

4.5 Feasibility of the ^{19}F MRI to Detect and Quantify Inflammation at 3 T

As noted previously, a major advantage of higher field strengths in magnetic resonance imaging is the greater spatial resolution and the lower detection threshold for small sources of signal (Wüst et al., 2019). In murine imaging at 9.4 T, these benefits can be fully exploited such that the ^{19}F imaging of atherosclerosis-associated inflammation becomes possible (Van Heeswijk et al., 2015). In our translational approach of imaging inflammation of porcine blood vessels at 3 T, the lower field strength imposed one of the main challenges to overcome.

The capability of the ^{19}F MRI for detection of larger sources of inflammation at 3 T was proven in experimental models of myocardial infarction *ex vivo* (Bönner et al., 2015) and *in vivo* (Rothe et al., 2019; Bönner et al., 2022). Here, we showed that the substantially smaller angioplasty-induced inflammatory response could also be reliably detected *ex vivo*. Even in the mild injury subgroup, ^{19}F enhancement was found in all carotids. In addition, the high specificity of the method was evident as none of the untreated vessels gave rise to a measurable ^{19}F signal.

Even though the sensitivity of the ^{19}F MRI to detect the overall presence of ^{19}F sources was remarkably high, the precise colocalization of the signal and macrophages seen on histology required stronger sources of signal. This is illustrated in Figure 24 of Section 3.4. Recall, the Figure delineated the relation between CD163^{+} cells in the adventitia and ^{19}F signal. The red lines indicate the association between the cell count and MRI signal in the severe injury subgroup as determined by linear regression. Overall, there was a moderate positive correlation (solid line). However, including two different regression lines for the severe injury subgroup (dashed and dashdotted lines) highlights that a strong positive association is noticeable for cell counts >350/mm^2 while lesser cell densities are not consistently positively correlated with the number of macrophages. Accordingly, in the mild injury subgroup, in which most cell counts were below 350/mm^2, the association between increments in cell density and ^{19}F was also small (0.9 units/100 cells). Thus, it is possible to detect ^{19}F signal in tissues with cell counts less than ~350/mm^2 but the predicted linear relationship between PFC-nanoparticle carrying cells and MRI signal is not unequivocally appreciable. Conversely, counts beyond 350/mm^2 are markedly positively correlated with ^{19}F signal and, based on the data in the Figure, a linear relationship seems plausible.

This conclusion is also consistent with Figure 25 which delineates the relationship between macrophages and ^{19}F signal in a single vessel. Histology reveals the maximum of cellular infiltration in the proximal part of the artery. With further distance from the bifurcation, cell counts gradually decrease to finally return to levels comparable to those found in untreated vessels. The ^{19}F signal intensity generally mirrors this proximal to distal gradient but the tapering of signal occurs much faster than that observed for the cell counts. Once the cell density drops below a certain threshold, the detectable amount of ^{19}F signal is small and is no longer related to changes in cellularity in any discernible fashion. Again, this highlights that the current capability of the ^{19}F MRI at 3 T to precisely quantify very small nanoparticle accumulations is limited.

As noted in Section 1.2.2, one of the main histological features associated with an increased risk for atherosclerotic plaque rupture is the extent of macrophage infiltration. In human carotid endarterectomy specimens exhibiting histological signs indicative of a tendency to rupture, a macrophage density of ~200

to 400/mm^2 was found (see Section 4.2). Due to the fact that the capacity for nanoparticle uptake by human macrophages exceeds the respective porcine uptake capacity (Bönner et al., 2015), we argue that the ^{19}F signal emitted by 200 to 400 macrophages in human tissues is equivalent to ~300 to 600 cells in pigs. Our finding that macrophage counts >350/mm^2 are strongly correlated with ^{19}F signal implies that the ^{19}F MRI is not only capable of detecting rupture-prone atherosclerotic lesions, but could also quantify the number of macrophages within. Such a precise characterization of plaque composition may permit the risk stratification of atheromatous plaques and thereby guide patient management. Assuming a current reliable detection threshold of 350 porcine macrophages ($\cong$ 235 human macrophages), some vulnerable plaques would still go unnoticed, though. Zheng et al. (2019) reported a macrophage density of 157/mm^2 in certain at-risk lesions. With further advances regarding MR imaging protocols and receiver coil handling, ^{19}F based diagnosis of such lesions at 3 T may also become achievable. In that context, it is especially noteworthy, that atherosclerotic lesions across different vascular territories vary in their microscopic structure. Virmani et al. (2006b) report the presence of 13.5 $\pm$10.9% macrophages in the fibrous cap of ruptured carotid plaques, whereas their coronary counterparts harbored 26 $\pm$20% macrophages. The fraction of macrophages in vulnerable carotid and coronary plaques was 10 $\pm$1.8% and 14 $\pm$10%, respectively. Due to the greater macrophage density in coronary plaques, cardiac atherosclerosis may actually be a more suitable target for detection by ^{19}F imaging despite the greater distance between the signal source and the receiver coil.

4.6 Value of Differential Atherosclerosis Imaging

In addition to ^{19}F MR imaging, a wide spectrum of alternative approaches to image atherosclerotic lesions are currently used in practice or are evaluated in clinical and preclinical studies (Syed et al., 2019; Tarkin et al., 2016). Many of these methods aim to identify factors which allow an assessment of the vulnerability of atherosclerotic plaques. Intuitively, modalities that yield information about the internal composition of a plaque provide the most accurate prognostic information due to the close interrelation between plaque histology and rupture risk (Virmani et al., 2006a; Howard et al., 2015).

High resolution invasive imaging modalities like optic coherence tomography and intravascular ultrasound provide a very detailed characterization of plaque morphology such that conclusions about plaque vulnerability can be drawn (Tearney et al., 2003; Jang et al., 2005; Štěchovskỳ et al., 2016) As these are invasive methods, they are unsuitable for routine use in low risk patient populations, though. Thus, there is a need for non-invasive techniques able to delineate plaque morphology (Syed et al., 2019; Tarkin et al., 2016). Promising imaging techniques in this field include MRI and Positron emission tomography (PET) using special contrast agents. Conventional CT or MRI provide only limited information about the composition of atherosclerotic plaques (Tarkin et al., 2016). Even at high magnetic field strengths of 7 T, no correlation between MR imaging and the histological structure of atherosclerotic lesions could be found (de Rotte et al., 2014). Thus, a number of sophisticated imaging techniques are currently investigated in preclinical and clinical studies to address the need of non-invasive plaque characterization (see Section 1.3).

In our experiments, we have shown that the ^{19}F MRI may be a valuable tool with regards to atherosclerosis imaging due to being (1) widely available, (2) non-invasive, (3) independent of ionizing radiation, and (4) sensitive to intraplaque morphology. Notice, we evaluated the properties of single contrast enhanced imaging using an untargeted nanoemulsion. Results from Flögel et al. (2021) obtained in mice show that targeted ^{19}F contrast agents can also be used for MRI-based delineation of pathophysiological relationships. Coupling PFC to macromolecular polyethylenglycol (PEG) prevents the uptake of PFC by monocytes after intravenous administration (Temme et al., 2015). As demonstrated by Wang et al. (2020), PFC can be functionalized before PEGylation by antibody-attachment. Thereby, specific epi-

topes can be marked via infusion of the PFC nanoemulsion. This would allow the visualization of very specific cell types by ^{19}F MRI. In addition, Flögel et al. (2021) demonstrated that ^{19}F MR imaging is not limited to the use of a single contrast agent: The authors report that multitargeted nanoemulsions with different ^{19}F agents identified by multi chemical shift selective imaging were capable of detecting a broad range of antigens important in the development of atherosclerosis ("multi-color-imaging"). As noted in Section 1.2.2, atherosclerotic plaques have different histologic morphologies and thus cellular compositions which correlate with clinical outcome parameters. Therefore, a detailed characterization of a plaque's internal structure is the prerequisite for an accurate patient risk stratification. Results summarized by Moroni et al. (2019) show that there were conflicting findings regarding the association between the extent of carotid plaque macrophage infiltration and prospectively observed clinical outcome parameters. Howard et al. (2015) found that the extent of overall macrophage infiltration in carotid endarterectomy specimens correlated with subsequent stroke risk while Hellings et al. (2010) could not reproduce this result. This supports the hypothesis that plaque macrophages do not constitute a homogeneous entity. Accordingly, De Gaetano et al. (2016) could show that the presence of M1 macrophages was associated with symptomatic carotid plaques while M2 macrophages were predominant in plaques from asymptomatic patients. Still, even the distinction of macrophages into M1 and M2 subsets and their subsequent quantification may not sufficiently capture the cellular impact on plaque progression to have a significant discriminating value between low and high risk plaques. This was shown by van Dijk et al. (2016) in cadaveric aortic specimens where both the presence of M1 and M2 macrophages within a plaque was strongly indicative of the plaque being histologically classified as progressive. A prospective study which investigated macrophage subpopulations more precisely revealed that the fraction of *matrix metalloproteinase 12* expressing macrophages in carotid endarterectomy specimens was significantly associated with the occurrence of MACE within a follow-up period of three years (Scholtes et al., 2012). Similarly, Bengtsson et al. (2020) reported that an increased number of CD163^{+} macrophages in carotid endarterectomy specimens was related to cerebrovascular symptoms. Hence, a very detailed characterization of macrophage subpopulations may be required to reliably predict clinical outcomes. Accordingly, there may be a future clinical demand to detect different antigens simultaneously. This would necessitate multi contrast imaging. As noted above, the ^{19}F platform could satisfy this demand by administering different PFC with different structural or antigenic targets. Such a non-invasive molecular imaging modality could be used to screen for high risk plaques in asymptomatic patients.

As noted in Section 1.3.2, PET-based detection of vulnerable atherosclerotic lesions has shown promising results in a number of clinical trials. However, comparing ^{19}F-based imaging of atherosclerosis to PET, there are a number of factors that favor the use of the ^{19}F MRI: (1) Currently, MR-scanners are more accessible than PET-scanners and usually there are lesser costs. (2) There is no requirement for ionizing radiation exposure which lowers the threshold for imaging younger patients or ordering repeat examinations. (3) PET studies rely almost exclusively of the radionuclide ^{18}F whose half-life is ~110 minutes. This precludes an assessment of longer pathological processes like cell migration. The 3-4 day half-life of PFOB nanoemulsions is more suitable for that purpose. (4) The presence of insulin-dependent Diabetes mellitus may negatively affect ^{18}FDG PET imaging. Even though research on comparably large inflammatory sources (such as fever of unknown origin, diabetic foot, or vascular graft infection) did not reveal any significant impairment of PET sensitivity in diabetic patients (Rabkin et al., 2010), this issue may still be relevant considering the small size of inflammation in atheromas. (5) As noted above, experimentally it is possible to visualize multiple pathological processes in a single session by combining different ^{19}F contrast-agents. Thereby, it may be possible to raise the diagnostic accuracy of the ^{19}F MRI further. Conversely, multi contrast PET imaging is challenging and highly susceptible to noise (Kadrmas and Hoffman, 2013).

Section 1.3.3 reviews research on small/ultrasmall paramagnetic particles of iron oxide (SPIO/

USPIO) as MR contrast agents with regards to their potential to delineate vulnerable atherosclerotic plaques. Here, we point out distinct advantages of ^{19}F contrast enhancement as compared to USPIO for the purpose of plaque detection. (1) Iron oxide particle contrast imaging can be relatively unspecific due to the fact that particle deposition is reflected by hypointensities on ^{1}H images. Thus, any other process causing a hypointensity in an image such as hemorrhage, cortical bone, and air spaces requires differentiation from USPIO accumulation (Makela et al., 2016; Liu and Frank, 2009). Consistently, in a study by Yilmaz et al. (2013), which investigated the capability of SPIO to characterize the inflammatory reaction after myocardial infarction, no SPIO hypoenhanced areas were found in the infarcted myocardium beyond the late Gadolinium enhanced territory. The authors hypothesized that this finding could be due to the presence of hemorrhage and edema that obscured the SPIO-induced hypoenhancement. ^{19}F, in contrast, is highly specific due to the negligible ^{19}F background in tissues (Wüst et al., 2019; Makela et al., 2016). (2) It is difficult to detect and quantify inflammation from USPIO-induced signal voids on MRI (Wüst et al., 2019; Liu and Frank, 2009) whereas the amount of ^{19}F contrast is proportional to the number of ^{19}F atoms per voxel (Rothe et al., 2019; Makela et al., 2016). (3) USPIO administration leads to signal voids for as long as the iron-particles remain inside a tissue. Thereby, the contrast agent may distort subsequent MR scans and negatively affect their diagnostic yield. ^{19}F administration does not interfere with other MR imaging techniques (Wüst et al., 2019).

Besides the detection of atherosclerotic plaques in treatment-naive patients, there is the medical need to identify patients at risk of neoatherosclerosis after angioplasty. Compared to bare-metal stents, drug-eluting stents have the advantage that the rate of early restenosis is reduced by inhibition of intimal overgrowth (Brar et al., 2009). Therefore, drug-eluting stents are used in the majority of patients nowadays. Despite preventing early restenosis, it was shown that the rate of neoatherosclerosis development within the extents of the stent is significantly greater when using drug-eluting stents (Otsuka et al., 2015). Histological analyses revealed that inflammation with intimal accumulation of foam cells and calcification are central morphologic patterns of neoatherosclerosis (Otsuka et al., 2015). In line with these findings, a prospective observational cohort study could demonstrate that PET imaging of vessel wall glucose uptake (^{18}F-FDG) and microcalcification (^{18}F-NaF) could predict restenosis following limb angioplasty (Chowdhury et al., 2020). Thus, already bulk identification of vessel wall surrogates of inflammation predicts restenosis. We have shown, that the ^{19}F MRI with an untargeted nanoemulsion can directly image and quantify monocytes/macrophages. The specificity of this approach can even be improved by functionalizing the nanoemulsion as described above to target M1 and M2 macrophages or more distinct macrophage subtypes. In addition to its potential value in the identification of vulnerable atherosclerotic plaques, this imaging platform could provide a complete phenotyping of vascular healing after angioplasty with the major advantage of a positive, specific, and quantifiable signal.

In the present study, using an untargeted nanoemulsion, we were able to directly visualize the monocyte/macrophage lesion burden in a quantitative manner with a resolution sufficient for improved vascular wall mapping of the signal. This makes the ^{19}F MRI a promising modality for vessel imaging that may play a central role in future research on and apparative diagnostic of vessel disease.

4.7 Conclusion

In our experiments, we examined whether the ^{19}F MRI could be a suitable imaging modality for the identification of unstable atherosclerotic lesions. ^{19}F imaging at 3 T proved to be capable of detecting even small numbers of cells containing PFC-nanoparticles. The number of cells per unit area required for reproducible *ex vivo* detection by ^{19}F MRI was in a similar range as the cell density found in the cap of vulnerable atheromas. In our regard, it is therefore probable that the *ex vivo* detection of unstable atheromatous lesions using a ^{19}F-based approach is possible. Since many individuals with vulnerable atherosclerotic plaques remain asymptomatic until the time of plaque rupture, screening of the at-risk population would be necessary to identify patients that would benefit from a preventive catheter intervention. In addition to being one of the few methods for which there is experimental evidence that the detection of vulnerable atherosclerotic plaques is possible, the ^{19}F MRI offers a number of advantages that are particularly useful in the setting of screening: (1) ^{19}F imaging can be performed on regular MRI platforms which are widely available for patients. (2) No exposure to ionizing radiation is required which permits studies in younger patients and repeat examinations if needed. (3) The high specificity ensures that the number of false positive results is minimized.

Due to the current scarcity of methods that allow the identification of patients at high risk for atherosclerotic plaque rupture, the ^{19}F MRI may become an invaluable tool for this purpose. Our proof-of-concept study showed that small sources of vascular inflammation can be identified on ^{19}F imaging. Still, further research on ^{19}F-based atherosclerosis imaging is necessary. These investigations are needed to confirm that atherosclerotic plaques can, in fact, be detected in clinical MR-scanners *ex vivo* and *in vivo*. Further, the correlations between potential ^{19}F-enhanced plaques and their associated histological findings as well as the plaques' natural history will have to be assessed in order to evaluate whether ^{19}F-enhanced plaques do exhibit the postulated instability.

5 Bibliography

Alexios S Antonopoulos, Fabio Sanna, Nikant Sabharwal, Sheena Thomas, Evangelos K Oikonomou, Laura Herdman, Marios Margaritis, Cheerag Shirodaria, Anna-Maria Kampoli, Ioannis Akoumianakis, et al. Detecting human coronary inflammation by imaging perivascular fat. *Science translational medicine*, 9(398):eaal2658, 2017.

Takayuki Asahara, Christophe Bauters, Christopher Pastore, Marianne Kearney, Susan Rossow, Stuart Bunting, Napoleone Ferrara, James F Symes, and Jeffrey M Isner. Local delivery of vascular endothelial growth factor accelerates reendothelialization and attenuates intimal hyperplasia in balloon-injured rat carotid artery. *Circulation*, 91(11):2793–2801, 1995.

Juan Jose Badimon, Antonio Fernandez Ortiz, Beat Meyer, Alessandra Mailhac, John T Fallon, Erling Falk, Lina Badimon, James H Chesebro, and Valentin Fuster. Different response to balloon angioplasty of carotid and coronary arteries: effects on acute platelet deposition and intimal thickening. *Atherosclerosis*, 140(2):307–314, 1998.

Eva Bengtsson, Karin Hultman, Andreas Edsfeldt, Ana Persson, Mihaela Nitulescu, Jan Nilsson, Isabel Gonçalves, and Harry Björkbacka. Cd163+ macrophages are associated with a vulnerable plaque phenotype in human carotid plaques. *Scientific reports*, 10(1):1–9, 2020.

Martin R Bennett, Sanjay Sinha, and Gary K Owens. Vascular smooth muscle cells in atherosclerosis. *Circulation research*, 118(4):692–702, 2016.

Katarina E Berg, Irena Ljungcrantz, Linda Andersson, Carl Bryngelsson, Bo Hedblad, Gunilla N Fredrikson, Jan Nilsson, and Harry Björkbacka. Elevated cd14++ cd16- monocytes predict cardiovascular events. *Circulation: Cardiovascular Genetics*, 5(1):122–131, 2012.

Emilio Boada-Romero, Jennifer Martinez, Bradlee L Heckmann, and Douglas R Green. The clearance of dead cells by efferocytosis. *Nature Reviews Molecular Cell Biology*, 21(7):398–414, 2020.

F Bönner, MW Merx, K Klingel, P Begovatz, U Flögel, M Sager, S Temme, C Jacoby, M Salehi Ravesh, C Grapentin, et al. Monocyte imaging after myocardial infarction with 19f mri at 3 t: a pilot study in explanted porcine hearts. *European Heart Journal-Cardiovascular Imaging*, 16(6):612–620, 2015.

Florian Bönner, Mareike Gastl, Fabian Nienhaus, Maik Rothe, Annika Jahn, Susanne Pfeiler, Ulrich Gross, Heinz-Peter Schultheiss, Borja Ibanez, Sebastian Kozerke, Julia Szendroedi, Michael Roden, Ralf Westenfeld, Jürgen Schrader, Ulrich Flögel, Gerd Heusch, and Malte Kelm. Regional analysis of inflammation and contractile function in reperfused acute myocardial infarction by in vivo 19f cardiovascular magnetic resonance in pigs. *Basic Research in Cardiology*, 117(1):1–15, 2022.

Pascal Bouvain, Sebastian Temme, and Ulrich Flögel. Hot spot 19f magnetic resonance imaging of inflammation. *Wiley Interdisciplinary Reviews: Nanomedicine and Nanobiotechnology*, 12(6):e1639, 2020.

Somjot S Brar, Martin B Leon, Gregg W Stone, Roxana Mehran, Jeffrey W Moses, Simerjeet K Brar, and George Dangas. Use of drug-eluting stents in acute myocardial infarction: a systematic review and meta-analysis. *Journal of the American College of Cardiology*, 53(18):1677–1689, 2009.

B Greg Brown, Xue-Qiao Zhao, Dianne E Sacco, and John J Albers. Lipid lowering and plaque regression. new insights into prevention of plaque disruption and clinical events in coronary disease. *Circulation*, 87(6):1781–1791, 1993.

Marco Busnelli, Alberto Froio, Maria Laura Bacci, Massimo Giunti, Maria Grazia Cerrito, Roberto Giovannoni, Monica Forni, Fabio Gentilini, Alessandra Scagliarini, Gaetano Deleo, et al. Pathogenetic role of hypercholesterolemia in a novel preclinical model of vascular injury in pigs. *Atherosclerosis*, 207 (2):384–390, 2009.

Marco Busnelli, Stefano Manzini, Alberto Froio, Alessia Vargiolu, Maria Grazia Cerrito, Ryszard T Smolenski, Massimo Giunti, Alessandro Cinti, Augusta Zannoni, Biagio Eugenio Leone, et al. Diet induced mild hypercholesterolemia in pigs: local and systemic inflammation, effects on vascular injury–rescue by high-dose statin treatment. *PloS one*, 8(11):e80588, 2013.

Caroline Camaré, Mélanie Pucelle, Anne Nègre-Salvayre, and Robert Salvayre. Angiogenesis in the atherosclerotic plaque. *Redox biology*, 12:18–34, 2017.

Michael J Campbell and Martin J Gardner. Statistics in medicine: Calculating confidence intervals for some non-parametric analyses. *British medical journal (Clinical research ed.)*, 296(6634):1454, 1988.

Larissa Cardilo-Reis, Sabrina Gruber, Sabine M Schreier, Maik Drechsler, Nikolina Papac-Milicevic, Christian Weber, Oswald Wagner, Herbert Stangl, Oliver Soehnlein, and Christoph J Binder. Interleukin-13 protects from atherosclerosis and modulates plaque composition by skewing the macrophage phenotype. *EMBO molecular medicine*, 4(10):1072–1086, 2012.

Linlin Chen, Huidan Deng, Hengmin Cui, Jing Fang, Zhicai Zuo, Junliang Deng, Yinglun Li, Xun Wang, and Ling Zhao. Inflammatory responses and inflammation-associated diseases in organs. *Oncotarget*, 9(6):7204, 2018.

Gilles Chironi, Alain Simon, Nicolas Denarié, Benoit Védie, Valérie Séné, Jean-louis Mégnien, and Jaime Levenson. Determinants of progression of coronary artery calcifications in asymptomatic men at high cardiovascular risk. *Angiology*, 53(6):677–683, 2002.

Robin P Choudhury, Valentin Fuster, Juan J Badimon, Edward A Fisher, and Zahi A Fayad. Mri and characterization of atherosclerotic plaque: emerging applications and molecular imaging. *Atherosclerosis, Thrombosis, and Vascular Biology*, 22(7):1065–1074, 2002.

Ohn A Chow, Maren von Köckritz-Blickwede, A Taylor Bright, Mary E Hensler, Annelies S Zinkernagel, Anna L Cogen, Richard L Gallo, Marc Monestier, Yanming Wang, Christopher K Glass, et al. Statins enhance formation of phagocyte extracellular traps. *Cell host & microbe*, 8(5):445–454, 2010.

Mohammed M Chowdhury, Jason M Tarkin, Mazen S Albaghdadi, Nicholas R Evans, Elizabeth PV Le, Thomas B Berrett, Umar Sadat, Francis R Joshi, Elizabeth A Warburton, John R Buscombe, et al. Vascular positron emission tomography and restenosis in symptomatic peripheral arterial disease: a prospective clinical study. *Cardiovascular Imaging*, 13(4):1008–1017, 2020.

Richard A Cooper. Influence of increased membrane cholesterol on membrane fluidity and cell function in human red blood cells. *Journal of supramolecular structure*, 8(4):413–430, 1978.

Michael J Davies. The pathophysiology of acute coronary syndromes. *Heart*, 83(3):361–366, 2000.

Monica De Gaetano, Daniel Crean, Mary Barry, and Orina Belton. M1-and m2-type macrophage responses are predictive of adverse outcomes in human atherosclerosis. *Frontiers in immunology*, 7:275, 2016.

Alexandra AJ de Rotte, Wouter Koning, Martine TB Truijman, Anne G den Hartog, Sandra M Bovens, Aryan Vink, Shahrzad Sepehrkhouy, Jaco JM Zwanenburg, Dennis WJ Klomp, Gerard Pasterkamp,

et al. Seven-tesla magnetic resonance imaging of atherosclerotic plaque in the significantly stenosed carotid artery: a feasibility study. *Investigative radiology*, 49(11):749–757, 2014.

Pamela S Douglas, Udo Hoffmann, Manesh R Patel, Daniel B Mark, Hussein R Al-Khalidi, Brendan Cavanaugh, Jason Cole, Rowena J Dolor, Christopher B Fordyce, Megan Huang, et al. Outcomes of anatomical versus functional testing for coronary artery disease. *New England Journal of Medicine*, 372(14):1291–1300, 2015.

Vincent Dumoulin and Francesco Visin. A guide to convolution arithmetic for deep learning. *arXiv preprint arXiv:1603.07285*, 2016.

Marc R Dweck, Marcus WL Chow, Nikhil V Joshi, Michelle C Williams, Charlotte Jones, Alison M Fletcher, Hamish Richardson, Audrey White, Graham McKillop, Edwin JR van Beek, et al. Coronary arterial 18f-sodium fluoride uptake: a novel marker of plaque biology. *Journal of the American College of Cardiology*, 59(17):1539–1548, 2012.

Iryna Dykun, Nils Lehmann, Hagen Kälsch, Stefan Möhlenkamp, Susanne Moebus, Thomas Budde, Rainer Seibel, Dietrich Grönemeyer, Karl-Heinz Jöckel, Raimund Erbel, et al. Statin medication enhances progression of coronary artery calcification: the heinz nixdorf recall study. *Journal of the American College of Cardiology*, 68(19):2123–2125, 2016.

Bernd Ebner, Patrick Behm, Christoph Jacoby, Sandra Burghoff, Brent A French, Jürgen Schrader, and Ulrich Flögel. Early assessment of pulmonary inflammation by 19f mri in vivo. *Circulation: Cardiovascular Imaging*, 3(2):202–210, 2010.

Leticia Fernández-Friera, Valentin Fuster, Beatriz López-Melgar, Belen Oliva, Javier Sánchez-González, Angel Macias, Braulio Perez-Asenjo, Daniel Zamudio, Juan C Alonso-Farto, Samuel Espana, et al. Vascular inflammation in subclinical atherosclerosis detected by hybrid pet/mri. *Journal of the American College of Cardiology*, 73(12):1371–1382, 2019.

Michael C Fishbein and Robert J Siegel. How big are coronary atherosclerotic plaques that rupture? *Circulation*, 94(10):2662–2666, 1996.

Robert Fisher, Simon Perkins, Ashley Walker, and Eric Wolfart. *Hypermedia Image Processing Reference (HIPR)*. URL `https://homepages.inf.ed.ac.uk/rbf/HIPR2/hipr_top.htm`.
HIPR provides information on a wide range of image processing operations;
Image Calculation available at: https://homepages.inf.ed.ac.uk/rbf/HIPR2/pixadd.htm;
Contrast Enhancement available at: https://homepages.inf.ed.ac.uk/rbf/HIPR2/stretch.htm;
Thresholding available at: https://homepages.inf.ed.ac.uk/rbf/HIPR2/threshld.htm;
last accessed on January 6th, 2023.

Eckart Fleck, Markus Heinemann, Thomas Meinertz, Kurt Bestehorn, Ariane Pott, and Mirja Rohjans. *Herzbericht 2020*, 2020. URL `https://herzstiftung.de/system/files/2021-06/Deutscher-Herzbericht-2020.pdf`.
last accessed on January 6th, 2023.

U Flögel, S Su, I Kreideweiss, Z Ding, L Galbarz, J Fu, C Jacoby, O Witzke, and J Schrader. Noninvasive detection of graft rejection by in vivo 19f mri in the early stage. *American Journal of Transplantation*, 11(2):235–244, 2011.

Ulrich Flögel, Zhaoping Ding, Hendrik Hardung, Sebastian Jander, Gaby Reichmann, Christoph Jacoby, Rolf Schubert, and Jürgen Schrader. In vivo monitoring of inflammation after cardiac and cerebral ischemia by 19f magnetic resonance imaging. *Circulation*, 118(2):140, 2008.

Ulrich Flögel, Sebastian Temme, Christoph Jacoby, Thomas Oerther, Petra Keul, Vera Flocke, Xiaowei Wang, Florian Bönner, Fabian Nienhaus, Karlheinz Peter, Jürgen Schrader, Maria Grandoch, Malte Kelm, and Bodo Levkau. Multi-targeted 1h/19f mri unmasks specific danger patterns for emerging cardiovascular disorders. *Nature communications*, 12(1):1–12, 2021.

Nikolaos G Frangogiannis. Regulation of the inflammatory response in cardiac repair. *Circulation research*, 110(1):159–173, 2012.

Nikolaos G Frangogiannis, C Wayne Smith, and Mark L Entman. The inflammatory response in myocardial infarction. *Cardiovascular research*, 53(1):31–47, 2002.

Peter N Furness. The use of digital images in pathology. *The Journal of Pathology: A Journal of the Pathological Society of Great Britain and Ireland*, 183(3):253–263, 1997.

Juan F Granada, Krzysztof Milewski, Hugh Zhao, John J Stankus, Armando Tellez, Michael S Aboodi, Greg L Kaluza, Christian G Krueger, Renu Virmani, Lewis B Schwartz, et al. Vascular response to zotarolimus-coated balloons in injured superficial femoral arteries of the familial hypercholesterolemic swine. *Circulation: Cardiovascular Interventions*, 4(5):447–455, 2011.

Gary Gray, Eddie D Davenport, Dennis Bron, Rienk Rienks, Joanna dArcy, Norbert Guettler, Olivier Manen, Thomas Syburra, and Edward D Nicol. The challenge of asymptomatic coronary artery disease in aircrew; detecting plaque before the accident. *Heart*, 105(Suppl 1):s17–s24, 2019.

Philip Greenland, Robert O Bonow, Bruce H Brundage, Matthew J Budoff, Mark J Eisenberg, Scott M Grundy, Michael S Lauer, Wendy S Post, Paolo Raggi, Rita F Redberg, et al. Accf/aha 2007 clinical expert consensus document on coronary artery calcium scoring by computed tomography in global cardiovascular risk assessment and in evaluation of patients with chest pain: a report of the american college of cardiology foundation clinical expert consensus task force (accf/aha writing committee to update the 2000 expert consensus document on electron beam computed tomography) developed in collaboration with the society of atherosclerosis imaging and prevention and the society of cardiovascular computed tomography. *Journal of the American College of Cardiology*, 49(3):378–402, 2007.

Philip Greenland, Michael J Blaha, Matthew J Budoff, Raimund Erbel, and Karol E Watson. Coronary calcium score and cardiovascular risk. *Journal of the American College of Cardiology*, 72(4):434–447, 2018.

Kevin Gurney. *An introduction to neural networks*. CRC press, 2018.

Göran K Hansson, Peter Libby, Uwe Schönbeck, and Zhong-Qun Yan. Innate and adaptive immunity in the pathogenesis of atherosclerosis. *Circulation research*, 91(4):281–291, 2002.

Göran K Hansson, Anna-Karin L Robertson, and Cecilia Söderberg-Nauclér. Inflammation and atherosclerosis. *Annu. Rev. Pathol. Mech. Dis.*, 1:297–329, 2006.

Peter Haub and Tobias Meckel. A model based survey of colour deconvolution in diagnostic brightfield microscopy: Error estimation and spectral consideration. *Scientific reports*, 5:12096, 2015.

Willem E Hellings, Wouter Peeters, Frans L Moll, Sebastiaan RD Piers, Jessica van Setten, Peter J Van der Spek, Jean-Paul PM de Vries, Kees A Seldenrijk, Peter C De Bruin, Aryan Vink, et al. Composition of carotid atherosclerotic plaque is associated with cardiovascular outcome: a prognostic study. *Circulation*, 121(17):1941–1950, 2010.

Richard G Henderson. Nuclear magnetic resonance imaging: A review1. *Journal of the Royal Society of Medicine*, 76(3):206–212, 1983.

Chris Heyn, John A Ronald, Lisa T Mackenzie, Ian C MacDonald, Ann F Chambers, Brian K Rutt, and Paula J Foster. In vivo magnetic resonance imaging of single cells in mouse brain with optical validation. *Magnetic Resonance in Medicine: An Official Journal of the International Society for Magnetic Resonance in Medicine*, 55(1):23–29, 2006.

Florence Hofman. Immunohistochemistry. *Current protocols in immunology*, 49(1):21–4, 2002.

Satoki Homma, Dana A Troxclair, Arthur W Zieske, Gray T Malcom, Jack P Strong, Pathobiological Determinants of Atherosclerosis in Youth (PDAY) Research Group, et al. Histological topographical comparisons of atherosclerosis progression in juvenils and young adults. *Atherosclerosis*, 197(2):791–798, 2008.

Dominic PJ Howard, Van Lammeren Guus W, Peter M Rothwell, Jessica N Redgrave, Frans L Moll, Jean-Paul PM de Vries, Dominique PV De Kleijn, Hester M Den Ruijter, Gert Jan De Borst, and Gerard Pasterkamp. Symptomatic carotid atherosclerotic disease: correlations between plaque composition and ipsilateral stroke risk. *Stroke*, 46(1):182–189, 2015.

SPS Howarth, TY Tang, Rikin Trivedi, R Weerakkody, J U-King-Im, ME Gaunt, JR Boyle, ZY Li, SR Miller, MJ Graves, et al. Utility of uspio-enhanced mr imaging to identify inflammation and the fibrous cap: a comparison of symptomatic and asymptomatic individuals. *European journal of radiology*, 70(3):555–560, 2009.

Su-Ming Hsu, L Raine, and HX Fanger. Use of avidin-biotin-peroxidase complex (abc) in immunoperoxidase techniques: a comparison between abc and unlabeled antibody (pap) procedures. *Journal of Histochemistry & Cytochemistry*, 29(4):577–580, 1981.

Akira Ishii, F Vinuela, Y Murayama, I Yuki, YL Nien, DT Yeh, and HV Vinters. Swine model of carotid artery atherosclerosis: experimental induction by surgical partial ligation and dietary hypercholesterolemia. *American Journal of Neuroradiology*, 27(9):1893–1899, 2006.

Christoph Jacoby, Nadine Borg, Philipp Heusch, Martina Sauter, Florian Bönner, Reinhard Kandolf, Karin Klingel, Jürgen Schrader, and Ulrich Flögel. Visualization of immune cell infiltration in experimental viral myocarditis by 19 f mri in vivo. *Magnetic Resonance Materials in Physics, Biology and Medicine*, 27(1):101–106, 2014a.

Christoph Jacoby, Sebastian Temme, Friederike Mayenfels, Nicole Benoit, Marie Pierre Krafft, Rolf Schubert, Jürgen Schrader, and Ulrich Flögel. Probing different perfluorocarbons for in vivo inflammation imaging by 19f mri: image reconstruction, biological half-lives and sensitivity. *NMR in Biomedicine*, 27(3):261–271, 2014b.

Ik-Kyung Jang, Guillermo J Tearney, Briain MacNeill, Masamichi Takano, Fabian Moselewski, Nicusor Iftima, Milen Shishkov, Stuart Houser, H Thomas Aretz, Elkan F Halpern, et al. In vivo characterization of coronary atherosclerotic plaque by use of optical coherence tomography. *Circulation*, 111(12): 1551–1555, 2005.

Haibo Jia, Jiannan Dai, Jingbo Hou, Lei Xing, Lijia Ma, Huimin Liu, Maoen Xu, Yuan Yao, Sining Hu, Erika Yamamoto, et al. Effective anti-thrombotic therapy without stenting: intravascular optical coherence tomography-based management in plaque erosion (the erosion study). *European Heart Journal*, 38(11):792–800, 2017.

Amer M Johri, Vijay Nambi, Tasneem Z Naqvi, Steven B Feinstein, Esther SH Kim, Margaret M Park, Harald Becher, and Henrik Sillesen. Recommendations for the assessment of carotid arterial plaque by

ultrasound for the characterization of atherosclerosis and evaluation of cardiovascular risk: from the american society of echocardiography. *Journal of the American Society of Echocardiography*, 33(8): 917–933, 2020.

Nikhil V Joshi, Alex T Vesey, Michelle C Williams, Anoop SV Shah, Patrick A Calvert, Felicity HM Craighead, Su Ern Yeoh, William Wallace, Donald Salter, Alison M Fletcher, et al. 18f-fluoride positron emission tomography for identification of ruptured and high-risk coronary atherosclerotic plaques: a prospective clinical trial. *The Lancet*, 383(9918):705–713, 2014.

Dan J Kadrmas and John M Hoffman. Methodology for quantitative rapid multi-tracer pet tumor characterizations. *Theranostics*, 3(10):757, 2013.

Juhani Knuuti, William Wijns, Antti Saraste, Davide Capodanno, Emanuele Barbato, Christian Funck-Brentano, Eva Prescott, Robert F Storey, Christi Deaton, Thomas Cuisset, Stefan Agewall, Kenneth Dickstein, Thor Edvardsen, Javier Escaned, Bernard J Gersh, Pavel Svitil, Martine Gilard, David Hasdai, Robert Hatala, Felix Mahfoud, Josep Masip, Claudio Muneretto, Marco Valgimigli, Stephan Achenbach, Jeroen J Bax, and ESC Scientific Document Group. 2019 esc guidelines for the diagnosis and management of chronic coronary syndromes: The task force for the diagnosis and management of chronic coronary syndromes of the european society of cardiology (esc). *European Heart Journal*, 41 (3):407–477, 08 2019. ISSN 0195-668X. doi:10.1093/eurheartj/ehz425. URL `https://doi.org/10.1093/eurheartj/ehz425`.

Wolfgang Koenig and Natalie Khuseyinova. Biomarkers of atherosclerotic plaque instability and rupture. *Arteriosclerosis, thrombosis, and vascular biology*, 27(1):15–26, 2007.

Ran Kornowski, Mun K Hong, Fermin O Tio, Orville Bramwell, Hongsheng Wu, and Martin B Leon. In stent restenosis: contributions of inflammatory responses and arterial injury to neointimal hyperplasia. *Journal of the American College of Cardiology*, 31(1):224–230, 1998.

Kate Kosmac, Marta Gonzalez-Freire, Mary M McDermott, Sarah H White, R Grace Walton, Robert L Sufit, Lu Tian, Lingyu Li, Melina R Kibbe, Michael H Criqui, et al. Correlations of calf muscle macrophage content with muscle properties and walking performance in peripheral artery disease. *Journal of the American Heart Association*, 9(10):e015929, 2020.

Jason A Koutcher and C Tyler Burt. Principles of nuclear magnetic resonance. *Journal of nuclear medicine*, 25(1):101–111, 1984.

N Kume, MI Cybulsky, and MAi Gimbrone. Lysophosphatidylcholine, a component of atherogenic lipoproteins, induces mononuclear leukocyte adhesion molecules in cultured human and rabbit arterial endothelial cells. *The Journal of clinical investigation*, 90(3):1138–1144, 1992.

Marino Labinaz, Klaus Pels, Cyrla Hoffert, Sanjay Aggarwal, and Edward R O'Brien. Time course and importance of neoadventitial formation in arterial remodeling following balloon angioplasty of porcine coronary arteries. *Cardiovascular research*, 41(1):255–266, 1999.

Mark E Ladd. High-field-strength magnetic resonance: potential and limits. *Topics in Magnetic Resonance Imaging*, 18(2):139–152, 2007.

Gabriel Landini, Curtis Rueden, Johannes Schindelin, Mark Hiner, and Stefan Helfrich. *ImageJ Auto Threshold*. URL `https://imagej.net/Auto_Threshold`.
The Auto Threshold plugin is included in the Fiji distribution of ImageJ; references to the articles describing this plugin's methods for thresholding can be found at the URL above;
last accessed on January 6th, 2023.

Beatriz León, María López-Bravo, and Carlos Ardavín. Monocyte-derived dendritic cells. In *Seminars in immunology*, volume 17, pages 313–318. Elsevier, 2005.

Peter Libby. Inflammatory mechanisms: The molecular basis of inflammation and disease. *Nutrition reviews*, 65(suppl_3):S140–S146, 2007.

Peter Libby, Gerard Pasterkamp, Filippo Crea, and Ik-Kyung Jang. Reassessing the mechanisms of acute coronary syndromes: the vulnerable plaque and superficial erosion. *Circulation research*, 124(1): 150–160, 2019.

Wei Liu and Joseph A Frank. Detection and quantification of magnetically labeled cells by cellular mri. *European journal of radiology*, 70(2):258–264, 2009.

DB Longmore. The principles of magnetic resonance. *British medical bulletin*, 45(4):848–880, 1989.

Michael Mæng, Peter G Olesen, Niels C Emmertsen, Martin Thorwest, Torsten T Nielsen, Bent Ø Kristensen, Erling Falk, and Henning R Andersen. Time course of vascular remodeling, formation of neointima and formation of neoadventitia after angioplasty in a porcine model. *Coronary artery disease*, 12(4):285–293, 2001.

Ashley V Makela, Donna H Murrell, Katie M Parkins, Jenna Kara, Jeffrey M Gaudet, and Paula J Foster. Cellular imaging with mri. *Topics in Magnetic Resonance Imaging*, 25(5):177–186, 2016.

Henry B Mann and Donald R Whitney. On a test of whether one of two random variables is stochastically larger than the other. *The annals of mathematical statistics*, pages 50–60, 1947.

Joseph C McGowan. Basic principles of magnetic resonance imaging. *Neuroimaging Clinics of North America*, 18(4):623–636, 2008.

Mary L McHugh. The chi-square test of independence. *Biochemia medica*, 23(2):143–149, 2013.

Katie L McMahon, Gary Cowin, and Graham Galloway. Magnetic resonance imaging: the underlying principles. *journal of orthopaedic & sports physical therapy*, 41(11):806–819, 2011.

Ruslan Medzhitov. Inflammation 2010: New adventures of an old frame. *Cell*, 140:771–776, 2010. doi:10.1016/j.cell.2010.03.006. URL `https://doi.org/10.1016/j.cell.2010.03.006`.

Leon J Menezes, Carl W Kotze, Obi Agu, Toby Richards, Jocelyn Brookes, Vicky J Goh, Manuel Rodriguez-Justo, Raymondo Endozo, Richard Harvey, Syed W Yusuf, et al. Investigating vulnerable atheroma using combined 18f-fdg pet/ct angiography of carotid plaque with immunohistochemical validation. *Journal of Nuclear Medicine*, 52(11):1698–1703, 2011.

George A Mensah, Gina S Wei, Paul D Sorlie, Lawrence J Fine, Yves Rosenberg, Peter G Kaufmann, Michael E Mussolino, Lucy L Hsu, Ebyan Addou, Michael M Engelgau, et al. Decline in cardiovascular mortality: possible causes and implications. *Circulation research*, 120(2):366–380, 2017.

G Monizzi, J Sonck, S Nagumo, D Buytaert, L Van Hoe, L Grancini, AL Bartorelli, P Vanhoenacker, P Simons, O Bladt, et al. Quantification of calcium burden by coronary ct angiography compared to optical coherence tomography. *The International Journal of Cardiovascular Imaging*, 36(12):2393–2402, 2020.

Francesco Moroni, Enrico Ammirati, Giuseppe Danilo Norata, Marco Magnoni, and Paolo G Camici. The role of monocytes and macrophages in human atherosclerosis, plaque neoangiogenesis, and atherothrombosis. *Mediators of inflammation*, 2019, 2019.

Jan Nagenborg, Pieter Goossens, Erik AL Biessen, and Marjo MPC Donners. Heterogeneity of atherosclerotic plaque macrophage origin, phenotype and functions: implications for treatment. *European journal of pharmacology*, 816:14–24, 2017.

Morteza Naghavi, Peter Libby, Erling Falk, S Ward Casscells, Silvio Litovsky, John Rumberger, Juan Jose Badimon, Christodoulos Stefanadis, Pedro Moreno, Gerard Pasterkamp, et al. From vulnerable plaque to vulnerable patient: a call for new definitions and risk assessment strategies: Part i. *Circulation*, 108 (14):1664–1672, 2003.

Yutaka Nakashima, Elaine W Raines, Andrew S Plump, Jan L Breslow, and Russell Ross. Upregulation of vcam-1 and icam-1 at atherosclerosis-prone sites on the endothelium in the apoe-deficient mouse. *Arteriosclerosis, thrombosis, and vascular biology*, 18(5):842–851, 1998.

Carl Nathan. Neutrophils and immunity: challenges and oppurtunities. *Nature review immunology*, 6(3): 173–182, 2006.

Fabian Nienhaus, Denise Colley, Annika Jahn, Susanne Pfeiler, Vera Flocke, Sebastian Temme, Malte Kelm, Norbert Gerdes, Ulrich Flögel, and Florian Bönner. Phagocytosis of a pfob-nanoemulsion for 19f magnetic resonance imaging: First results in monocytes of patients with stable coronary artery disease and st-elevation myocardial infarction. *Molecules*, 24(11):2058, 2019.

Sussan Nourshargh and Ronen Alon. Leukocyte migration into inflamed tissues. *Immunity*, 41(5):694–707, 2014.

Kisho Ohtani, Kensuke Egashira, Ken-ichi Hiasa, Qingwei Zhao, Shiro Kitamoto, Minako Ishibashi, Makoto Usui, Shujiro Inoue, Yoshikazu Yonemitsu, Katsuo Sueishi, et al. Blockade of vascular endothelial growth factor suppresses experimental restenosis after intraluminal injury by inhibiting recruitment of monocyte lineage cells. *Circulation*, 110(16):2444–2452, 2004.

Evangelos K Oikonomou, Mohamed Marwan, Milind Y Desai, Jennifer Mancio, Alaa Alashi, Erika Hutt Centeno, Sheena Thomas, Laura Herdman, Christos P Kotanidis, Katharine E Thomas, et al. Non-invasive detection of coronary inflammation using computed tomography and prediction of residual cardiovascular risk (the crisp ct study): a post-hoc analysis of prospective outcome data. *The Lancet*, 392(10151):929–939, 2018.

Evangelos K Oikonomou, Milind Y Desai, Mohamed Marwan, Christos P Kotanidis, Alexios S Antonopoulos, David Schottlander, Keith M Channon, Stefan Neubauer, Stephan Achenbach, and Charalambos Antoniades. Perivascular fat attenuation index stratifies cardiac risk associated with high-risk plaques in the crisp-ct study. *Journal of the American College of Cardiology*, 76(6):755–757, 2020.

Ei-ichi Okamoto, Tracey Couse, Hector De Leon, Jakob Vinten-Johansen, Richard B Goodman, Neal A Scott, and Josiah N Wilcox. Perivascular inflammation after balloon angioplasty of porcine coronary arteries. *Circulation*, 104(18):2228–2235, 2001.

Daniel S Ong, Jay S Lee, Tsunenari Soeda, Takumi Higuma, Yoshiyasu Minami, Zhao Wang, Hang Lee, Hiroaki Yokoyama, Takashi Yokota, Ken Okumura, et al. Coronary calcification and plaque vulnerability: an optical coherence tomographic study. *Circulation: Cardiovascular Imaging*, 9(1): e003929, 2016.

Fumiyuki Otsuka, Robert A Byrne, Kazuyuki Yahagi, Hiroyoshi Mori, Elena Ladich, David R Fowler, Robert Kutys, Erion Xhepa, Adnan Kastrati, Renu Virmani, et al. Neoatherosclerosis: overview of histopathologic findings and implications for intravascular imaging assessment. *European heart journal*, 36(32):2147–2159, 2015.

Ramon A Partida, Peter Libby, Filippo Crea, and Ik-Kyung Jang. Plaque erosion: a new in vivo diagnosis and a potential major shift in the management of patients with acute coronary syndromes. *European heart journal*, 39(22):2070–2076, 2018.

Bernward Passlick, Dimitri Flieger, and HW Ziegler-Heitbrock. Identification and characterization of a novel monocyte subpopulation in human peripheral blood. *Blood, The Journal of the American Society of Hematology*, 74(7):2527–2535, 1989.

Adam Paszke, Sam Gross, Soumith Chintala, Gregory Chanan, Edward Yang, Zachary DeVito, Zeming Lin, Alban Desmaison, Luca Antiga, and Adam Lerer. Automatic differentiation in pytorch. 2017.

Klaus Pels, Marino Labinaz, Cyrla Hoffert, and Edward R OBrien. Adventitial angiogenesis early after coronary angioplasty: correlation with arterial remodeling. *Arteriosclerosis, thrombosis, and vascular biology*, 19(2):229–238, 1999.

Sumanth D Prabhu and Nikolaos G Frangogiannis. The biological basis for cardiac repair after myocardial infarction: from inflammation to fibrosis. *Circulation research*, 119(1):91–112, 2016.

Thibaut Quillard, Grégory Franck, Thomas Mawson, Eduardo Folco, and Peter Libby. Mechanisms of erosion of atherosclerotic plaques. *Current opinion in lipidology*, 28(5):434, 2017.

Zoya Rabkin, Ora Israel, and Zohar Keidar. Do hyperglycemia and diabetes affect the incidence of false-negative 18f-fdg pet/ct studies in patients evaluated for infection or inflammation and cancer? a comparative analysis. *Journal of Nuclear Medicine*, 51(7):1015–1020, 2010.

Kristiina Rajamäki, Jani Lappalainen, Katariina Öörni, Elina Välimäki, Sampsa Matikainen, Petri T Kovanen, and Kari K Eklund. Cholesterol crystals activate the nlrp3 inflammasome in human macrophages: a novel link between cholesterol metabolism and inflammation. *PloS one*, 5(7):e11765, 2010.

Anthony E Rizzardi, Arthur T Johnson, Rachel Isaksson Vogel, Stefan E Pambuccian, Jonathan Henriksen, Amy PN Skubitz, Gregory J Metzger, and Stephen C Schmechel. Quantitative comparison of immunohistochemical staining measured by digital image analysis versus pathologist visual scoring. *Diagnostic pathology*, 7(1):1–10, 2012.

Clinton S Robbins, Ingo Hilgendorf, Georg F Weber, Igor Theurl, Yoshiko Iwamoto, Jose-Luiz Figueiredo, Rostic Gorbatov, Galina K Sukhova, Louisa Gerhardt, David Smyth, et al. Local proliferation dominates lesional macrophage accumulation in atherosclerosis. *Nature medicine*, 19(9):1166–1172, 2013.

Kenneth L Rock, Eicke Latz, Fernando Ontiveros, and Hajime Kono. The sterile inflammatory response. *Annual review of immunology*, 28:321–342, 2009.

Kyrill S Rogacev, Bodo Cremers, Adam M Zawada, Sarah Seiler, Nadine Binder, Philipp Ege, Gunnar Große-Dunker, Isabel Heisel, Florian Hornof, Jana Jeken, et al. Cd14++ cd16+ monocytes independently predict cardiovascular events: a cohort study of 951 patients referred for elective coronary angiography. *Journal of the American College of Cardiology*, 60(16):1512–1520, 2012.

Ian S Rogers, Khurram Nasir, Amparo L Figueroa, Ricardo C Cury, Udo Hoffmann, David A Vermylen, Thomas J Brady, and Ahmed Tawakol. Feasibility of fdg imaging of the coronary arteries: comparison between acute coronary syndrome and stable angina. *JACC: Cardiovascular Imaging*, 3(4):388–397, 2010.

Olaf Ronneberg, Philipp Fischer, and Thomas Brox. U-net: Convolutional networks for biomedical image segmentation. In *International Conference on Medical image computing and computer-assisted intervention*, pages 234–241. Springer, 2015.

Russell Ross. Atherosclerosisan inflammatory disease. *New England journal of medicine*, 340(2):115–126, 1999.

Maik Rothe, Annika Jahn, Kilian Weiss, Jong-Hee Hwang, Julia Szendroedi, Malte Kelm, Jürgen Schrader, Michael Roden, Ulrich Flögel, and Florian Bönner. In vivo 19f mr inflammation imaging after myocardial infarction in a large animal model at 3 t. *Magnetic Resonance Materials in Physics, Biology and Medicine*, 32(1):5–13, 2019.

Henning Rud Andersen, Michael Mæng, Martin Thorwest, and Erling Falk. Remodeling rather than neointimal formation explains luminal narrowing after deep vessel wall injury: insights from a porcine coronary (re) stenosis model. *Circulation*, 93(9):1716–1724, 1996.

Arnout C Ruifrok, Dennis A Johnston, et al. Quantification of histochemical staining by color deconvolution. *Analytical and quantitative cytology and histology*, 23(4):291–299, 2001.

Chang-Woo Ryu, Hyo-Sung Kwak, Geon-Ho Jahng, and Han Na Lee. High-resolution mri of intracranial atherosclerotic disease. *Neurointervention*, 9(1):9, 2014.

Martin Schillinger and Erich Minar. Restenosis after percutaneous angioplasty: the role of vascular inflammation. *Vascular health and risk management*, 1(1):73, 2005.

Johannes Schindelin, Ignacio Arganda-Carreras, Erwin Frise, Verena Kaynig, Mark Longair, Tobias Pietzsch, Stephan Preibisch, Curtis Rueden, Stephan Saalfeld, Benjamin Schmid, et al. Fiji: an open-source platform for biological-image analysis. *Nature methods*, 9(7):676–682, 2012.

Caroline A Schneider, Wayne S Rasband, and Kevin W Eliceiri. Nih image to imagej: 25 years of image analysis. *Nature methods*, 9(7):671, 2012.

Vincent PW Scholtes, Jason L Johnson, Nicholas Jenkins, Graciela B Sala-Newby, Jean-Paul PM de Vries, Gert Jan de Borst, Dominique PV de Kleijn, Frans L Moll, Gerard Pasterkamp, and Andrew C Newby. Carotid atherosclerotic plaque matrix metalloproteinase-12–positive macrophage subpopulation predicts adverse outcome after endarterectomy. *Journal of the American Heart Association*, 1(6):e001040, 2012.

Kate Schroder and Jurg Tschopp. The inflammasomes. *cell*, 140(6):821–832, 2010.

Neal A Scott, Gustavo D Cipolla, Cheryl E Ross, Bradley Dunn, Francis H Martin, Lizette Simonet, and Josiah N Wilcox. Identification of a potential role for the adventitia in vascular lesion formation after balloon overstretch injury of porcine coronary arteries. *Circulation*, 93(12):2178–2187, 1996.

Junhee Seok, H Shaw Warren, Alex G Cuenca, Michael N Mindrinos, Henry V Baker, Weihong Xu, Daniel R Richards, Grace P McDonald-Smith, Hong Gao, Laura Hennessy, et al. Genomic responses in mouse models poorly mimic human inflammatory diseases. *Proceedings of the National Academy of Sciences*, 110(9):3507–3512, 2013.

Carlos V Serrano, José Antônio F Ramires, Margareth Venturinelli, Siguemituso Arie, Elbio DAmico, Jay L Zweier, Fulvio Pileggi, and Protasio L Da Luz. Coronary angioplasty results in leukocyte and platelet activation with adhesion molecule expression: evidence of inflammatory responses in coronary angioplasty. *Journal of the American College of Cardiology*, 29(6):1276–1283, 1997.

Patrick W Serruys, David P Foley, Richard L Kirkeeide, and Spencer B King III. Restenosis revisited: insights provided by quantitative coronary angiography. *American heart journal*, 126(5):1243–1267, 1993.

Erik M Shapiro, Laura N Medford-Davis, Tarek M Fahmy, Cynthia E Dunbar, and Alan P Koretsky. Antibody-mediated cell labeling of peripheral t cells with micron-sized iron oxide particles (mpios) allows single cell detection by mri. *Contrast media & molecular imaging*, 2(3):147–153, 2007.

Xuan Shi, Jie Gao, Quishi Lv, Haodi Cai, Fang Wang, Ruidong Ye, and Xinfeng Liu. Calcification in atherosclerotic plaque vulnerability: friend or foe? *Frontiers in physiology*, 11:56, 2020.

Yi Shi, Marc Pieniek, Ali Fard, James OBrien, John D Mannion, and Andrew Zalewski. Adventitial remodeling after coronary arterial injury. *Circulation*, 93(2):340–348, 1996.

Evan Shlofmitz, Micaela Iantorno, and Ron Waksman. Restenosis of drug-eluting stents: a new classification system based on disease mechanism to guide treatment and state-of-the-art review. *Circulation: Cardiovascular Interventions*, 12(8):e007023, 2019.

Kristina Skålén, Maria Gustafsson, Ellen Knutsen Rydberg, Lillemor Mattsson Hultén, Olov Wiklund, Thomas L Innerarity, and Jan Borén. Subendothelial retention of atherogenic lipoproteins in early atherosclerosis. *Nature*, 417(6890):750, 2002.

Joanna Skrzeczyńska-Moncznik, Małgorzata Bzowska, S Lo seke, E Grage-Griebenow, M Zembala, and J Pryjma. Peripheral blood cd14high cd16+ monocytes are main producers of il-10. *Scandinavian journal of immunology*, 67(2):152–159, 2008.

Donat R Spahn, Klaus F Waschke, Thomas Standl, Johann Motsch, Léone Van Huynegem, Martin Welte, Hans Gombotz, Pierre Coriat, Lev Verkh, Simon Faithfull, et al. Use of perflubron emulsion to decrease allogeneic blood transfusion in high-blood-loss non-cardiac surgeryresults of a european phase 3 study. *Anesthesiology: The Journal of the American Society of Anesthesiologists*, 97(6):1338–1349, 2002.

DonatR Spahn. Blood substitutes artificial oxygen carriers: perfluorocarbon emulsions. *Critical Care*, 3 (5):R93, 1999.

Statistisches Bundesamt. *Operationen und Prozeduren 2018*, 2018. URL `https://destatis.de/DE/Themen/Gesellschaft-Umwelt/Gesundheit/Krankenhaeuser/Publikationen/Downloads-Krankenhaeuser/operationen-prozeduren-5231401187014.pdf?__blob=publicationFile`.
last accessed on January 6th, 2023.

Cyril Štěchovskỳ, Petr Hájek, Martin Horváth, Miloslav Špaček, and Josef Veselka. Near-infrared spectroscopy combined with intravascular ultrasound in carotid arteries. *The international journal of cardiovascular imaging*, 32(1):181–188, 2016.

Eli Stevens, Luca Antiga, and Thomas Viehmann. *Deep learning with PyTorch*. Manning Publications, 2020.

Jack Stewart, Gavin Manmathan, and Peter Wilkinson. Primary prevention of cardiovascular disease: A review of contemporary guidance and literature. *JRSM cardiovascular disease*, 6:2048004016687211, 2017.

Gregg W Stone, Akiko Maehara, Alexandra J Lansky, Bernard De Bruyne, Ecaterina Cristea, Gary S Mintz, Roxana Mehran, John McPherson, Naim Farhat, Steven P Marso, et al. A prospective natural-history study of coronary atherosclerosis. *New England journal of medicine*, 364(3):226–235, 2011.

Jack P Strong, Gray T Malcom, C Alex McMahan, Richard E Tracy, William P Newman III, Edward E Herderick, J Fredrick Cornhill, Pathobiological Determinants of Atherosclerosis in Youth Research Group, et al. Prevalence and extent of atherosclerosis in adolescents and young adults: implications for prevention from the pathobiological determinants of atherosclerosis in youth study. *Jama*, 281(8):727–735, 1999.

Michelle A Sugimoto, Lirlândia P Sousa, Vanessa Pinho, Mauro Perretti, and Mauro M Teixeira. Resolution of inflammation: what controls its onset? *Frontiers in immunology*, 7:160, 2016.

Filip K Swirski, Peter Libby, Elena Aikawa, Pilar Alcaide, F William Luscinskas, Ralph Weissleder, Mikael J Pittet, et al. Ly-6c hi monocytes dominate hypercholesterolemia-associated monocytosis and give rise to macrophages in atheromata. *The Journal of clinical investigation*, 117(1):195–205, 2007.

Maaz BJ Syed, Alexander J Fletcher, Rachael O Forsythe, Jakub Kaczynski, David E Newby, Marc R Dweck, and Edwin JR van Beek. Emerging techniques in atherosclerosis imaging. *The British Journal of Radiology*, 92(1103):20180309, 2019.

Richard P Tan, Isabelle Ryder, Nianji Yang, Yuen Ting Lam, Miguel Santos, Praveesuda L Michael, David A Robinson, Martin K Ng, and Steven G Wise. Macrophage polarization as a novel therapeutic target for endovascular intervention in peripheral artery disease. *Basic to Translational Science*, 6(8): 693–704, 2021.

Jason M Tarkin, Marc R Dweck, Nicholas R Evans, Richard AP Takx, Adam J Brown, Ahmed Tawakol, Zahi A Fayad, and James HF Rudd. Imaging atherosclerosis. *Circulation research*, 118(4):750–769, 2016.

Jason M Tarkin, Francis R Joshi, Nicholas R Evans, Mohammed M Chowdhury, Nichola L Figg, Aarti V Shah, Lakshi T Starks, Abel Martin-Garrido, Roido Manavaki, Emma Yu, et al. Detection of atherosclerotic inflammation by 68ga-dotatate pet compared to [18f] fdg pet imaging. *Journal of the American College of Cardiology*, 69(14):1774–1791, 2017.

Guillermo J Tearney, Hiroshi Yabushita, Stuart L Houser, H Thomas Aretz, Ik-Kyung Jang, Kelly H Schlendorf, Christopher R Kauffman, Milen Shishkov, Elkan F Halpern, and Brett E Bouma. Quantification of macrophage content in atherosclerotic plaques by optical coherence tomography. *Circulation*, 107(1):113–119, 2003.

Sebastian Temme, Christoph Grapentin, Christine Quast, Christoph Jacoby, Maria Grandoch, Zhaoping Ding, Christoph Owenier, Friederike Mayenfels, Jens W Fisher, Rolf Schubert, et al. Noninvasive imaging of early venous thrombosis by 19f magnetic resonance imaging with targeted perfluorocarbon nanoemulsions. *Circulation*, 131(16):1405–1414, 2015.

Philippe Thévenaz and Michael Unser. User-friendly semiautomated assembly of accurate image mosaics in microscopy. *Microscopy research and technique*, 70(2):135–146, 2007.

Lale Tokgözoğlu and Peter Libby. The dawn of a new era of targeted lipid-lowering therapies. *European Heart Journal*, 2022.

Mariusz Tomaniak, Yuki Katagiri, Rodrigo Modolo, Ranil de Silva, Ramzi Y Khamis, Christos V Bourantas, Ryo Torii, Jolanda J Wentzel, Frank JH Gijsen, Gijs van Soest, et al. Vulnerable plaques and patients: state-of-the-art. *European heart journal*, 41(31):2997–3004, 2020.

Nick Townsend, Lauren Wilson, Prachi Bhatnagar, Kremlin Wickramasinghe, Mike Rayner, and Melanie Nichols. Cardiovascular disease in europe: epidemiological update 2016. *European heart journal*, 37 (42):3232–3245, 2016.

Rikin A Trivedi, Chinthake Mallawarachi, Jean-Marie U-King-Im, Martin J Graves, Jo Horsley, Martin J Goddard, Andrew Brown, Liqun Wang, Peter J Kirkpatrick, John Brown, et al. Identifying inflamed carotid plaques using in vivo uspio-enhanced mr imaging to label plaque macrophages. *Arteriosclerosis, thrombosis, and vascular biology*, 26(7):1601–1606, 2006.

Dimitrios A Tsakiris, Martin Tschöpl, Kurt Jäger, Walter E Haefeli, Francine Wolf, and German A Marbet. Circulating cell adhesion molecules and endothelial markers before and after transluminal angioplasty in peripheral arterial occlusive disease. *Atherosclerosis*, 142(1):193–200, 1999.

Jeroen AWM Van der Laak, Martin MM Pahlplatz, Antonius GJM Hanselaar, and Peter CM de Wilde. Hue-saturation-density (hsd) model for stain recognition in digital images from transmitted light microscopy. *Cytometry: The Journal of the International Society for Analytical Cytology*, 39(4):275–284, 2000.

Rogier A van Dijk, Kevin Rijs, Anouk Wezel, Jaap F Hamming, Frank D Kolodgie, Renu Virmani, Alexander F Schaapherder, and Jan HN Lindeman. Systematic evaluation of the cellular innate immune response during the process of human atherosclerosis. *Journal of the American Heart Association*, 5 (6):e002860, 2016.

Robert-Jan M Van Geuns, Piotr A Wielopolski, Hein G de Bruin, Benno J Rensing, Peter MA van Ooijen, Marc Hulshoff, Matthijs Oudkerk, and Pim J de Feyter. Basic principles of magnetic resonance imaging. *Progress in cardiovascular diseases*, 42(2):149–156, 1999.

Ruud B Van Heeswijk, Maxime Pellegrin, Ulrich Flögel, Christine Gonzales, Jean-François Aubert, Lucia Mazzolai, Juerg Schwitter, and Matthias Stuber. Fluorine mr imaging of inflammation in atherosclerotic plaque in vivo. *Radiology*, 275(2):421–429, 2015.

Renu Virmani, Frank D Kolodgie, Allen P Burke, Aloke V Finn, Herman K Gold, Thomas N Tulenko, Steven P Wrenn, and Jagat Narula. Atherosclerotic plaque progression and vulnerability to rupture: angiogenesis as a source of intraplaque hemorrhage. *Arteriosclerosis, thrombosis, and vascular biology*, 25(10):2054–2061, 2005.

Renu Virmani, Allen P Burke, Andrew Farb, and Frank D Kolodgie. Pathology of the vulnerable plaque. *Journal of the American College of Cardiology*, 47(8 Supplement):C13–C18, 2006a.

Renu Virmani, Elena R Ladich, Allen P Burke, and Frank D Kolodgie. Histopathology of carotid atherosclerotic disease. *Neurosurgery*, 59(suppl_5):S3–219, 2006b.

Pauli Virtanen, Ralf Gommers, Travis E Oliphant, Matt Haberland, Tyler Reddy, David Cournapeau, Evegeni Burovski, Pearu Peterson, Warren Weckesser, Jonathan Bright, Stéfan J van der Walt, Matthew Brett, Joshua Wilson, K Jarrod Millman, Nikolay Mayorov, Andrew R J Nelson, Eric Jones, Robert Kern, Eric Larson, C J Carey, İlhan Polat, Yu Feng, Eric W Moore, Jake VanderPlas, Denis Laxalde, Josef Perktold, Robert Cimrman, Ian Henriksen, E A Quintero, Charles R Harris, Anne M Archibald, Antônio H Ribeiro, Fabian Pedregosa, Paul van Mulbregt, and SciPy 1.0 Contributors. SciPy 1.0: Fundamental Algorithms for Scientific Computing in Python. *Nature Methods*, 17:261–272, 2020. doi:10.1038/s41592-019-0686-2. URL `https://rdcu.be/b08Wh`.

Xiaowei Wang, Sebastian Temme, Christoph Grapentin, Jathushan Palasubramaniam, Aidan Walsh, Wolfgang Krämer, Patricia Kleimann, Asli Havlas, Rolf Schubert, Jürgen Schrader, et al. Fluorine-19 magnetic resonance imaging of activated platelets. *Journal of the American Heart Association*, 9(18): e016971, 2020.

H Shaw Warren, Catherine Fitting, Eva Hoff, Minou Adib-Conquy, Laura Beasley-Topliffe, Brenda Tesini, Xueya Liang, Catherine Valentine, Judith Hellman, Douglas Hayden, et al. Resilience to bacterial infection: difference between species could be due to proteins in serum. *The Journal of infectious diseases*, 201(2):223–232, 2010.

Sergio Waxman, Fumiyuki Ishibashi, and James E Muller. Detection and treatment of vulnerable plaques and vulnerable patients: novel approaches to prevention of coronary events. *Circulation*, 114(22):2390–2411, 2006.

Bryant J Webber, Peter G Seguin, Daniel G Burnett, Leslie L Clark, and Jean L Otto. Prevalence of and risk factors for autopsy-determined atherosclerosis among us service members, 2001-2011. *Jama*, 308(24):2577–2583, 2012.

Wolfgang Weninger, Maté Biro, and Rohit Jain. Leukocyte migration in the interstitial space of non-lymphoid organs. *Nature Reviews Immunology*, 14(4):232, 2014.

Elizabeth Wilkins, L Wilson, Kremlin Wickramasinghe, Prachi Bhatnagar, Jose Leal, Ramon Luengo-Fernandez, R Burns, Mike Rayner, and Nick Townsend. European cardiovascular disease statistics 2017. 2017. URL `http://www.ehnheart.org/images/CVD-statistics-report-August-2017.pdf`. last accessed on January 6th, 2023.

EM Winter, B Hogers, LM Van der Graaf, AC Gittenberger-de Groot, RE Poelmann, and L Van der Weerd. Cell tracking using iron oxide fails to distinguish dead from living transplanted cells in the infarcted heart. *Magnetic resonance in medicine*, 63:817–821, 2010.

Joseph L Witztum and Andrew H Lichtman. The influence of innate and adaptive immune responses on atherosclerosis. *Annual Review of Pathology: Mechanisms of Disease*, 9: 73–102, 2014. doi:10.1146/annurev-pathol-020712-163936. URL `https://doi.org/10.1146/annurev-pathol-020712-163936`. PMID: 23937439.

Joseph L Witztum and Daniel Steinberg. Role of oxidized low density lipoprotein in atherogenesis. *The Journal of clinical investigation*, 88(6):1785–1792, 1991.

Kok Loon Wong, June Jing-Yi Tai, Wing-Cheong Wong, Hao Han, Xiaohui Sem, Wei-Hseun Yeap, Philippe Kourilsky, and Siew-Cheng Wong. Gene expression profiling reveals the defining features of the classical, intermediate, and nonclassical human monocyte subsets. *Blood, The Journal of the American Society of Hematology*, 118(5):e16–e31, 2011.

Rob CI Wüst, Claudia Calcagno, Mariah RR Daal, Aart J Nederveen, Bram F Coolen, and Gustav J Strijkers. Emerging magnetic resonance imaging techniques for atherosclerosis imaging: High magnetic field, relaxation time mapping, and fluorine-19 imaging. *Arteriosclerosis, thrombosis, and vascular biology*, 39(5):841–849, 2019.

Joanna Wykrzykowska, Sanaz Lehman, Gethin Williams, J Anthony Parker, Matthew R Palmer, Santosh Varkey, Gerald Kolodny, and Roger Laham. Imaging of inflamed and vulnerable plaque in coronary arteries with 18f-fdg pet/ct in patients with suppression of myocardial uptake using a low-carbohydrate, high-fat preparation. *Journal of nuclear medicine*, 50(4):563–568, 2009.

Haoxing Xu and Dejian Ren. Lysosomal physiology. *Annual review of physiology*, 77:57, 2015.

Motoko Yamada, Shokei Kim, Kensuke Egashira, Motohiro Takeya, Tomohiro Ikeda, Osamu Mimura, and Hiroshi Iwao. Molecular mechanism and role of endothelial monocyte chemoattractant protein-1 induction by vascular endothelial growth factor. *Arteriosclerosis, thrombosis, and vascular biology*, 23 (11):1996–2001, 2003.

Hiroyuki Yamamoto, Naofumi Yoshida, Toshiro Shinke, Hiromasa Otake, Masaru Kuroda, Kazuhiko Sakaguchi, Yushi Hirota, Takayoshi Toba, Hachidai Takahashi, Daisuke Terashita, et al. Impact of cd14++ cd16+ monocytes on coronary plaque vulnerability assessed by optical coherence tomography in coronary artery disease patients. *Atherosclerosis*, 269:245–251, 2018.

Ali Yilmaz, Sabine Rösch, Karin Klingel, Reinhard Kandolf, Xavier Helluy, Karl-Heinz Hiller, Peter M Jakob, and Udo Sechtem. Magnetic resonance imaging (mri) of inflamed myocardium using iron oxide nanoparticles in patients with acute myocardial infarctionpreliminary results. *International journal of cardiology*, 163(2):175–182, 2013.

Izma Zani, Sam Stephen, Nadeem Mughal, David Russell, Shervanthi Homer-Vanniasinkam, Stephen Wheatcroft, and Sreenivasan Ponnambalam. Scavenger receptor structure and function in health and disease. *Cells*, 4(2):178–201, 2015.

Niloufar Zarghami, Alexandre A Khrapitchev, Francisco Perez-Balderas, Manuel Sarmiento Soto, James R Larkin, Luca Bau, and Nicola R Sibson. Optimization of molecularly targeted mri in the brain: empirical comparison of sequences and particles. *International journal of nanomedicine*, 13: 4345, 2018.

Huiying Zhang, Lei Zhang, Jacob Myerson, Kristin Bibee, Michael Scott, John Allen, Gregorio Sicard, Gregory Lanza, and Samuel Wickline. Quantifying the evolution of vascular barrier disruption in advanced atherosclerosis with semipermeant nanoparticle contrast agents. *PloS one*, 6(10):e26385, 2011.

Huaien Zheng, Karina Gasbarrino, John P Veinot, Chi Lai, and Stella S Daskalopoulou. New quantitative digital image analysis method of histological features of carotid atherosclerotic plaques. *European Journal of Vascular and Endovascular Surgery*, 58(5):654–663, 2019.

Loems Ziegler-Heitbrock, Petronela Ancuta, Suzanne Crowe, Marc Dalod, Veronika Grau, Derek N Hart, Pieter JM Leenen, Yong-Jun Liu, Gordon MacPherson, Gwendalyn J Randolph, et al. Nomenclature of monocytes and dendritic cells in blood. *Blood, The Journal of the American Society of Hematology*, 116(16):e74–e80, 2010.

6 Appendix

6.1 *Unet* Image Segmentation

The Unet model described in Section 2.2.3 was implemented using PyTorch as shown below.

```
import torch
import torch.nn as nn
import torchvision.transforms.functional as tf

class double_convolution(nn.Module):
    def __init__(self, in_channels, out_channels):
        super().__init__()
        self.convolution = []
        for c in (in_channels, out_channels):
            self.convolution.append(nn.Conv2d(c, out_channels, kernel_size = 3,\
                                              stride = 1, padding = 0, bias = False))
            self.convolution.append(nn.BatchNorm2d(out_channels))
            self.convolution.append(nn.ReLU(inplace = True))
        self.convolution = nn.Sequential(*self.convolution)
    def forward(self, input_batch):
        return self.convolution(input_batch)

class unet(nn.Module):
    def __init__(self, in_channels = 3, out_channels = 1, features = [64, 128, 256, 512]):
        super().__init__()
        self.contracting_path, self.expanding_path = nn.ModuleList(), nn.ModuleList()
        self.max_pool = nn.MaxPool2d(kernel_size = 2, stride = 2)
        for feature in features:
            self.contracting_path.append(double_convolution(in_channels, feature))
            in_channels = feature
        for feature in reversed(features):
            temp = nn.ModuleList()
            ct2d = nn.ConvTranspose2d(feature * 2, feature, kernel_size = 2, stride = 2)
            temp.append(ct2d)
            temp.append(double_convolution(feature * 2, feature))
            self.expanding_path.append(temp)
        self.final_expansion = double_convolution(features[-1], features[-1] * 2)
        self.final_contraction = nn.Conv2d(features[0], out_channels, kernel_size = 1)
    def forward(self, input_batch):
        skip_connections, input_shape = [], input_batch.shape[2 :]
        for contraction in self.contracting_path:
            input_batch = contraction(input_batch)
            skip_connections.append(input_batch)
            input_batch = self.max_pool(input_batch)
        input_batch = self.final_expansion(input_batch)
        for ep, sc in zip(self.expanding_path, reversed(skip_connections)):
            input_batch = ep[0](input_batch)
            if input_batch.shape != sc.shape:
                #sc = tf.resize(sc, size = input_batch.shape[2 :])
                input_batch = tf.resize(input_batch, size = sc.shape[2 :])
            input_batch = torch.cat((sc, input_batch), dim = 1)
```

```
            input_batch = ep[1](input_batch)
        input_batch = self.final_contraction(input_batch)
        return tf.resize(input_batch, size = input_shape)
```

Before starting the training process, image preprocessing was performed. This involved splitting up the images into subparts of the same size whose number of rows and colums were close to 500. Thereafter, white padding was added around the subparts such that the number of rows and columns equaled 500. Then, to increase the amount of data prior to training the network, the subparts were randomly flipped horizontally, flipped vertically, and rotated randomly. Additionally, hue, saturation, and contrast were randomly altered. The split-up original images and their random mutations were saved. For training purposes, four epochs were run with the Adam-optimizer included with PyTorch, BCEWithLogitsLoss-Loss function included with PyTorch, a batch size of 8, and a learning rate of 0.01. The python code used for training the network is given below.

```
from tqdm import tqdm
import os
import torch
import torch.nn as nn
import torch.optim as optim
from torchvision.transforms import Normalize
from torchvision.transforms.functional import hflip, vflip, rotate
from unet import unet
from utils import data_loader, save_predictions, save_checkpoint, load_checkpoint

def train_network(loader, model, optimizer, loss_function, scaler, device):
    loop = tqdm(loader)
    for batch_index, (data, targets) in enumerate(loop):
        data = data.to(device = device)
        targets = targets.float().unsqueeze(1).to(device = device)
        with torch.cuda.amp.autocast():
            predictions = model(data)
            loss = loss_function(predictions, targets)
        optimizer.zero_grad()
        scaler.scale(loss).backward()
        scaler.step(optimizer)
        scaler.update()
        loop.set_postfix(loss = loss.item())

def main(path, load = None):
    device = 'cuda' if torch.cuda.is_available() else 'cpu'
    model = unet(in_channels = 3, out_channels = 1).to(device = device)
    loss_function = nn.BCEWithLogitsLoss()
    optimizer = optim.Adam(model.parameters(), lr = 1e-2)
    scaler = torch.cuda.amp.GradScaler()
    normalize, transforms = Normalize(0, 1), [hflip, vflip, rotate]
    params = {'batch_size' : 8, 'num_workers' : 2, 'pin_memory' : True, 'shuffle' : True}
    training_set = data_loader(path, normalize, transforms, **params)
    if load is not None:
        load_checkpoint(torch.load(load), model)
    for epochs in range(3):
        train_network(training_set, model, optimizer, loss_function, scaler, device)
        cp = {'state_dict' : model.state_dict(), 'optimizer' : optimizer.state_dict()}
```

```
        save_checkpoint(cp, f'{path}/checkpoint/checkpoint.pth.tar')
        save_predictions(training_set, model, f'{path}/predictions/', device)

if __name__ == '__main__':
    main(path = './')
```

Applying the trained model on the input data yielded output predictions. Since these predictions were made on image subparts sized 500x500 pixels, a reassembly function was used to reconstruct the images.

6.2 Radius of Non-circular Shapes

In section 3.3, the radius of the individual wall layers of the carotids was reported. The radius was obtained by taking the square root of the area enclosed by the respective wall segment divided by π. Obtaining the radius in this manner makes the assumption that the wall segments are ideal circles. Since wall segments were not precisely circular but rather polygonal shapes, the reported radius should be interpreted as a marker of the mean distance of all points on the circumference of the given wall segment to the centroid of the segment. This can be proven empirically using simulated sets of non-selfintersecting polygons. In a simulation of 100 polygons with a mean number of 34 corners (range 20 to 50 corners), the mean ratio of the mean distance of the points on the circumference to the centroid, as described above, and the radius of a circle with the same area as the simulated polygon was 0.988 (99% CI 0.972 - 1.004).

Danksagung

Ich möchte mich bei allen bedanken, die mich in der Durchführung der Versuche und beim Verfassen der Arbeit unterstützt haben.

Mein besonderer Dank gilt PD Dr. med. Florian Bönner für die Annahme als Doktorand in seiner Arbeitsgruppe und für die stets freundliche Unterstützung und Betreuung während der Durchführung der Arbeit.

Weiterhin danke ich Dr. med. Fabian Nienhaus, der mir in allen Belangen unterstützend zur Seite stand und immer großes Interesse daran zeigte, nicht nur das Projekt als Ganzes, sondern auch speziell meine Arbeit voranzubringen.

Bedanken möchte ich mich auch bei Dr. rer. nat. Susanne Pfeiler, Dr. med. vet. Annika Jahn und Maik Rothe M. Sc., die mich bei allen Fragen und Problemen während der Experimente mit großer Hilfsbereitschaft unterstützt haben.

Zuletzt bedanke ich mich bei meiner Familie, die das Projekt mit viel Interesse verfolgt und mir in der Konzeption der Arbeit durch vielfache Ratschläge sehr geholfen hat.